Alma Mater Studiorum · Università di Bologna

Dottorato di Ricerca in
Meccanica e Scienze Avanzate dell'Ingegneria (DIMSAI)
Ciclo: XXXIII

Settore Concorsuale:
09/A3 - Progettazione Industriale, Costruzioni Meccaniche e Metallurgia

Settore Scientifico Disciplinare:
ING-IND/14 - Progettazione Meccanica e Costruzione di Macchine

DESIGN, DEVELOPMENT, AND ANALYSIS OF HYBRID METAL-COMPOSITE TUBES FOR INDUSTRIAL APPLICATIONS

Coordinatore Dottorato:
Prof. Ing.
MARCO CARRICATO

Presentata da:
MARCO POVOLO

Supervisore:
Prof. Ing.
ANDREA ZUCCHELLI

Esame Finale Anno 2021

To my parents. For their love, endless support, and encouragement.

Preface

Composite materials were discovered by humans many years ago. The oldest composite for building applications documented is probably wattle and daub, over 6000 years ago[1], in which woven lattice of wooden strips was smeared with a material made of a combination of clay, wet soil, sand, animal dung, and straw.

Since then, composite materials have evolved to a crucial turning point that arrived during the 30s with Fibre-Reinforced Plastic (FRF) development and, in particular, Glass-Fibre-Reinforced-Polymers (GFRP) for commercial use. The story of Carbon-Fibre-Reinforced-Polymers (CFRP) only started in the 60s, and since then, their market growth has been exponential[2].

To the present day, the wide use of fiber-reinforced materials has pushed researchers to focus on many unconventional aspects, such as high stiffness, damping, impact resistance, and other properties that are currently no longer negligible, such as recycling and disposal. In particular, the coupling between metal and CFRP and the damping properties of composite materials in the industrial field were the reasons that prompted the University of Bologna to create a special Ph.D. program financed by a research grant. This research work lasted three years and was conducted in Italy and abroad in collaboration with the company Reglass Srl (Minerbio (BO), Italy), the University of Bologna, and the University of Wisconsin-Milwaukee (US). For this reason, this thesis deals with many industrial aspects often neglected in the academic world. The results obtained and reported allowed to realize new industrial products that made the sponsor company more competitive on the global scene.

This thesis mostly refers to GFRP and CFRP and their application on generally axial-symmetrical components in the aerospace, automotive, printing, and converting industries. Specifically, new materials, production techniques, and products have been investigated. Analytical and numerical methods have also been proposed and validated by experimental tests.

The thesis is divided into three parts. The first part deals with general aspects and the theory of composite materials. Part two focuses mainly on the topic of damping in composite materials and finally the third part concerns the application of the previous concepts for the development of innovative hybrid metal-composite

tubes for industrial application that led to the publication up to now of several scientific papers[3, 4, 5, 6, 7, 8, 9] and others that are under review or ready to be submitted at the time of writing this thesis [10, 11].

Contents

List of Figures

List of Tables

Part I

Composite materials

Chapter 1

Composite Materials: an overview

1.1 Introduction

Composite materials are materials that existed before homo sapiens took control of the earth. Both flora and fauna of the planet are made up of composite materials, but only after the 1960s engineers realize their potentials. The development and applications of composites in the 21st century are now accelerating. Their incredible performances compared to conventional materials are changing designing components belonging to all sectors, from sports to aerospace ones.

The applications covered in this thesis are only a small portion of all the possible ones, currently limited only by the designer's imagination. But composite materials have not only merits. To give a more complete overview to the reader, the composites will always be compared with traditional materials throughout this work.

However, this primary focus of this thesis is the mechanical and dynamical behaviors of axial-symmetric components made of composite materials for the converting, printing, automotive, aerospace, and sport industrial sectors. A particular focus will be made on hybrid tubes and their interface and behavior, like damping and stiffness. Furthermore, innovative analytical, numerical, and experimental methods will always be proposed in the presented fields. It is impossible to write an all-encompassing thesis on composite materials. Still, I hope this work will help engineers and students to face workplace challenges.

Composite materials coupled with nanofibers will also be cited and experimented. However, their detailed study is not the subject of this thesis. Macro and micromechanics will be analyzed but not nanomechanics, since it is a very complex subject that deserves detailed studies separately.

Figure 1.1: A combination of mud and papyrus dried into a construction brick in modern Egypt.

1.2 Definition of a Composite Materials

A composite is a material composed of two, three, or more distinct phases. In this thesis, materials consisting of two different phases in which one (fibers) acts as a reinforcement of a second phase (matrix) are considered. The challenge is to design the material with the desired performance by modifying the volumetric ratio of the two phases.

Composite materials currently refer to all those materials that contain strong fibers embedded in a weaker matrix that keeps the fibers together and in order. The composite material resulting from their coupling will have intermediate performances between fibers and matrix. This thesis refers exclusively to glass fibers and carbon-based fibers, joined by a thermosetting matrix (epoxy resin). Composite materials made with fibers are called Fiber-Reinforced-Polymers (FRP). In particular, the glass-fiber-based ones are called Glass-Fiber-Reinforced-Polymer (GFRP), and the carbon-based ones are called Carbon-Fiber-Reinforced-Polymer (CFRP).

An ancient example of fiber-reinforced-materials was the combination of papyrus as fiber with different matrix to make boats, baskets, rope, and houses (Figure 1.1). Papyrus was used by early Egyptians but is still in use today. What has changed today is the type of fiber and matrix type, but not the theory underlying the composite materials.

Table 1.1: Standard fibers for industrial application properties.

Fiber	Type	ρ (g/cm^3)	α (1/°C)	E (MPa)	R (MPa)	ν
E-Glass	glass	2.6	5.0×10^{-6}	74000	2500	0.25
R-Glass	glass	2.5	3.0×10^{-6}	86000	3200	0.20
HR graphite	PAN	1.7	0.2×10^{-6}	230000	3200	0.30
HM graphite	PAN	1.8	0.8×10^{-6}	390000	2500	0.35
CHM	PITCH	2.2	-1.2×10^{-7}	780000	3200	0.28

1.3 Fibers and matrix properties

Fibers are the primary constituent of composite reinforcement. They are spun into coils and are generally made of glass or carbon. In particular, carbon-based fibers are divided into two types: PAN and PITCH. They consist of thousands of filaments, each with a diameter that varies between 5 μm (for PAN fibers) and 10 μm (for PITCH fibers). The PAN fibers derive from the modification of organic fibers and usually have very high resistance and an elastic modulus between 200 GPa and 400 GPa. Pitch fibers are produced from oil or tar distillation residues and have low resistance respect to PAN fibers but very high elastic modulus to reach 900 GPa. Standard fibers properties used in this research and the industrial field are reported in Table 1.1. However, the matrices most used in industry are those shown in the Table 1.2.

This thesis always refer to composites with a matrix based on epoxy resin made by the company Reglass SRL (Minerbio (BO), Italy), regardless of the fiber used. It is immediate to understand that the advantage of composite materials is to be able to design a material using the fibers present in the Table 1.1 and the matrix in the Table 1.2 to reach and exceed the performance of the common materials shown in the Table 1.3.

The first comparison parameter could be the specific elastic modulus (E/ρ) which, as can easily be seen, is equivalent to about 26×10^3 for both steel and aluminum but that can go up to 26×10^4 for a prepreg based on CHM Pitch fibers, that is up to 10 times higher.

1.4 Manufacturing process

In the previous Section 1.3, it has been introduced how the combination of fiber and matrix can generate composites with performances much higher than the common metals. In the industrial sector, to combine matrix and fiber for axial-symmetric components, different techniques can be used, and the most common are:

Table 1.2: Standard matrix for industrial application properties.

matrix	ρ (g/cm^3)	α (1/℃)	E (MPa)	R (MPa)	ν
Epoxy	1.2	11.0×10^{-5}	4500	130	0.40
Reglass - Epoxy	1.1	6.0×10^{-5}	2200	60	0.36
Phenolic	1.3	1.0×10^{-5}	3000	70	0.40
Polyester	1.2	8.0×10^{-5}	4000	80	0.40
Vinylester	1.1	5.0×10^{-5}	3200	75	-

Table 1.3: Standard materials for industrial application properties.

metal	ρ (g/cm^3)	α (1/℃)	E (MPa)	R (MPa)	ν
Steel	7.8	1.3×10^{-5}	205000	400-1500	0.30
Aluminum alloy	2.8	2.2×10^{-5}	75000	450	0.30

- Filament Winding
- Pull Winding
- Pultrusion
- Wrapping

It is preferable to use a prepreg deposition technology like Wrapping to get products like a high-speed roller for converting and printing industries. This methodology has enormous advantages because it allows obtaining a material with low voids due to air volumes and high performances (Figure 1.2). Besides, prepreg can be created with very low percentages of resin respect to filament winding technology. The main disadvantage is having first to prepare the prepreg and then place it on the mold and is why this technology is generally more expensive.

Once the prepreg is placed, the resin must cross-link to make the product stable. The main techniques for curing are:

- Autoclave
- UV
- Oven
- Microwave

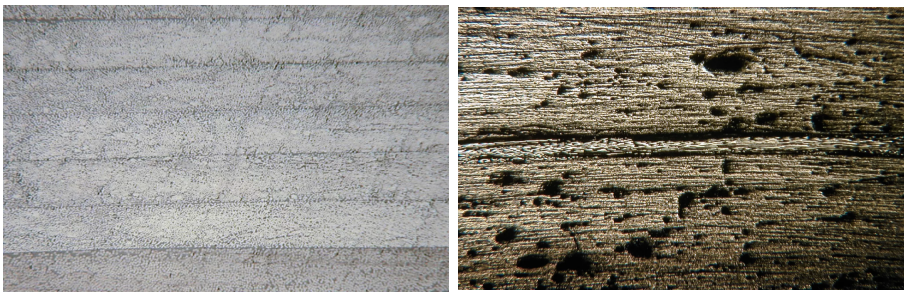

(a) Wrapping technology. (b) Filament Winding technology.

Figure 1.2: Micrograph analysis of the cross sections of tubes.

Reglass SRL company mainly uses the autoclave curing technique. Thanks to the collaboration between the University of Bologna and this company, an innovative curing method for metal-carbon hybrid tubes has been studied and developed successfully, becoming part of its production. It will be illustrated later.

Chapter 2

Mechanics

> "Very simply, a composite is a material which is composed of two or more distinct phases" Carl T. Herakovich[12].

It is not easy to write concisely and elegantly on such a vast and studied subject. For this reason, in this Part (I) concerning the basic concepts of composites' mechanics, I was inspired by a book that represents a milestone, written by Carl T. Herakovich[12]. I tried to integrate what he wrote so elegantly with other authors reported in more recent works. The following does not represent a novelty on the subject, but I thought it appropriate to report this theoretical part to introduce and justify the research presented in the following chapters.

2.1 Basic Concepts

2.1.1 Tensor and matrix transformation

In mechanics and mathematics, a tensor is a mathematical representation of a physical object. It is a generalization of a vector represented by an array of components that change from the different coordinate systems and are functions of the coordinates of a space [13]. In this chapter, only Cartesian tensor, written using index notation are considered. To transform tensor from a coordinate system to another one, equation based on direction cosines a_{ij} (i, j = 1, 2, 3) are proposed. the angles of direction cosines are based on the difference between unprimed axes x_i and primed axes x'_i. The first subscription (i) of a_{ij} corresponds to the unprimed (initial axes) and the second subscription (j) of a_{ij} corresponds to the primed axes (final axes). In Table 2.1 the 3D case for direction cosines for coordinate transformation is depicted.

Figure 2.1 is reported as an example of a transformation in a plane with a rotation of an angle θ. The coefficients a_{ij} of this transformation of rotation on

Table 2.1: Direction cosine correspondence.

	x'_1	x'_2	x'_3
x_1	a_{11}	a_{12}	a_{13}
x_2	a_{21}	a_{22}	a_{23}
x_3	a_{31}	a_{32}	a_{33}

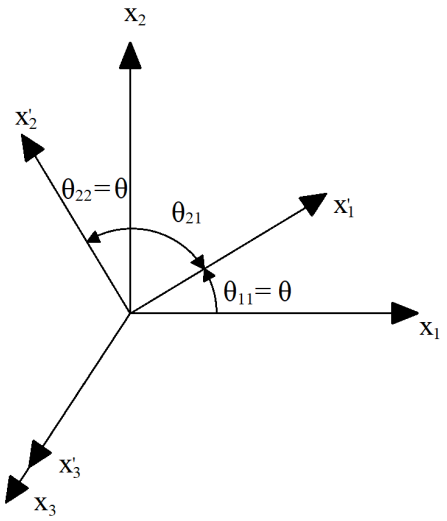

Figure 2.1: Rotation on x_3 axis.

the x_3 axis are represented in matrix form

$$a_{ij} = \begin{bmatrix} \cos\theta & -\sin\theta & 0 \\ \sin\theta & \cos\theta & 0 \\ 0 & 0 & 1 \end{bmatrix} \tag{2.1}$$

It is common to define $m = \cos\theta$ and $n = \sin\theta$, and thus (2.1) can be written

$$a_{ij} = \begin{bmatrix} m & -n & 0 \\ n & m & 0 \\ 0 & 0 & 1 \end{bmatrix} \tag{2.2}$$

For the definition of a_{ij} in (2.1), it easly demonstrable that

$$a_{ji}^{-1} = a_{ij} = (a_{ji})^T \tag{2.3}$$

2.1.2 Deformation and Strain

If a body is subject to a force, it is clear that it may translate and rotate as a rigid body, and deform. These concepts, studied since the 1600s, are widely reported

in the literature, starting by Hooke[14] and, more specifically, by Fung[15]. In the field of composites, by Lekhnitskii[16] and Herakovich[12].

If the gradient of displacements is sufficiently small, the second-order partial derivates of displacements are negligible compared to the first-order one. The strain tensor ε_{ij} are so defined by

$$\varepsilon_{ij} = \frac{1}{2}(u_{i,j} + u_{j,i}) \tag{2.4}$$

where the definition of displacement $u_{i,j}$ is

$$u_{i,j} = \frac{\partial u_i}{\partial x_j} \tag{2.5}$$

From (2.4), using 3D notation ($i, j = 1, 2, 3$) and the concept of symmetric tensor (i.e., $\varepsilon_{ij} = \varepsilon_{ji}$) the expanded form are

$$\begin{aligned} \varepsilon_{11} &= \frac{\partial u_1}{\partial x_1} \quad \varepsilon_{12} = \varepsilon_{21} = \frac{1}{2}(\frac{\partial u_1}{\partial x_2} + \frac{\partial u_2}{\partial x_1}) \\ \varepsilon_{22} &= \frac{\partial u_2}{\partial x_2} \quad \varepsilon_{13} = \varepsilon_{31} = \frac{1}{2}(\frac{\partial u_1}{\partial x_3} + \frac{\partial u_3}{\partial x_1}) \\ \varepsilon_{33} &= \frac{\partial u_3}{\partial x_3} \quad \varepsilon_{23} = \varepsilon_{32} = \frac{1}{2}(\frac{\partial u_2}{\partial x_3} + \frac{\partial u_3}{\partial x_2}) \end{aligned} \tag{2.6}$$

If i=j, the ε corresponds to the normal components of strain, otherwise if $i \neq j$ the ε corresponds to the shear components of strain. In mechanical of materials study, it is common to use the *engineering shear strain* γ_{ij} which are defined as

$$\begin{aligned} \gamma_{12} &= \gamma_{21} = 2\varepsilon_{12} \\ \gamma_{13} &= \gamma_{31} = 2\varepsilon_{13} \\ \gamma_{23} &= \gamma_{32} = 2\varepsilon_{23} \end{aligned} \tag{2.7}$$

and replacing (2.6) in (2.7)

$$\begin{aligned} \gamma_{12} &= \frac{\partial u_1}{\partial x_2} + \frac{\partial u_2}{\partial x_1} \\ \gamma_{13} &= \frac{\partial u_1}{\partial x_3} + \frac{\partial u_3}{\partial x_1} \\ \gamma_{23} &= \frac{\partial u_2}{\partial x_3} + \frac{\partial u_3}{\partial x_2} \end{aligned} \tag{2.8}$$

Finally, the second-order strain tensor can be written, in matrix notation, in the two forms (mathematical and with engineering shear strains) as

Table 2.2: Contracted notation of the 6 independent components of strain.

Tensorial	Contracted
ε_{11}	ε_1
ε_{22}	ε_2
ε_{33}	ε_3
γ_{23}	γ_4
γ_{13}	γ_5
γ_{12}	γ_6

$$[\varepsilon] = \begin{bmatrix} \varepsilon_{11} & \varepsilon_{12} & \varepsilon_{13} \\ \varepsilon_{12} & \varepsilon_{22} & \varepsilon_{23} \\ \varepsilon_{13} & \varepsilon_{23} & \varepsilon_{33} \end{bmatrix} = \begin{bmatrix} \varepsilon_{11} & \frac{\gamma_{12}}{2} & \frac{\gamma_{13}}{2} \\ \frac{\gamma_{12}}{2} & \varepsilon_{22} & \frac{\gamma_{23}}{2} \\ \frac{\gamma_{13}}{2} & \frac{\gamma_{23}}{2} & \varepsilon_{33} \end{bmatrix} \tag{2.9}$$

Various books, like Barbero [17], refers to the six components of strain which are independent in contracted notation as in Table 2.2.

2.1.3 Stress and Equilibrium

Stress are expressed as $\frac{Force}{Area}$ MPa. The second-order tensor of stress can be written, dividing the components into the 3D orthogonal planes, as reported in Figure 2.2, which have only positive components. The notation for stress is similar to the strain one and is σ_{ij} (for i,j = 1, 2, 3). The second-order tensor can be express in matrix notation, and the resultant matrix is symmetric as the strains one. For this reason, σ_{ij} is equal to σ_{ji}. If $i \neq j$, the stress components will also be written as shear stress components τ_{ij}.

$$[\sigma] = \begin{bmatrix} \sigma_{11} & \sigma_{21} & \sigma_{31} \\ \sigma_{12} & \sigma_{22} & \sigma_{32} \\ \sigma_{13} & \sigma_{23} & \sigma_{32} \end{bmatrix} = \begin{bmatrix} \sigma_{xx} & \tau_{xy} & \tau_{xz} \\ \tau_{xy} & \sigma_{yy} & \tau_{yz} \\ \tau_{xz} & \tau_{yz} & \sigma_{zz} \end{bmatrix} \tag{2.10}$$

As for the strain, the contracted notation can be adopted for the stresses in Table 2.3.

Body force per unit volume can be considered negligible for applying standard mechanics and composite materials in the analytical study. For this reason, the equilibrium could be written in the form

$$\sigma_{ij,j} = 0 \tag{2.11}$$

and written in the expanding form with the global x-y-z coordinate system

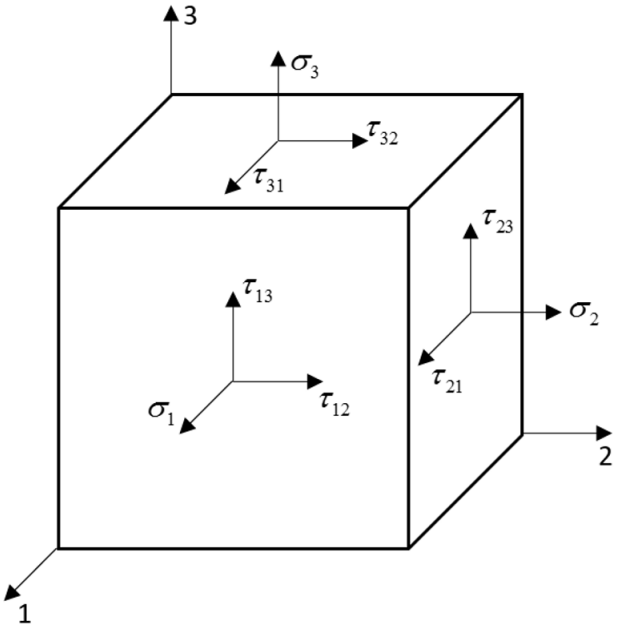

Figure 2.2: Components of 3D stress

Table 2.3: Contracted notation of the 6 independent components of stress.

Tensorial	Contracted
σ_{11}	σ_1
σ_{22}	σ_2
σ_{33}	σ_3
τ_{23}	τ_4
τ_{13}	τ_5
τ_{12}	τ_6

$$\begin{aligned} \frac{\partial \sigma_{xx}}{\partial x} + \frac{\partial \sigma_{xy}}{\partial y} + \frac{\partial \sigma_{xz}}{\partial z} = 0 \\ \frac{\partial \sigma_{xy}}{\partial x} + \frac{\partial \sigma_{yy}}{\partial y} + \frac{\partial \sigma_{yz}}{\partial z} = 0 \\ \frac{\partial \sigma_{xz}}{\partial x} + \frac{\partial \sigma_{yz}}{\partial y} + \frac{\partial \sigma_{zz}}{\partial z} = 0 \end{aligned} \tag{2.12}$$

Regarding the Boundary, Continuity, and Compatibility Condition, Gurtin[18] provide more details.

2.1.4 Constitutive Equations

The relationship between stress and strain is linear. It is provided by the Constitutive Equation and concerns linear elastic material response. The general form is expressed as

$$\sigma_{ij} = C_{ijkl}\varepsilon_{kl} \tag{2.13}$$

This relationship is called the generalized Hooke's law and the C_{ijkl} therms are the elastic constant called *elastic moduli* or *stiffness*[14, 19]. Inverting (2.13) gives the strains in function of stresses in the form

$$\varepsilon_{ij} = C^{-1}_{ijkl}\sigma_{kl} \tag{2.14}$$

that is called *compliance* S_{ijkl} as the inverting of stiffness

$$\varepsilon_{ij} = S_{ijkl}\sigma_{kl} \tag{2.15}$$

2.2 3D Mechanics

2.2.1 Hook's Law: Generalization

In Section 2.1, in particular in (2.13), that the most generalized form of the linear relationship between stress and strain, called *Generalized Hook's law* was expressed as

$$\sigma_{ij} = C_{ijkl}\varepsilon_{kl} \tag{2.16}$$

where C_{ijkl} is the tensor of fourth-order with 3^4 (81) elastic constants. For the symmetry of stress and strain, the number of 81 constants can be reduce to 36 because $C_{ijkl} = C_{ijlk}$. So the C_{ijkl} therms became C_{ij} with (i,j = 1, 2, 3, ..., 6).

From the quadratic form of *strain energy density function*[20], the C_{ij} constants can be reduce to 21 independent ones. These 21 constants identified a type of material called *Anisotropic*. The symmetric matrix of stiffness can be written as

$$[C_{ij}] = \begin{bmatrix} C_{11} & C_{21} & C_{31} & C_{41} & C_{51} & C_{61} \\ C_{12} & C_{22} & C_{32} & C_{42} & C_{52} & C_{62} \\ C_{13} & C_{23} & C_{33} & C_{43} & C_{53} & C_{63} \\ C_{14} & C_{24} & C_{34} & C_{44} & C_{54} & C_{64} \\ C_{15} & C_{25} & C_{35} & C_{45} & C_{55} & C_{65} \\ C_{16} & C_{26} & C_{36} & C_{46} & C_{56} & C_{66} \end{bmatrix} \tag{2.17}$$

If the stiffness matrix is symmetric, the compliance matrix and coefficients are also symmetric because

$$S_{ij} = C_{ij}^{-1} \tag{2.18}$$

Chapter 3

Material Mechanics

3.1 Symmetry

As shown in Section 2.2, an anisotropic material has 21 independent constants. If a general anisotropic material has a plane of symmetry, it is called a *monoclinic* material. A first example can be a plane of symmetry on x_1 and x_2 axes. In this case, the matrix reported in (2.17) will present different zero terms caused by the dependency of the constants by each other. So

$$\begin{aligned} C_{14} &= 0 \\ C_{15} &= 0 \\ C_{24} &= 0 \\ C_{25} &= 0 \\ C_{34} &= 0 \\ C_{35} &= 0 \\ C_{46} &= 0 \\ C_{56} &= 0 \end{aligned} \tag{3.1}$$

and the stiffness matrix became

$$[C_{ij}] = \begin{bmatrix} C_{11} & C_{21} & C_{31} & 0 & 0 & C_{61} \\ C_{12} & C_{22} & C_{32} & 0 & 0 & C_{62} \\ C_{13} & C_{23} & C_{33} & 0 & 0 & C_{63} \\ 0 & 0 & 0 & C_{44} & C_{54} & 0 \\ 0 & 0 & 0 & C_{45} & C_{55} & 0 \\ C_{16} & C_{26} & C_{36} & 0 & 0 & C_{66} \end{bmatrix} \tag{3.2}$$

as indicated in 3.2, a monoclinic material has 13 independent constants.

If another symmetry plane is considered, the material will be called *orthotropic*, and other constants became equal to zero due to the dependency relationship. This zero constant has to be added to the others reported for monoclinic material

$$\begin{aligned} C_{16} &= 0 \\ C_{26} &= 0 \\ C_{36} &= 0 \\ C_{45} &= 0 \end{aligned} \tag{3.3}$$

and the stiffness matrix

$$[C_{ij}] = \begin{bmatrix} C_{11} & C_{21} & C_{31} & 0 & 0 & 0 \\ C_{12} & C_{22} & C_{32} & 0 & 0 & 0 \\ C_{13} & C_{23} & C_{33} & 0 & 0 & 0 \\ 0 & 0 & 0 & C_{44} & 0 & 0 \\ 0 & 0 & 0 & 0 & C_{55} & 0 \\ 0 & 0 & 0 & 0 & 0 & C_{66} \end{bmatrix} \tag{3.4}$$

The constitutive Equation reported in (2.13) can be so represented in matrix form

$$\begin{Bmatrix} \sigma_1 \\ \sigma_2 \\ \sigma_3 \\ \tau_{23} \\ \tau_{13} \\ \tau_{12} \end{Bmatrix} = \begin{bmatrix} C_{11} & C_{21} & C_{31} & 0 & 0 & 0 \\ C_{12} & C_{22} & C_{32} & 0 & 0 & 0 \\ C_{13} & C_{23} & C_{33} & 0 & 0 & 0 \\ 0 & 0 & 0 & C_{44} & 0 & 0 \\ 0 & 0 & 0 & 0 & C_{55} & 0 \\ 0 & 0 & 0 & 0 & 0 & C_{66} \end{bmatrix} \begin{Bmatrix} \varepsilon_1 \\ \varepsilon_2 \\ \varepsilon_3 \\ \gamma_{23} \\ \gamma_{13} \\ \gamma_{12} \end{Bmatrix} \tag{3.5}$$

3.2 Common materials

3.2.1 UD lamina

Tha unidirectional lamina of common composite materials has another special property. Its linear elasticity does not depend on the direction in almost one of its planes. This kind of material is called *transversely isotropic material*. In this thesis, I will refer mainly to this type of material and the definition of principal directions (fiber direction = 1), as in Figure 3.1.

The transverse isotropy behavior results in the following stiffness coefficients mutual relationship.

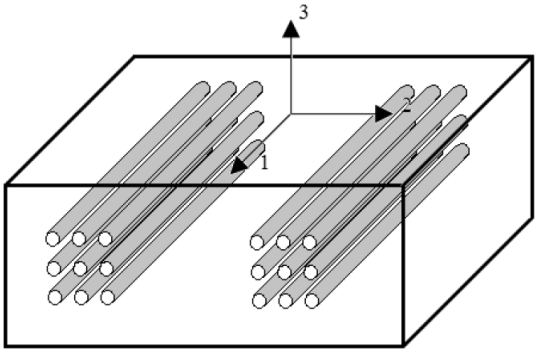

Figure 3.1: Transverse isotropic material rappresentation

$$\begin{aligned} C_{22} &= C_{33} \\ C_{12} &= C_{13} \\ C_{55} &= C_{66} \\ C_{44} &= \frac{C_{22} - C_{23}}{2} \end{aligned} \tag{3.6}$$

The independent constants for a transversely isotropic material are only 5. So the stiffness matrix can be written in the form

$$[C_{ij}] = \begin{bmatrix} C_{11} & C_{21} & C_{31} & 0 & 0 & 0 \\ C_{12} & C_{22} & C_{32} & 0 & 0 & 0 \\ C_{13} & C_{23} & C_{33} & 0 & 0 & 0 \\ 0 & 0 & 0 & \frac{C_{22}-C_{23}}{2} & 0 & 0 \\ 0 & 0 & 0 & 0 & C_{66} & 0 \\ 0 & 0 & 0 & 0 & 0 & C_{66} \end{bmatrix} \tag{3.7}$$

So the constitutive Equation reported in (2.13) can be so represented in matrix form

$$\begin{Bmatrix} \sigma_1 \\ \sigma_2 \\ \sigma_3 \\ \tau_{23} \\ \tau_{13} \\ \tau_{12} \end{Bmatrix} = \begin{bmatrix} C_{11} & C_{21} & C_{31} & 0 & 0 & 0 \\ C_{12} & C_{22} & C_{32} & 0 & 0 & 0 \\ C_{13} & C_{23} & C_{33} & 0 & 0 & 0 \\ 0 & 0 & 0 & \frac{C_{22}-C_{23}}{2} & 0 & 0 \\ 0 & 0 & 0 & 0 & C_{66} & 0 \\ 0 & 0 & 0 & 0 & 0 & C_{66} \end{bmatrix} \begin{Bmatrix} \varepsilon_1 \\ \varepsilon_2 \\ \varepsilon_3 \\ \gamma_{23} \\ \gamma_{13} \\ \gamma_{12} \end{Bmatrix} \tag{3.8}$$

3.2.2 Metals

On the other hand, metal materials are called *isotropic* for their intrinsic properties of independency from direction and to have all the planes as planes of symmetry. In this case, this kind of materials have an additional relationship between their stiffness coefficients

$$\begin{aligned} C_{11} &= C_{22} \\ C_{12} &= C_{23} \\ C_{66} &= \frac{C_{11} - C_{12}}{2} \end{aligned} \tag{3.9}$$

The remain independent elastic constants are only 2, and the stiffness matrix can be written in the form

$$[C_{ij}] = \begin{bmatrix} C_{11} & C_{21} & C_{31} & 0 & 0 & 0 \\ C_{12} & C_{22} & C_{32} & 0 & 0 & 0 \\ C_{13} & C_{23} & C_{33} & 0 & 0 & 0 \\ 0 & 0 & 0 & \frac{C_{12}-C_{12}}{2} & 0 & 0 \\ 0 & 0 & 0 & 0 & \frac{C_{12}-C_{12}}{2} & 0 \\ 0 & 0 & 0 & 0 & 0 & \frac{C_{12}-C_{12}}{2} \end{bmatrix} \tag{3.10}$$

and the constitutive equation reported in (2.13) can be so rappresented in matrix form

$$\begin{Bmatrix} \sigma_1 \\ \sigma_2 \\ \sigma_3 \\ \tau_{23} \\ \tau_{13} \\ \tau_{12} \end{Bmatrix} = \begin{bmatrix} C_{11} & C_{21} & C_{31} & 0 & 0 & 0 \\ C_{12} & C_{22} & C_{32} & 0 & 0 & 0 \\ C_{13} & C_{23} & C_{33} & 0 & 0 & 0 \\ 0 & 0 & 0 & \frac{C_{12}-C_{12}}{2} & 0 & 0 \\ 0 & 0 & 0 & 0 & \frac{C_{12}-C_{12}}{2} & 0 \\ 0 & 0 & 0 & 0 & 0 & \frac{C_{12}-C_{12}}{2} \end{bmatrix} \begin{Bmatrix} \varepsilon_1 \\ \varepsilon_2 \\ \varepsilon_3 \\ \gamma_{23} \\ \gamma_{13} \\ \gamma_{12} \end{Bmatrix} \tag{3.11}$$

3.3 Engineering Constants

The properties of materials obtained during laboratory tests are usually expressed in *engineering constants*, which are different from the stiffness coefficients C_{ij}. For an orthotropic material subjected to a 3D state of stresses, the equation of stresses

could be expresses as

$$\begin{aligned}
\varepsilon_1 &= \frac{\sigma_1}{E_1} - \frac{\nu_{21}}{E_2}\sigma_2 - \frac{\nu_{31}}{E_3}\sigma_3 \\
\varepsilon_2 &= -\frac{\nu_{12}}{E_1}\sigma_1 + \frac{\sigma_2}{E_2} - \frac{\nu_{32}}{E_3}\sigma_3 \\
\varepsilon_3 &= -\frac{\nu_{13}}{E_1}\sigma_1 - \frac{\nu_{23}}{E_2}\sigma_2 + \frac{\sigma_3}{E_3} \\
\gamma_{23} &= \frac{\tau_{23}}{G_{23}} \\
\gamma_{13} &= \frac{\tau_{13}}{G_{13}} \\
\gamma_{12} &= \frac{\tau_{12}}{G_{12}}
\end{aligned} \tag{3.12}$$

Where in Equation 3.12, the E_{ij} terms are Young's moduli in the three coordinates (1 the direction of the fibers, 2, and 3 the transverse directions) and the ν_{ij} terms are the Poisson's ratios. It's important to note that the Poisson's ratios are different for a general unidirectional composite material because the first term i depends on the direction of applied stress, and j terms depend on the strain direction. The G_{ij} terms are the shear moduli and are defined for shear stress loading in the plane ij.

Substituting the Equation of stresses 3.12 in the Equation 2.15, we can write the constitutive equation in the compliance form in terms of engineering constants for a general orthotropic material

$$\begin{Bmatrix} \varepsilon_1 \\ \varepsilon_2 \\ \varepsilon_3 \\ \gamma_{23} \\ \gamma_{13} \\ \gamma_{12} \end{Bmatrix} = \begin{bmatrix} S_{11} & S_{21} & S_{31} & 0 & 0 & 0 \\ S_{12} & S_{22} & S_{32} & 0 & 0 & 0 \\ S_{13} & S_{23} & S_{33} & 0 & 0 & 0 \\ 0 & 0 & 0 & S_{44} & 0 & 0 \\ 0 & 0 & 0 & 0 & S_{66} & 0 \\ 0 & 0 & 0 & 0 & 0 & S_{66} \end{bmatrix} \begin{Bmatrix} \sigma_1 \\ \sigma_2 \\ \sigma_3 \\ \tau_{23} \\ \tau_{13} \\ \tau_{12} \end{Bmatrix} \tag{3.13}$$

substituting

$$\begin{Bmatrix} \varepsilon_1 \\ \varepsilon_2 \\ \varepsilon_3 \\ \gamma_{23} \\ \gamma_{13} \\ \gamma_{12} \end{Bmatrix} = \begin{bmatrix} \frac{1}{E_1} & \frac{-\nu_{21}}{E_2} & \frac{-\nu_{31}}{E_3} & 0 & 0 & 0 \\ \frac{-\nu_{12}}{E_1} & \frac{1}{E_2} & \frac{-\nu_{32}}{E_3} & 0 & 0 & 0 \\ \frac{-\nu_{13}}{E_1} & \frac{-\nu_{23}}{E_2} & \frac{1}{E_3} & 0 & 0 & 0 \\ 0 & 0 & 0 & \frac{1}{G_{23}} & 0 & 0 \\ 0 & 0 & 0 & 0 & \frac{1}{G_{13}} & 0 \\ 0 & 0 & 0 & 0 & 0 & \frac{1}{G_{12}} \end{bmatrix} \begin{Bmatrix} \sigma_1 \\ \sigma_2 \\ \sigma_3 \\ \tau_{23} \\ \tau_{13} \\ \tau_{12} \end{Bmatrix} \tag{3.14}$$

and for a general unidirectional composite material (transversely isotropic) as reported in Subsection 3.2.1 where $E_2 = E_3$, $\nu_{12} = \nu_{13}$, $G_{12} = G_{13}$, $G_{23} = \frac{E_2}{2(1+\nu 23)}$

and the symmetry of the compliance matrix, i.e. $S_{ij} = Sji$, simplifies to

$$\begin{Bmatrix} \varepsilon_1 \\ \varepsilon_2 \\ \varepsilon_3 \\ \gamma_{23} \\ \gamma_{13} \\ \gamma_{12} \end{Bmatrix} = \begin{bmatrix} \frac{1}{E_1} & \frac{-\nu_{12}}{E_1} & \frac{-\nu_{12}}{E_1} & 0 & 0 & 0 \\ \frac{-\nu_{12}}{E_1} & \frac{1}{E_2} & \frac{-\nu_{23}}{E_2} & 0 & 0 & 0 \\ \frac{-\nu_{12}}{E_1} & \frac{-\nu_{23}}{E_2} & \frac{1}{E_2} & 0 & 0 & 0 \\ 0 & 0 & 0 & \frac{2(1+\nu_{23})}{E_2} & 0 & 0 \\ 0 & 0 & 0 & 0 & \frac{1}{G_{12}} & 0 \\ 0 & 0 & 0 & 0 & 0 & \frac{1}{G_{12}} \end{bmatrix} \begin{Bmatrix} \sigma_1 \\ \sigma_2 \\ \sigma_3 \\ \tau_{23} \\ \tau_{13} \\ \tau_{12} \end{Bmatrix} \tag{3.15}$$

The inversion of the compliance matrix $[S]$ gives the stiffness matrix $[C]$ in terms of engineering constants of the constitutive equations.

$$\big[S\big]^{-1} = \big[C\big] \tag{3.16}$$

Defining $\Delta = \frac{(1-\nu_{12}\nu_{21}-\nu_{23}\nu_{32}-\nu_{13}\nu_{31}-2\nu_{21}\nu_{23}\nu_{13}}{E_1E_2E_3}$ the stiffness matrix can be expressed as

$$\begin{Bmatrix} \sigma_1 \\ \sigma_2 \\ \sigma_3 \\ \tau_{23} \\ \tau_{13} \\ \tau_{12} \end{Bmatrix} = \begin{bmatrix} \frac{1-\nu_{23}\nu_{32}}{E_2E_3\Delta} & \frac{\nu_{21}-\nu_{23}\nu_{31}}{E_2E_3\Delta} & \frac{\nu_{31}-\nu_{21}\nu_{32}}{E_2E_3\Delta} & 0 & 0 & 0 \\ \frac{\nu_{21}-\nu_{23}\nu_{31}}{E_2E_3\Delta} & \frac{1-\nu_{13}\nu_{31}}{E_1E_3\Delta} & \frac{\nu_{32}-\nu_{12}\nu_{31}}{E_1E_3\Delta} & 0 & 0 & 0 \\ \frac{\nu_{31}-\nu_{21}\nu_{32}}{E_2E_3\Delta} & \frac{\nu_{32}-\nu_{12}\nu_{31}}{E_1E_3\Delta} & \frac{1-\nu_{12}\nu_{21}}{E_1E_2\Delta} & 0 & 0 & 0 \\ 0 & 0 & 0 & G_{23} & 0 & 0 \\ 0 & 0 & 0 & 0 & G_{13} & 0 \\ 0 & 0 & 0 & 0 & 0 & G_{12} \end{bmatrix} \begin{Bmatrix} \varepsilon_1 \\ \varepsilon_2 \\ \varepsilon_3 \\ \gamma_{23} \\ \gamma_{13} \\ \gamma_{12} \end{Bmatrix} \tag{3.17}$$

The Stiffness matrix for a general unidirectional composite material (transversely isotropic material) is not reported because, obviously, the inversion of the compliance form is more simple and more writable.

3.4 Coordinate transformations

As shown in Chapter 2, the stiffness and the compliance matrix are 4th order tensors; instead, stress and strain are 2nd order tensors. The quantities expressed in the coordinate system for the principal material are denoted with subscript 1, and the quantities expressed in the global coordinate are denoted with subscript x.

The most common transformation through different coordinate systems is the rotation through an angle θ about the *z-axis* because it changes the direction of the fibers in a common unidirectional composite material.

To transform using engineering constants, it is necessary to define two transformations matrix, for stresses transformation (T_1) and for strains transformations

(T_2). The stresses relation between principal material coordinates and the global coordinates can be expressed as

$$\begin{Bmatrix} \sigma_1 \\ \sigma_2 \\ \sigma_3 \\ \tau_{23} \\ \tau_{13} \\ \tau_{12} \end{Bmatrix}_1 = \left[T_1\right] \begin{Bmatrix} \sigma_1 \\ \sigma_2 \\ \sigma_3 \\ \tau_{23} \\ \tau_{13} \\ \tau_{12} \end{Bmatrix}_x \tag{3.18}$$

$$\begin{Bmatrix} \sigma_1 \\ \sigma_2 \\ \sigma_3 \\ \tau_{23} \\ \tau_{13} \\ \tau_{12} \end{Bmatrix}_1 = \begin{bmatrix} c^2 & s^2 & 0 & 0 & 0 & 2cs \\ s^2 & c^2 & 0 & 0 & 0 & -2cs \\ 0 & 0 & 1 & 0 & 0 & 0 \\ 0 & 0 & 0 & c & -s & 0 \\ 0 & 0 & 0 & s & c & 0 \\ -cs & cs & 0 & 0 & 0 & c^2 - s^2 \end{bmatrix} \begin{Bmatrix} \sigma_1 \\ \sigma_2 \\ \sigma_3 \\ \tau_{23} \\ \tau_{13} \\ \tau_{12} \end{Bmatrix}_x \tag{3.19}$$

where $s = \sin\theta$ and $c = \cos\theta$. Likewise, the strains relation between principal material coordinates and the global coordinates can be expressed as

$$\begin{Bmatrix} \varepsilon_1 \\ \varepsilon_2 \\ \varepsilon_3 \\ \gamma_{23} \\ \gamma_{13} \\ \gamma_{12} \end{Bmatrix}_1 = \left[T_2\right] \begin{Bmatrix} \varepsilon_1 \\ \varepsilon_2 \\ \varepsilon_3 \\ \gamma_{23} \\ \gamma_{13} \\ \gamma_{12} \end{Bmatrix}_x \tag{3.20}$$

$$\begin{Bmatrix} \varepsilon_1 \\ \varepsilon_2 \\ \varepsilon_3 \\ \gamma_{23} \\ \gamma_{13} \\ \gamma_{12} \end{Bmatrix}_1 = \begin{bmatrix} c^2 & s^2 & 0 & 0 & 0 & cs \\ s^2 & c^2 & 0 & 0 & 0 & -cs \\ 0 & 0 & 1 & 0 & 0 & 0 \\ 0 & 0 & 0 & c & -s & 0 \\ 0 & 0 & 0 & s & c & 0 \\ -2cs & 2cs & 0 & 0 & 0 & c^2 - s^2 \end{bmatrix} \begin{Bmatrix} \varepsilon_1 \\ \varepsilon_2 \\ \varepsilon_3 \\ \gamma_{23} \\ \gamma_{13} \\ \gamma_{12} \end{Bmatrix}_x \tag{3.21}$$

The rotation matrices (T_1 and T_2) are different by only two terms. It can be notices that $[T_1(\theta)]^{-1} = [T_1(-\theta)]$ and $[T_2(\theta)]^{-1} = [T_2(-\theta)]$.

3.4.1 Transformed stiffness matrix

The transformed stiffness matrix $[\bar{C}]$ can be determined starting from the constitutive equation 2.13 in the principal material coordinates (subscript 1) and apply the stress and strain transformation (3.19, 3.21) to pass in the global coordinate system (subscript x).

$$\begin{Bmatrix} \sigma_1 \\ \sigma_2 \\ \sigma_3 \\ \tau_{23} \\ \tau_{13} \\ \tau_{12} \end{Bmatrix}_1 = \begin{bmatrix} C \end{bmatrix} \begin{Bmatrix} \varepsilon_1 \\ \varepsilon_2 \\ \varepsilon_3 \\ \gamma_{23} \\ \gamma_{13} \\ \gamma_{12} \end{Bmatrix}_1 \tag{3.22}$$

$$\begin{bmatrix} T_1 \end{bmatrix} \begin{Bmatrix} \sigma_1 \\ \sigma_2 \\ \sigma_3 \\ \tau_{23} \\ \tau_{13} \\ \tau_{12} \end{Bmatrix}_x = \begin{bmatrix} C \end{bmatrix} \begin{Bmatrix} \varepsilon_1 \\ \varepsilon_2 \\ \varepsilon_3 \\ \gamma_{23} \\ \gamma_{13} \\ \gamma_{12} \end{Bmatrix}_1 \tag{3.23}$$

$$\begin{bmatrix} T_1 \end{bmatrix} \begin{Bmatrix} \sigma_1 \\ \sigma_2 \\ \sigma_3 \\ \tau_{23} \\ \tau_{13} \\ \tau_{12} \end{Bmatrix}_x = \begin{bmatrix} C \end{bmatrix} \begin{bmatrix} T_2 \end{bmatrix} \begin{Bmatrix} \varepsilon_1 \\ \varepsilon_2 \\ \varepsilon_3 \\ \gamma_{23} \\ \gamma_{13} \\ \gamma_{12} \end{Bmatrix}_x \tag{3.24}$$

and multiply for both parts by $[T_1]^{-1}$

$$\begin{bmatrix} T_1 \end{bmatrix}^{-1} \begin{bmatrix} T_1 \end{bmatrix} \begin{Bmatrix} \sigma_1 \\ \sigma_2 \\ \sigma_3 \\ \tau_{23} \\ \tau_{13} \\ \tau_{12} \end{Bmatrix}_x = \begin{bmatrix} T_1 \end{bmatrix}^{-1} \begin{bmatrix} C \end{bmatrix} \begin{bmatrix} T_2 \end{bmatrix} \begin{Bmatrix} \varepsilon_1 \\ \varepsilon_2 \\ \varepsilon_3 \\ \gamma_{23} \\ \gamma_{13} \\ \gamma_{12} \end{Bmatrix}_x \tag{3.25}$$

the results is

$$\begin{Bmatrix} \sigma_1 \\ \sigma_2 \\ \sigma_3 \\ \tau_{23} \\ \tau_{13} \\ \tau_{12} \end{Bmatrix}_x = \begin{bmatrix} T_1 \end{bmatrix}^{-1} \begin{bmatrix} C \end{bmatrix} \begin{bmatrix} T_2 \end{bmatrix} \begin{Bmatrix} \varepsilon_1 \\ \varepsilon_2 \\ \varepsilon_3 \\ \gamma_{23} \\ \gamma_{13} \\ \gamma_{12} \end{Bmatrix}_x \tag{3.26}$$

and, defining the *transformed stiffness matrix* $[\bar{C}]$ as

$$\begin{bmatrix} \bar{C} \end{bmatrix} = \begin{bmatrix} T_1 \end{bmatrix}^{-1} \begin{bmatrix} C \end{bmatrix} \begin{bmatrix} T_2 \end{bmatrix} \tag{3.27}$$

the constitutive equation in global coordinate system can be written as

$$\begin{Bmatrix} \sigma_1 \\ \sigma_2 \\ \sigma_3 \\ \tau_{23} \\ \tau_{13} \\ \tau_{12} \end{Bmatrix}_x = \left[\bar{C}\right] \begin{Bmatrix} \varepsilon_1 \\ \varepsilon_2 \\ \varepsilon_3 \\ \gamma_{23} \\ \gamma_{13} \\ \gamma_{12} \end{Bmatrix}_x \tag{3.28}$$

For a monoclinic material 3.2, $[\bar{C}]$ can be determined from T_1 (3.19), T_2 (3.21) and 3.27.

$$\left[\bar{C}\right] = \begin{bmatrix} \bar{C}_{11} & \bar{C}_{21} & \bar{C}_{31} & 0 & 0 & \bar{C}_{61} \\ \bar{C}_{12} & \bar{C}_{22} & \bar{C}_{32} & 0 & 0 & \bar{C}_{62} \\ \bar{C}_{13} & \bar{C}_{23} & \bar{C}_{33} & 0 & 0 & \bar{C}_{63} \\ 0 & 0 & 0 & \bar{C}_{44} & \bar{C}_{54} & 0 \\ 0 & 0 & 0 & \bar{C}_{45} & \bar{C}_{55} & 0 \\ \bar{C}_{16} & \bar{C}_{26} & \bar{C}_{36} & 0 & 0 & \bar{C}_{66} \end{bmatrix} \tag{3.29}$$

The single stiffness terms of $[\bar{C}]$ in extended form

$$\begin{aligned} \bar{C}_{11} &= c^4 C_{11} + 2c^2 s^2 (C_{12} + 2C_{66}) + s^4 C_{22} \\ \bar{C}_{12} &= s^2 c^2 (C_{11} + C_{22} - 4C_{66}) + (s^4 + c^4) C_{12} \\ \bar{C}_{13} &= c^2 C_{13} + s^2 C_{23} \\ \bar{C}_{16} &= sc(c^2 (C_{11} - C_{12} - 2C_{66}) + s^2 (C_{12} - C_{22} - 2C_{66})) \\ \bar{C}_{22} &= s^4 C_{11} + 2c^2 s^2 (C_{12} + 2C_{66}) + c^4 C_{22} \\ \bar{C}_{23} &= s^2 C_{13} + c^2 C_{23} \\ \bar{C}_{26} &= sc(s^2 (C_{11} - C_{12} - 2C_{66}) + c^2 (C_{12} - C_{22} + 2C_{66})) \\ \bar{C}_{33} &= C_{33} \\ \bar{C}_{36} &= cs(C_{13} - C_{23}) \\ \bar{C}_{44} &= c^2 C_{44} + s^2 C_{55} \\ \bar{C}_{45} &= cs(C_{55} - C_{44}) \\ \bar{C}_{55} &= s^2 C_{44} + c^2 C_{55} \\ \bar{C}_{66} &= s^2 c^2 (C_{11} - 2C_{12} + C_{22}) + (s^2 - c^2)^2 C_{66} \end{aligned} \tag{3.30}$$

It can be noticed that all the cs terms are identically zero for particular θ angles like 0° and 90°.

Transversely isotropic stiffness case

For a transversely isotropic material (Section 3.2.1 the equation can be simplified because

$$\begin{aligned} C_{22} &= C_{33} \\ C_{12} &= C_{13} \\ C_{55} &= C_{66} \\ C_{44} &= \frac{C_{22} - C_{33}}{2} \end{aligned} \tag{3.31}$$

3.4.2 Transformed compliance matrix

The most simple way to determinate the compliance matrix in global coordinate system $[\bar{S}]$ is inverting the stiffness matrix expressed in global coordinate system $[\bar{C}]$

$$\left[\bar{S}\right] = \left[\bar{C}\right]^{-1} \tag{3.32}$$

in extended form

$$\left[\bar{S}\right] = (\left[T_1\right]^{-1} \left[C\right] \left[T_2\right])^{-1} \tag{3.33}$$

$$\left[\bar{S}\right] = \left[T_2\right]^{-1} \left[C\right]^{-1} (\left[T_1\right]^{-1})^{-1} \tag{3.34}$$

then

$$\left[\bar{S}\right] = \left[T_2\right]^{-1} \left[S\right] \left[T_1\right] \tag{3.35}$$

As reported for the monoclinic material 3.2 for the stiffness matrix 3.29, the transformed compliance matrix expressed in global coordinate system is

$$\left[\bar{S}\right] = \begin{bmatrix} \bar{S}_{11} & \bar{S}_{21} & \bar{S}_{31} & 0 & 0 & \bar{S}_{61} \\ \bar{S}_{12} & \bar{S}_{22} & \bar{S}_{32} & 0 & 0 & \bar{S}_{62} \\ \bar{S}_{13} & \bar{S}_{23} & \bar{S}_{33} & 0 & 0 & \bar{S}_{63} \\ 0 & 0 & 0 & \bar{S}_{44} & \bar{S}_{54} & 0 \\ 0 & 0 & 0 & \bar{S}_{45} & \bar{S}_{55} & 0 \\ \bar{S}_{16} & \bar{S}_{26} & \bar{S}_{36} & 0 & 0 & \bar{S}_{66} \end{bmatrix} \tag{3.36}$$

The single terms of $[\bar{S}]$ in extended form

$$\begin{aligned}
\bar{S}_{11} &= c^4 S_{11} + c^2 s^2 (2S_{12} + S_{66}) + s^4 S_{22} \\
\bar{S}_{12} &= s^2 c^2 (S_{11} + S_{22} - S_{66}) + (s^4 + c^4) S_{12} \\
\bar{S}_{13} &= c^2 S_{13} + s^2 S_{23} \\
\bar{S}_{16} &= sc(c^2(2S_{11} - 2S_{12} - S_{66}) + s^2(2S_{12} - 2S_{22} + S_{66})) \\
\bar{S}_{22} &= s^4 S_{11} + c^2 s^2 (2S_{12} + S_{66}) + c^4 S_{22} \\
\bar{S}_{23} &= s^2 S_{13} + c^2 S_{23} \\
\bar{S}_{26} &= sc(s^2(2S_{11} - 2S_{12} - S_{66}) + c^2(2S_{12} - 2S_{22} + S_{66})) \\
\bar{S}_{33} &= S_{33} \\
\bar{S}_{36} &= 2cs(S_{13} - S_{23}) \\
\bar{S}_{44} &= c^2 S_{44} + s^2 S_{55} \\
\bar{S}_{45} &= cs(S_{55} - S_{44}) \\
\bar{S}_{55} &= s^2 S_{44} + c^2 S_{55} \\
\bar{S}_{66} &= 4s^2 c^2 (S_{11} - 2S_{12} + S_{22}) + (s^2 - c^2)^2 S_{66}
\end{aligned} \tag{3.37}$$

Transversely isotropic compliance case

For a transversely isotropic material (Section 3.2.1) the equation can be simplified because

$$\begin{aligned}
S_{22} &= S_{33} \\
S_{12} &= S_{13} \\
S_{55} &= S_{66} \\
S_{44} &= \frac{S_{22} - S_{33}}{2}
\end{aligned} \tag{3.38}$$

3.5 Angle dependence of UD lamina stiffness

For a transversely isotropic material, like the unidirectional lamina of CFRP, it is possible to plot the variation of $[\bar{S}]$ and $[\bar{C}]$ terms ij in the function of the angle of the lamina on the global coordinate system. For this example, the performance/characteristics of a generic UD lamina are taken from Ansys Workbench [21, 22] and are reported in Table1 3.1. In Figure 3.2 and 3.3 are shown the variation of the 11 independent terms of $[\bar{S}]$ and $[\bar{C}]$ in function of an angle which varies from $-90°$ to $90°$ respectively. In Appendix 3.7 is shown the Matlab Code to obtain the Figure 3.2a and 3.3.

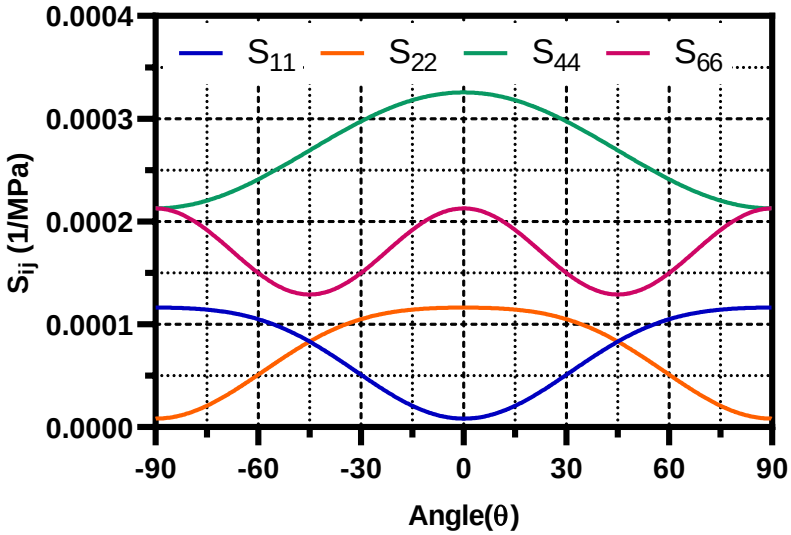

(a) Diagonal terms of $[\bar{S}]$ matrix.

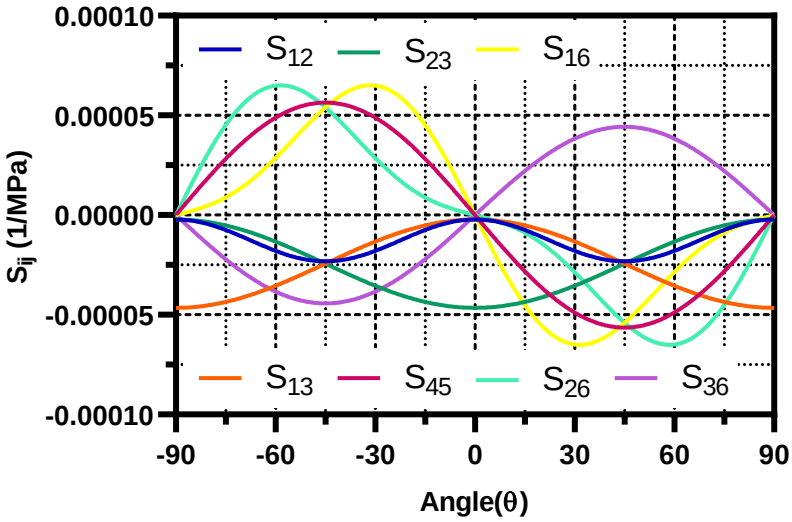

(b) Other terms of $[\bar{S}]$ matrix.

Figure 3.2: Influence of angle variation on $[\bar{S}]$ matrix.

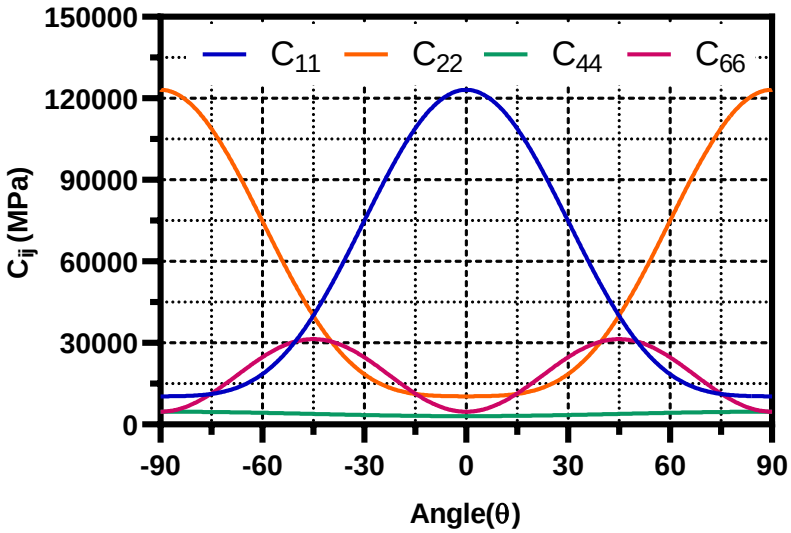

(a) Diagonal terms of $[\bar{C}]$ matrix.

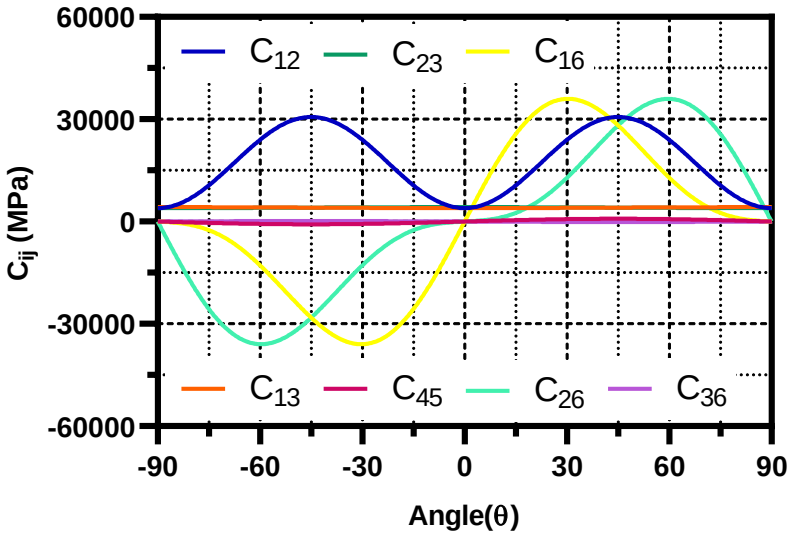

(b) Other terms of $[\bar{C}]$ matrix.

Figure 3.3: Influence of angle variation on $[\bar{C}]$ matrix.

3.6 Thermal strain and stress

The evaluation of the thermal effects on composite is critical. The CTE (Coefficient of Thermal Expansion) of a ply/lamina depends on the angle of orientation θ of the fibers.

From Table 3.1 can be noticed that the CTE in x direction is negative and positive in y and z. This difference is because, in the x direction, the fiber properties are predominant, while in the other directions, those of the matrix are predominant.

Both in the design, but especially in the process, thermal expansion is of great importance. Different CTEs can cause, in the cooling phase, after the curing cycle, thermal stresses that can cause breakage and delaminations.

CTEs in literature are denoted by α, in the material coordinate system

$$\left\{\varepsilon^T\right\}_1 = \left\{\alpha\right\}_1 \Delta T \tag{3.39}$$

In global coordinate system

$$\left\{\varepsilon^T\right\}_x = \left[T_2\right]^{-1} \left\{\varepsilon^T\right\}_1 \tag{3.40}$$

and combined

$$\left\{\varepsilon^T\right\}_x = \left[T_2\right]^{-1} \left\{\alpha\right\}_1 \Delta T \tag{3.41}$$

It is clear that we can transform α from material coordinate system to global coordinate system.

$$\begin{Bmatrix} \alpha_x \\ \alpha_y \\ \alpha_z \\ 0 \\ 0 \\ \alpha_{xy} \end{Bmatrix}_x = \left[T_2\right]^{-1} \begin{Bmatrix} \alpha_1 \\ \alpha_2 \\ \alpha_3 \\ 0 \\ 0 \\ 0 \end{Bmatrix}_1 \tag{3.42}$$

In explicit form,

$$\begin{aligned} \alpha_x &= c^2\alpha_1 + s^2\alpha_2 \\ \alpha_y &= s^2\alpha_1 + c^2\alpha_2 \\ \alpha_z &= \alpha_3 \\ \alpha_{xy} &= 2cs(\alpha_1 - \alpha_2) \end{aligned} \tag{3.43}$$

3.6.1 Constitutive Equation whit thermal effects

The total strain in a thermo-elastic analysis is the sum of the thermal strain due by the CTEs and the elastic strain due by the compliance/stiffness matrix. So

$$\left\{\varepsilon\right\} = \left\{\varepsilon^\sigma\right\} + \left\{\varepsilon^T\right\} \tag{3.44}$$

then

$$\{\varepsilon\} = [S]\{\sigma\} + \{\varepsilon^T\} \tag{3.45}$$

And inverting the previous equation, the σ becomes

$$\{\sigma\} = [C](\{\varepsilon\} - \{\varepsilon^T\}) \tag{3.46}$$

This relations can be written in explicit/matrix form in global coordinate system

$$\begin{Bmatrix} \sigma_x \\ \sigma_y \\ \sigma_z \\ \tau_{yz} \\ \tau_{xz} \\ \tau_{xy} \end{Bmatrix} = \begin{bmatrix} c^2 & s^2 & 0 & 0 & 0 & 2cs \\ s^2 & c^2 & 0 & 0 & 0 & -2cs \\ 0 & 0 & 1 & 0 & 0 & 0 \\ 0 & 0 & 0 & c & -s & 0 \\ 0 & 0 & 0 & s & c & 0 \\ -cs & cs & 0 & 0 & 0 & c^2 - s^2 \end{bmatrix} \begin{Bmatrix} \varepsilon_x - \varepsilon_x^T \\ \varepsilon_y - \varepsilon_y^T \\ \varepsilon_z - \varepsilon_z^T \\ \gamma_{yz} \\ \gamma_{xz} \\ \gamma_{xy} - \gamma_{xy}^T \end{Bmatrix} \tag{3.47}$$

3.7 Appendix: Matlab Code

```
clear all
close all
clc

E1  = 121000; % MPa
E2  = 8600;   % MPa
E3  = 8600;   % MPa
G12 = 4700;   % MPa
v12 = 0.27;
v23 = 0.40;

n = 1000;

ang = linspace(-90*pi/180,90*pi/180,n);

 S  =     [1/E1    -v12/E1 -v12/E1  0                  0       0;
          -v12/E1   1/E2    -v23/E2  0                  0       0;
          -v12/E1  -v23/E2   1/E3    0                  0       0;
             0        0        0    2*((1+v23)/(E2))   0       0;
             0        0        0     0                1/G12    0;
             0        0        0     0                 0     1/G12];

 C  = inv(S);
```

```
24
25
26  for i=1:n
27      c(i)  = cos(ang(i));
28      c2(i) = c(i)^2;
29      s(i)  = sin(ang(i));
30      s2(i) = s(i)^2;
31  end
32  for i=1:n
33  a(i).T1 = [c2(i) s2(i) 0 0 0 2*c(i)*s(i);
34         s2(i) c2(i) 0 0 0 -2*c(i)*s(i);
35         0 0 1 0 0 0;
36         0 0 0 c(i) -s(i) 0;
37         0 0 0 s(i) c(i) 0;
38         -c(i)*s(i) c(i)*s(i) 0 0 0 c2(i)-s2(i)];
39
40  a(i).T2 = [c2(i) s2(i) 0 0 0 c(i)*s(i);
41         s2(i) c2(i) 0 0 0 -c(i)*s(i);
42         0 0 1 0 0 0;
43         0 0 0 c(i) -s(i) 0;
44         0 0 0 s(i) c(i) 0;
45         -2*c(i)*s(i) 2*c(i)*s(i) 0 0 0 c2(i)-s2(i)];
46  end
47
48  for i=1:n
49    a(i).Ss=inv(a(i).T2)*S*a(i).T1;
50    a(i).Cc=inv(a(i).T1)*C*a(i).T2;
51  end
52
53  ang = linspace(-90,90,n);
54  ang=ang.';
55
56  for i=1:n
57      Cc11(i,1) = a(i).Cc(1,1);
58      Cc22(i,1) = a(i).Cc(2,2);
59      Cc44(i,1) = a(i).Cc(4,4);
60      Cc66(i,1) = a(i).Cc(6,6);
61      Cc12(i,1) = a(i).Cc(1,2);
62      Cc13(i,1) = a(i).Cc(1,3);
63      Cc23(i,1) = a(i).Cc(2,3);
```

```
64        Cc45(i,1) = a(i).Cc(4,5);
65        Cc16(i,1) = a(i).Cc(1,6);
66        Cc26(i,1) = a(i).Cc(2,6);
67        Cc36(i,1) = a(i).Cc(3,6);
68
69        Ss11(i,1) = a(i).Ss(1,1);
70        Ss22(i,1) = a(i).Ss(2,2);
71        Ss44(i,1) = a(i).Ss(4,4);
72        Ss66(i,1) = a(i).Ss(6,6);
73        Ss12(i,1) = a(i).Ss(1,2);
74        Ss13(i,1) = a(i).Ss(1,3);
75        Ss23(i,1) = a(i).Ss(2,3);
76        Ss45(i,1) = a(i).Ss(4,5);
77        Ss16(i,1) = a(i).Ss(1,6);
78        Ss26(i,1) = a(i).Ss(2,6);
79        Ss36(i,1) = a(i).Ss(3,6);
80    end
81
82  Cc(:,1)=Cc11(:,1);
83  Cc(:,2)=Cc22(:,1);
84  Cc(:,3)=Cc44(:,1);
85  Cc(:,4)=Cc66(:,1);
86  Cc(:,5)=Cc12(:,1);
87  Cc(:,6)=Cc13(:,1);
88  Cc(:,7)=Cc23(:,1);
89  Cc(:,8)=Cc45(:,1);
90  Cc(:,9)=Cc16(:,1);
91  Cc(:,10)=Cc26(:,1);
92  Cc(:,11)=Cc36(:,1);
93
94  Ss(:,1)=Ss11(:,1);
95  Ss(:,2)=Ss22(:,1);
96  Ss(:,3)=Ss44(:,1);
97  Ss(:,4)=Ss66(:,1);
98  Ss(:,5)=Ss12(:,1);
99  Ss(:,6)=Ss13(:,1);
100 Ss(:,7)=Ss23(:,1);
101 Ss(:,8)=Ss45(:,1);
102 Ss(:,9)=Ss16(:,1);
103 Ss(:,10)=Ss26(:,1);
```

```
104 Ss(:,11)=Ss36(:,1);
```

Table 3.1: Mechanical properties of Epoxy Carbon UD (230 GPa) Prepreg

Density		1.49	[g/cm3]
Coefficient of Thermal Expansion	Direction X	-4.70E-07	[1/°C]
	Direction Y	3.00E-05	[1/°C]
	Direction Z	3.00E-05	[1/°C]
Orthotropic Elasticity	Young's Modulus X	121000	[Mpa]
	Young's Modulus Y	8600	[Mpa]
	Young's Modulus Z	8600	[Mpa]
	Poisson's Ratio XY	0.27	
	Poisson's Ratio YZ	0.40	
	Poisson's Ratio XZ	0.27	
	Shear Modulus XY	4700	[Mpa]
	Shear Modulus YZ	3100	[Mpa]
	Shear Modulus XZ	4700	[Mpa]
Stress Limits	Tensile X	2231	[Mpa]
	Tensile Y	29	[Mpa]
	Tensile Z	29	[Mpa]
	Compressive X	-1082	[Mpa]
	Compressive Y	-100	[Mpa]
	Compressive Z	-100	[Mpa]
	Shear XY	60	[Mpa]
	Shear YZ	32	[Mpa]
	Shear XZ	60	[Mpa]
Strain Limits	Tensile X	0.0167	
	Tensile Y	0.0032	
	Tensile Z	0.0032	
	Compressive X	-0.0108	
	Compressive Y	-0.0192	
	Compressive Z	-0.0192	
	Shear XY	0.0120	
	Shear YZ	0.0110	
	Shear XZ	0.0120	

Chapter 4

Theory of Lamination

4.1 Introduction to plane-stress state

Plane stress condition is often used in analysis and design of composite material components because is a simplified form of 3D state and a very good approximation. It is possible to start from the constitutive equation, in particular from the compliance matrix expressed in global coordinate system 3.36.

$$\left[\bar{S}\right] = \begin{bmatrix} \bar{S}_{11} & \bar{S}_{21} & \bar{S}_{31} & 0 & 0 & \bar{S}_{61} \\ \bar{S}_{12} & \bar{S}_{22} & \bar{S}_{32} & 0 & 0 & \bar{S}_{62} \\ \bar{S}_{13} & \bar{S}_{23} & \bar{S}_{33} & 0 & 0 & \bar{S}_{63} \\ 0 & 0 & 0 & \bar{S}_{44} & \bar{S}_{54} & 0 \\ 0 & 0 & 0 & \bar{S}_{45} & \bar{S}_{55} & 0 \\ \bar{S}_{16} & \bar{S}_{26} & \bar{S}_{36} & 0 & 0 & \bar{S}_{66} \end{bmatrix} \tag{4.1}$$

In plane-stress state, some stresses are equal to zero by definition: $\sigma_z = \tau_{yz} = \tau_{zx} = 0$, consequently the strains

$$\begin{aligned} \gamma_{yz} &= \bar{S}_{44}\tau_{yz} + \bar{S}_{45}\tau_{zx} = 0 \\ \gamma_{zx} &= \bar{S}_{44}\tau_{yz} + \bar{S}_{55}\tau_{zx} = 0 \\ \varepsilon_z &= \bar{S}_{13}\sigma_x + \bar{S}_{23}\sigma_y + \bar{S}_{36}\tau_{xy} \end{aligned} \tag{4.2}$$

For these reasons the constitutive equation expressed in global coordinate system

$$\begin{Bmatrix} \varepsilon_x \\ \varepsilon_y \\ \varepsilon_z \\ \gamma_{yz} \\ \gamma_{zx} \\ \gamma_{xy} \end{Bmatrix} = \begin{bmatrix} \bar{S}_{11} & \bar{S}_{21} & \bar{S}_{31} & 0 & 0 & \bar{S}_{61} \\ \bar{S}_{12} & \bar{S}_{22} & \bar{S}_{32} & 0 & 0 & \bar{S}_{62} \\ \bar{S}_{13} & \bar{S}_{23} & \bar{S}_{33} & 0 & 0 & \bar{S}_{63} \\ 0 & 0 & 0 & \bar{S}_{44} & \bar{S}_{54} & 0 \\ 0 & 0 & 0 & \bar{S}_{45} & \bar{S}_{55} & 0 \\ \bar{S}_{16} & \bar{S}_{26} & \bar{S}_{36} & 0 & 0 & \bar{S}_{66} \end{bmatrix} \begin{Bmatrix} \sigma_x \\ \sigma_y \\ \sigma_z \\ \tau_{yz} \\ \tau_{zx} \\ \tau_{xy} \end{Bmatrix} \tag{4.3}$$

became

$$\begin{Bmatrix} \varepsilon_x \\ \varepsilon_y \\ \varepsilon_z \\ \gamma_{yz} \\ \gamma_{zx} \\ \gamma_{xy} \end{Bmatrix} = \begin{bmatrix} \bar{S}_{11} & \bar{S}_{21} & \bar{S}_{31} & 0 & 0 & \bar{S}_{61} \\ \bar{S}_{12} & \bar{S}_{22} & \bar{S}_{32} & 0 & 0 & \bar{S}_{62} \\ \bar{S}_{13} & \bar{S}_{23} & \bar{S}_{33} & 0 & 0 & \bar{S}_{63} \\ 0 & 0 & 0 & \bar{S}_{44} & \bar{S}_{54} & 0 \\ 0 & 0 & 0 & \bar{S}_{45} & \bar{S}_{55} & 0 \\ \bar{S}_{16} & \bar{S}_{26} & \bar{S}_{36} & 0 & 0 & \bar{S}_{66} \end{bmatrix} \begin{Bmatrix} \sigma_x \\ \sigma_y \\ 0 \\ 0 \\ 0 \\ \tau_{xy} \end{Bmatrix} \tag{4.4}$$

and in contracted form (also called 2D form o plane-stress constitutive equation)

$$\begin{Bmatrix} \varepsilon_x \\ \varepsilon_y \\ \gamma_{xy} \end{Bmatrix} = \begin{bmatrix} \bar{S}_{11} & \bar{S}_{21} & \bar{S}_{61} \\ \bar{S}_{12} & \bar{S}_{22} & \bar{S}_{62} \\ \bar{S}_{16} & \bar{S}_{26} & \bar{S}_{66} \end{bmatrix} \begin{Bmatrix} \sigma_x \\ \sigma_y \\ \tau_{xy} \end{Bmatrix} \tag{4.5}$$

The out-of-plane strain ε_z can be expressed in terms of in-plane strain so, once the in-plane problem is solved, also out-of-plane strains γ_{yz} and γ_{zx} can be determinated. Compliance matrix in plane-stress condition can be also expressed in the same way. It can be noticed that $[\bar{Q}_{ij}]$ terms are different and are not corresponding terms $[\bar{C}_{ij}]$ taken from the global 3D stiffness matrix.

$$\begin{Bmatrix} \sigma_x \\ \sigma_y \\ \tau_{xy} \end{Bmatrix} = \begin{bmatrix} \bar{Q}_{11} & \bar{Q}_{21} & \bar{Q}_{61} \\ \bar{Q}_{12} & \bar{Q}_{22} & \bar{Q}_{62} \\ \bar{Q}_{16} & \bar{Q}_{26} & \bar{Q}_{66} \end{bmatrix} \begin{Bmatrix} \varepsilon_x \\ \varepsilon_y \\ \gamma_{xy} \end{Bmatrix} \tag{4.6}$$

4.2 Coordinate transformation

Starting from a general material in plane-stress condition and material coordinate system

$$\begin{Bmatrix} \varepsilon_1 \\ \varepsilon_2 \\ \gamma_{12} \end{Bmatrix}_1 = \begin{bmatrix} S_{11} & S_{21} & S_{61} \\ S_{12} & S_{22} & S_{62} \\ S_{16} & S_{26} & S_{66} \end{bmatrix} \begin{Bmatrix} \sigma_1 \\ \sigma_2 \\ \tau_{12} \end{Bmatrix}_1 \tag{4.7}$$

$$\begin{Bmatrix} \sigma_1 \\ \sigma_2 \\ \tau_{12} \end{Bmatrix}_1 = \begin{bmatrix} Q_{11} & Q_{21} & Q_{61} \\ Q_{12} & Q_{22} & Q_{62} \\ Q_{16} & Q_{26} & Q_{66} \end{bmatrix} \begin{Bmatrix} \varepsilon_1 \\ \varepsilon_2 \\ \gamma_{12} \end{Bmatrix}_1 \tag{4.8}$$

the Equations 4.7 and 4.8 could be written in material coordinates for an orthotropic material in the same plane-stress condition

$$\begin{Bmatrix} \varepsilon_1 \\ \varepsilon_2 \\ \gamma_{12} \end{Bmatrix}_1 = \begin{bmatrix} S_{11} & S_{21} & 0 \\ S_{12} & S_{22} & 0 \\ 0 & 0 & S_{66} \end{bmatrix} \begin{Bmatrix} \sigma_1 \\ \sigma_2 \\ \tau_{12} \end{Bmatrix}_1 \tag{4.9}$$

$$\begin{Bmatrix} \sigma_1 \\ \sigma_2 \\ \tau_{12} \end{Bmatrix}_1 = \begin{bmatrix} Q_{11} & Q_{21} & 0 \\ Q_{12} & Q_{22} & 0 \\ 0 & 0 & Q_{66} \end{bmatrix} \begin{Bmatrix} \varepsilon_1 \\ \varepsilon_2 \\ \gamma_{12} \end{Bmatrix}_1 \tag{4.10}$$

As shown in Section 3.4, the most common 2D transformation is the rotation about the z axis. So it is possible to write the equivalent transformation/rotation matrix for stress $[T_1]$ and $[T_2]$ strain respectively to change the coordinate system from material to global.

$$\begin{Bmatrix} \sigma_1 \\ \sigma_2 \\ \tau_{12} \end{Bmatrix}_1 = \big[T_1\big] \begin{Bmatrix} \sigma_1 \\ \sigma_2 \\ \tau_{12} \end{Bmatrix}_x \tag{4.11}$$

$$\begin{Bmatrix} \varepsilon_1 \\ \varepsilon_2 \\ \gamma_{12} \end{Bmatrix}_1 = \big[T_2\big] \begin{Bmatrix} \varepsilon_1 \\ \varepsilon_2 \\ \gamma_{12} \end{Bmatrix}_x \tag{4.12}$$

defining $c = \cos\theta$ and $s = \sin\theta$, the transformation matrix

$$\big[T_1\big] = \begin{bmatrix} c^2 & s^2 & 2cs \\ s^2 & c^2 & -2cs \\ -cs & cs & c^2 - s^2 \end{bmatrix} \tag{4.13}$$

$$\big[T_2\big] = \begin{bmatrix} c^2 & s^2 & cs \\ s^2 & c^2 & -cs \\ -2cs & 2cs & c^2 - s^2 \end{bmatrix} \tag{4.14}$$

The rotation matrices (T_1 and T_2) are different by only two terms. It can be notice that $[T_1(\theta)]^{-1} = [T_1(-\theta)]$ and $[T_2(\theta)]^{-1} = [T_2(-\theta)]$. From the previous relations

$$\begin{Bmatrix} \sigma_1 \\ \sigma_2 \\ \tau_{12} \end{Bmatrix}_x = \big[T_1\big]^{-1} \big[Q\big] \big[T_2\big] \begin{Bmatrix} \varepsilon_1 \\ \varepsilon_2 \\ \gamma_{12} \end{Bmatrix}_x \tag{4.15}$$

and defining the plane-stress transofrmed 2D reduced stiffness matrix $[\bar{Q}]$ as

$$\big[\bar{Q}\big] = \big[T_1\big]^{-1} \big[Q\big] \big[T_2\big] \tag{4.16}$$

and the constitutive equation in global coordinate system

$$\begin{Bmatrix} \sigma_1 \\ \sigma_2 \\ \tau_{12} \end{Bmatrix}_x = \begin{bmatrix} \bar{Q}_{11} & \bar{Q}_{21} & 0 \\ \bar{Q}_{12} & \bar{Q}_{22} & 0 \\ 0 & 0 & \bar{Q}_{66} \end{bmatrix} \begin{Bmatrix} \varepsilon_1 \\ \varepsilon_2 \\ \gamma_{12} \end{Bmatrix}_x \tag{4.17}$$

The ij terms of $[\bar{Q}]$ in extended form

$$\begin{aligned}
\bar{Q}_{11} &= Q_{11}c^4 + 2(Q_{12} + 2Q_{66})c^2s^2 + Q_{22}s^4 \\
\bar{Q}_{12} &= (Q_{11} + Q_{22} - 4Q_{66})c^2s^2 + Q_{12}(s^4 + c^4) \\
\bar{Q}_{22} &= Q_{11}s^4 + 2(Q_{12} + 2Q_{66})c^2s^2 + Q_{22}c^4 \\
\bar{Q}_{16} &= (Q_{11} - Q_{12} - 2Q_{66})c^3s + (Q_{12} - Q_{22} + 2Q_{66})s^3c \\
\bar{Q}_{26} &= (Q_{11} - Q_{12} - 2Q_{66})cs^3 + (Q_{12} - Q_{22} + 2Q_{66})sc^3 \\
\bar{Q}_{66} &= (Q_{11} + Q_{22} - 2Q_{12} - 2Q_{66})c^2s^2 + Q_{66}(s^4 + c^4)
\end{aligned} \tag{4.18}$$

In the same way

$$\left[\bar{S}\right] = \left[T_2\right]^{-1}\left[S\right]^{-1}\left[T_1\right] \tag{4.19}$$

The ij terms of $[\bar{S}]$ in extended form

$$\begin{aligned}
\bar{S}_{11} &= c^4S_{11} + c^2s^2(2S_{12} + S_{66}) + c^4S_{22} \\
\bar{S}_{12} &= s^2c^2(S_{11} + S_{22} - S_{66}) + (s^4 - c^4)S_{12} \\
\bar{S}_{22} &= s^4S_{11} + c^2s^2(2S_{12} + S_{66}) + c^4S_{22} \\
\bar{S}_{16} &= sc(c^2(2S_{11} - 2S_{12} - S_{66}) + s^2(2S_{12} - 2S_{22} + S_{66})) \\
\bar{S}_{26} &= sc(s^2(2S_{11} - 2S_{12} - S_{66}) + c^2(2S_{12} - 2S_{22} + S_{66})) \\
\bar{S}_{66} &= 4s^2c^2(S_{11} - 2S_{12} + S_{22}) + (s^2 - c^2)^2S_{66}
\end{aligned} \tag{4.20}$$

The relation $[\bar{S}] = [\bar{Q}]^{-1}$ in 2D plane stress condition is the same of 3D one.

4.3 Fundamental concepts

The lamination theory for composite materials was presented in early 1960 [23, 24, 25] and later refined by numerous studies. The theory and analysis presented, follow the clearest one (for the author) shown by Herakovich in 1992 [12]. In this Chapter, the equations describe the linear-elastic response of a plate made in transversely isotropic materials, with different angles of the single lamina, in the global coordinate system in plane-stress condition. Matlab code will follow the present theory to develop a simple software for lamination calculation.

4.3.1 Notation

In this Chapter, the global x-y-z coordinate system is taken according to Herakovich [12], with z positive downward and perpendicular respect the plane of the laminate. The axis origin is located in half of the thickness on the midplane of the laminate, as depicted in Figure 4.1. Each ply has a different fibers orientation

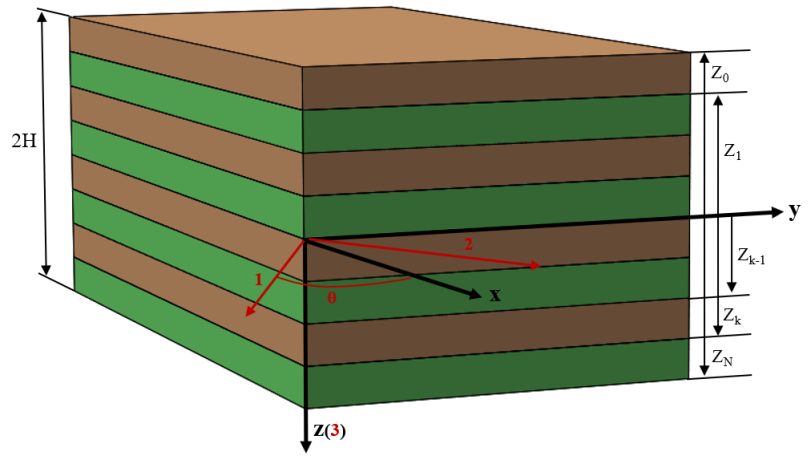

Figure 4.1: Composite laminate with coordinates in both global and ply coordinate system.

θ_k respect x axis (Figure 4.1) and each k layer has a thickness t_k which is determined by the position on z axis ($t_k = z_k - z_{k-1}$). The sum of each layer thickness is the total thickness of the laminate denominated $2H$. Some assumptions are fundamental in this theory:

- Every layer is a homogeneous material
- Every layer is isotropic or orthotropic or transversely isotropic.
- The system is in a plane stress condition.
- Every layer is perfectly bonded in the laminate.
- The midplane normals remain straight and normal after the deformation due to a load condition.
- Normals to midplane do not change length [26, 27].

In matrix form, the planar strain can be combined in strain-displacement equations.

$$\begin{Bmatrix} \varepsilon_x \\ \varepsilon_y \\ \varepsilon_z \end{Bmatrix} = \begin{Bmatrix} \varepsilon_x^0 \\ \varepsilon_y^0 \\ \gamma_{xy}^0 \end{Bmatrix} + z \begin{Bmatrix} k_x \\ k_y \\ k_{xy} \end{Bmatrix} \tag{4.21}$$

or in compact form

$$\left\{\varepsilon\right\}_x = \left\{\varepsilon^0\right\}_x + z \left\{k\right\}_x \tag{4.22}$$

where the curvature k are defined starting from the relation between displacement and strain-displacement equation in global coordinate system. The planar strains:

$$\begin{aligned} \varepsilon_x &= \frac{\partial u}{\partial x} = \frac{\partial u^0}{\partial x} - z\frac{\partial^2 w}{\partial x^2} = \varepsilon_x^0 + zk_x \\ \varepsilon_y &= \frac{\partial v}{\partial y} = \frac{\partial v^0}{\partial y} - z\frac{\partial^2 w}{\partial y^2} = \varepsilon_y^0 + zk_y \\ \gamma_{xy} &= (\frac{\partial u}{\partial x} + \frac{\partial v}{\partial y}) = \frac{\partial u^0}{\partial x} - 2z\frac{\partial^2 w}{\partial x \partial y} = \gamma_{xy}^0 + zk_{xy} \end{aligned} \tag{4.23}$$

and from Equation 4.23 the curvature can be defined as

$$\begin{aligned} k_x &= -\frac{\partial^2 w}{\partial x^2} \\ k_y &= -\frac{\partial^2 w}{\partial y^2} \\ k_{xy} &= -2z\frac{\partial^2 w}{\partial x \partial y} \end{aligned} \tag{4.24}$$

4.3.2 Stresses

Substituting the strain (Equation 4.24) into the plane stress constitutive equation (Equation 4.17), the stresses at any *z-position* of laminate location can be simply determined. The results can be express as

$$\left\{\sigma\right\}_x = \left[\bar{Q}\right]^k \left\{\varepsilon\right\}_x \tag{4.25}$$

In Equation 4.25 the $[\bar{Q}]^k$ is the matrix of transformed reduced stiffness in plane-stress condition of the kth ply in z-location. This matrix varies with the ply (fibers) orientation. The combination given by Equation 4.22 and Equation 4.25 gives, for a general z-location throughout the thickness, a general expression for the stresses of the kth ply of the laminate.

$$\left\{\sigma\right\}^k = \left[\bar{Q}\right]^k \left\{\varepsilon^0\right\} + \left[\bar{Q}\right]^k z \left\{k\right\} \tag{4.26}$$

4.3.3 Force in-plane

The integral through the thickness of the planar stresses in the laminate gives the in-plane forces per unit length. Thus

$$\begin{aligned} N_x &= \int_{-H}^{H} \sigma_x dz \\ N_y &= \int_{-H}^{H} \sigma_y dz \\ N_{xy} &= \int_{-H}^{H} \tau_{xy} dz \end{aligned} \tag{4.27}$$

in contracted form

$$\left\{N\right\} = \int_{-H}^{H} \left\{\sigma\right\} dz \tag{4.28}$$

The combination of Equation 4.26 with the explicit form of Equation 4.28, gives

$$\left\{N\right\} = \int_{-H}^{H} \left[\bar{Q}\right]^k \left\{\varepsilon^0\right\} dz + \int_{-H}^{H} \left[\bar{Q}\right]^k \left\{k\right\} z dz \tag{4.29}$$

The midplane strains ($\left\{\varepsilon^0\right\}$) and the curvature ($\left\{k\right\}$) are indipendent of z and the the sum of the contributes of each ply can be expressed as a summation of integrals over the thickness.

$$\left\{N\right\} = \sum_{k=1}^{N} \left(\int_{-H}^{H} \left[\bar{Q}\right]^k dz\right) \left\{\varepsilon^0\right\} + \sum_{k=1}^{N} \left(\int_{-H}^{H} \left[\bar{Q}\right]^k z dz\right) \left\{k\right\} \tag{4.30}$$

The previous Equation 4.30 can be written as

$$\left\{N\right\} = \left[A\right] \left\{\varepsilon^0\right\} + \left[B\right] \left\{k\right\} \tag{4.31}$$

where $[A]$ and $[B]$ are defined as summations, in matrix form, for all N plys,

$$\begin{aligned} \left[A\right] &= \sum_{k=1}^{N} \left[\bar{Q}\right]^k (z_k - z_{k-1}) \\ \left[B\right] &= \frac{1}{2} \sum_{k=1}^{N} \left[\bar{Q}\right]^k (z_k^2 - z_{k-1}^2) \end{aligned} \tag{4.32}$$

4.3.4 Moments

As defined for in-plane forces in Equation 4.27, the Moments fer unit-length can be defined. Thus

$$\begin{aligned} M_x &= \int_{-H}^{H} \sigma_x z dz \\ M_y &= \int_{-H}^{H} \sigma_y z dz \\ M_{xy} &= \int_{-H}^{H} \tau_{xy} z dz \end{aligned} \tag{4.33}$$

and in contracted form

$$\{M\} = \int_{-H}^{H} \{\sigma\} z dz \tag{4.34}$$

As shown before, substituting the Equation 4.34 in 4.26 gives the expression of Moments

$$\{M\} = [B] \{\varepsilon^0\} + [D] \{k\} \tag{4.35}$$

and the stiffness matrix $[D]$ in sum form is

$$[D] = \frac{1}{3} \sum_{k=1}^{N} [\bar{Q}]^k (z_k^3 - z_{k-1}^3) \tag{4.36}$$

4.4 Constitutive laminate matrix relations

The matrices $[A]$, $[B]$ and $[D]$ are defined as

$$\begin{aligned} [A] &= \sum_{k=1}^{N} [\bar{Q}]^k (z_k - z_{k-1}) \\ [B] &= \frac{1}{2} \sum_{k=1}^{N} [\bar{Q}]^k (z_k^2 - z_{k-1}^2) \\ [D] &= \frac{1}{3} \sum_{k=1}^{N} [\bar{Q}]^k (z_k^3 - z_{k-1}^3) \end{aligned} \tag{4.37}$$

and

$$\begin{aligned} \{N\} &= [A] \{\varepsilon^0\} + [B] \{k\} \\ \{M\} &= [B] \{\varepsilon^0\} + [D] \{k\} \end{aligned} \tag{4.38}$$

The Equation 4.37 and 4.38 can be combined in matrix notation as

$$\begin{Bmatrix} N \\ M \end{Bmatrix} = \begin{bmatrix} A & B \\ B & D \end{bmatrix} \begin{Bmatrix} \varepsilon^0 \\ k \end{Bmatrix} \tag{4.39}$$

and in explicit form

$$\begin{Bmatrix} N_x \\ N_y \\ N_{xy} \\ M_x \\ M_y \\ M_{xy} \end{Bmatrix} = \begin{bmatrix} A_{11} & A_{21} & A_{16} & B_{11} & B_{21} & B_{16} \\ A_{12} & A_{22} & A_{26} & B_{12} & B_{22} & B_{26} \\ A_{16} & A_{26} & A_{66} & B_{16} & B_{26} & B_{66} \\ B_{11} & B_{21} & B_{16} & D_{11} & D_{21} & D_{16} \\ B_{12} & B_{22} & B_{26} & D_{12} & D_{22} & D_{26} \\ B_{16} & B_{26} & B_{66} & D_{16} & D_{26} & D_{66} \end{bmatrix} \begin{Bmatrix} \varepsilon_x^0 \\ \varepsilon_y^0 \\ \gamma_{xy}^0 \\ k_x \\ k_y \\ k_{xy} \end{Bmatrix} \tag{4.40}$$

The matrix in Equation 4.40 can be inverted to expose the strain in function of the loads. It can define

$$\begin{Bmatrix} \varepsilon_x^0 \\ \varepsilon_y^0 \\ \gamma_{xy}^0 \\ k_x \\ k_y \\ k_{xy} \end{Bmatrix} = \begin{bmatrix} A'_{11} & A'_{21} & A'_{16} & B'_{11} & B'_{21} & B'_{16} \\ A'_{12} & A'_{22} & A'_{26} & B'_{12} & B'_{22} & B'_{26} \\ A'_{16} & A'_{26} & A'_{66} & B'_{16} & B'_{26} & B'_{66} \\ C'_{11} & C'_{21} & C'_{16} & D'_{11} & D'_{21} & D'_{16} \\ C'_{12} & C'_{22} & C'_{26} & D'_{12} & D'_{22} & D'_{26} \\ C'_{16} & C'_{26} & C'_{66} & D'_{16} & D'_{26} & D'_{66} \end{bmatrix} \begin{Bmatrix} N_x \\ N_y \\ N_{xy} \\ M_x \\ M_y \\ M_{xy} \end{Bmatrix} \tag{4.41}$$

where

$$\begin{aligned} \left[A'\right] &= \left[A\right]^{-1} + \left[A\right]^{-1}\left[B\right]\left(\left[D\right] - \left[B\right]\left[A\right]^{-1}\left[B\right]\right)^{-1}\left[B\right]\left[A\right]^{-1} \\ \left[B'\right] &= -\left[A\right]^{-1}\left[B\right]\left(\left[D\right] - \left[B\right]\left[A\right]^{-1}\left[B\right]\right)^{-1} \\ \left[C'\right] &= -\left(\left[D\right] - \left[B\right]\left[A\right]^{-1}\left[B\right]\right)^{-1}\left[B\right]\left[A\right]^{-1} \\ \left[D'\right] &= \left(\left[D\right] - \left[B\right]\left[A\right]^{-1}\left[B\right]\right)^{-1} \end{aligned} \tag{4.42}$$

The matrix $[C'] = [B']^T$ but $[B']^T = [B']$ so finally

$$\begin{Bmatrix} \varepsilon_x^0 \\ \varepsilon_y^0 \\ \gamma_{xy}^0 \\ k_x \\ k_y \\ k_{xy} \end{Bmatrix} = \begin{bmatrix} A'_{11} & A'_{21} & A'_{16} & B'_{11} & B'_{21} & B'_{16} \\ A'_{12} & A'_{22} & A'_{26} & B'_{12} & B'_{22} & B'_{26} \\ A'_{16} & A'_{26} & A'_{66} & B'_{16} & B'_{26} & B'_{66} \\ B'_{11} & B'_{21} & B'_{16} & D'_{11} & D'_{21} & D'_{16} \\ B'_{12} & B'_{22} & B'_{26} & D'_{12} & D'_{22} & D'_{26} \\ B'_{16} & B'_{26} & B'_{66} & D'_{16} & D'_{26} & D'_{66} \end{bmatrix} \begin{Bmatrix} N_x \\ N_y \\ N_{xy} \\ M_x \\ M_y \\ M_{xy} \end{Bmatrix} \tag{4.43}$$

4.5 Engineering Constants of a generic Laminate

For convenience, the mechanical characteristics of a generic laminate are often expressed in terms of Engineering Constants. In this case, the laminate is treated as if it were made of a single material with equivalent mechanical characteristics. Now, the main purpose of classical theory is that of giving a law capable of simulating the behavior of the multilayer laminate as if it were made up of just one

layer, having the total thickness of the laminate. Since now there is a homogeneous monolithic layer, in general anisotropic, the equivalent elastic characteristics are found starting from the normalized stiffness tensors

$$\begin{aligned} \left[a^*\right] &= h\left[A'\right] \\ \left[b^*\right] &= \frac{h^2}{2}\left[B'\right] \\ \left[d^*\right] &= \frac{h^3}{12}\left[D'\right] \end{aligned} \tag{4.44}$$

Generally, a^* is different from d^*, which means that in reality is as if the equivalent monolayer consisted of two different materials, one for membrane behavior and one for bending. A plate can be orthotropic in the membrane and bending, but with rotated orthotropic axes. Or a laminate can be isotropic in the membrane and completely anisotropic in bending. Moreover, the value of the stiffness components of the fictitious materials is different. This means that the same specimen obtained from a laminate subjected to laboratory tests will show values differently, such as the equivalent Young modulus, in a three-point bending test, and in a traction one.

Therefore, the decoupled Engineering Constants can be derived, one for the membrane (m) behavior and one for the flexural/bending one (f).

$$\begin{aligned} E_x^m &= \frac{1}{a_{11}^*} \\ E_y^m &= \frac{1}{a_{22}^*} \\ G_{xy}^m &= \frac{1}{a_{66}^*} \\ \nu_x^m &= -\frac{a_{12}^*}{a_{11}^*} \end{aligned} \tag{4.45}$$

and

$$\begin{aligned} E_x^f &= \frac{1}{d_{11}^*} \\ E_y^f &= \frac{1}{d_{22}^*} \\ G_{xy}^f &= \frac{1}{d_{66}^*} \\ \nu_x^f &= -\frac{d_{12}^*}{d_{11}^*} \end{aligned} \tag{4.46}$$

4.6 Appendix: Matlab Code

In this section, an example of MATLAB function for the calculation of laminate properties is reported. In particular, the function *lamination* has the structure *HT* (ply properties) and *n* (number of plies) as inputs. The output is *W*, the final laminate matrix.

```
function [W] = lamination(HT,n)
    H = 0;
    for i=1:n
        H = H + HT(n).h;
    end
    H  = H/2; % half of thickness
    H2 = H*2;

    z = zeros(1,n+1);
    z(1) = -H;
    for i=2:n+1
        z(i) = z(i-1) + HT(n).h;
    end

    %-----------------------------------------------------------
    W.A = zeros(3);
    W.B = zeros(3);
    W.D = zeros(3);

    for i=2:n+1
        W.A = W.A + HT(n-1).K2r*(z(n)-z(n-1));
        W.B = W.B + HT(n-1).K2r*(((z(n))^2 - (z(n-1))^2)/2)
            ;
        W.D = W.D + HT(n-1).K2r*(((z(n))^3 - (z(n-1))^3)/3)
            ;
    end
    %-----------------------------------------------------------

    W.KK = [W.A(1,1)  W.A(1,2)  W.A(1,3)      W.B(1,1)  W.B
        (1,2)  W.B(1,3);
            W.A(2,1)  W.A(2,2)  W.A(2,3)      W.B(2,1)  W.B
                (2,2)  W.B(2,3);
            W.A(3,1)  W.A(3,2)  W.A(3,3)      W.B(3,1)  W.B
                (3,2)  W.B(3,3);
```

```
30
31              W.B(1,1)  W.B(1,2)  W.B(1,3)       W.D(1,1)  W.D
                    (1,2)  W.D(1,3);
32              W.B(2,1)  W.B(2,2)  W.B(2,3)       W.D(2,1)  W.D
                    (2,2)  W.D(2,3);
33              W.B(3,1)  W.B(3,2)  W.B(3,3)       W.D(3,1)  W.D
                    (3,2)  W.D(3,3)];
34
35
36      W.CC = inv(W.KK);
37
38      W.Aa = W.A   *   1/H2;
39      W.Ba = W.B   *   2/(H2^2);
40      W.Da = W.D   *   12/(H2^3);
41
42      W.Exm = 1/W.CC(1,1);
43      W.Efm = 1/W.CC(2,2);
44      W.Gxm = 1/W.CC(3,3);
45      W.Exf = 1/W.CC(4,4);
46      W.Eff = 1/W.CC(5,5);
47      W.Gxf = 1/W.CC(6,6);
48
49  end
```

Chapter 5

Micromechanics

5.1 Introduction

Micromechanics is the study of the composite at the fiber and matrix level. Micromechanics is important in predicting ply/lamina properties and performance, like elastic modulus, thermo-elastic properties, or, more recently, in failure behavior.

Many methods for the prediction of the performance of the lamina are available in literature. The earliest works started in early 1960 with Paul [28], Hashin [29, 30], Hill [31, 32] and Achenbach [33]. Based on a purely analytical approach, the first methods have been verified to date by other techniques based on numerical calculation, experimental, FEA, and nanomechanics.

This section focus on a small comparative overview of the best approaches, based on the review of Younes [34], which is an excellent starting point for identifying the best method to be used later in advanced computing systems.

5.2 Elasticity

For every analytical and numerical study of a composite product, especially in this work, it is important to predict the elastic properties of UD composite. UD laminas/plies are considered transverseley isotropic materials (see Section 3.2.1) and the compliance matrix is composed by only five indipendend constants: E_1, E_2, G_{12}, G_{23} (or ν_{23}) and ν_{12}. Therefore, it seems evident that it is necessary to find the best method or model to approximate the real performance of materials.

Example, for an orthotropic general material, the Compliance matrix is

$$\begin{Bmatrix} \varepsilon_1 \\ \varepsilon_2 \\ \varepsilon_3 \\ \gamma_{23} \\ \gamma_{13} \\ \gamma_{12} \end{Bmatrix} = \begin{bmatrix} \frac{1}{E_1} & \frac{-\nu_{21}}{E_2} & \frac{-\nu_{31}}{E_3} & 0 & 0 & 0 \\ \frac{-\nu_{12}}{E_1} & \frac{1}{E_2} & \frac{-\nu_{32}}{E_3} & 0 & 0 & 0 \\ \frac{-\nu_{13}}{E_1} & \frac{-\nu_{23}}{E_2} & \frac{1}{E_3} & 0 & 0 & 0 \\ 0 & 0 & 0 & \frac{1}{G_{23}} & 0 & 0 \\ 0 & 0 & 0 & 0 & \frac{1}{G_{13}} & 0 \\ 0 & 0 & 0 & 0 & 0 & \frac{1}{G_{12}} \end{bmatrix} \begin{Bmatrix} \sigma_1 \\ \sigma_2 \\ \sigma_3 \\ \tau_{23} \\ \tau_{13} \\ \tau_{12} \end{Bmatrix} \tag{5.1}$$

but for a general UD composite material, where $E_2 = E_3$, $\nu_{12} = \nu_{13}$, $G_{12} = G_{13}$, $G_{23} = \frac{E_2}{2(1+\nu 23)}$ Equation 5.1 simplifies to

$$\begin{Bmatrix} \varepsilon_1 \\ \varepsilon_2 \\ \varepsilon_3 \\ \gamma_{23} \\ \gamma_{13} \\ \gamma_{12} \end{Bmatrix} = \begin{bmatrix} \frac{1}{E_1} & \frac{-\nu_{12}}{E_1} & \frac{-\nu_{12}}{E_1} & 0 & 0 & 0 \\ \frac{-\nu_{12}}{E_1} & \frac{1}{E_2} & \frac{-\nu_{23}}{E_2} & 0 & 0 & 0 \\ \frac{-\nu_{12}}{E_1} & \frac{-\nu_{23}}{E_2} & \frac{1}{E_2} & 0 & 0 & 0 \\ 0 & 0 & 0 & \frac{2(1+\nu_{23})}{E_2} & 0 & 0 \\ 0 & 0 & 0 & 0 & \frac{1}{G_{12}} & 0 \\ 0 & 0 & 0 & 0 & 0 & \frac{1}{G_{12}} \end{bmatrix} \begin{Bmatrix} \sigma_1 \\ \sigma_2 \\ \sigma_3 \\ \tau_{23} \\ \tau_{13} \\ \tau_{12} \end{Bmatrix} \tag{5.2}$$

5.2.1 ROM: Rule of Mixture

The Rule of Mixture (ROM) is the most straightforward approach for UD calculation, and it is based on the Voigt (ROM) [35] and Reuss models (IROM) [36].

$$\begin{aligned} E_1 &= V^f E_1^f + V^m E^m \\ \nu_{12} &= V^f \nu_1^f + V^m \nu^m \\ E_2 &= \frac{E_2^f E^m}{E^m V^f + E_2^f V^m} \\ G_{12} &= \frac{G_{12}^f G^m}{G^m V^f + G_{12}^f V^m} \end{aligned} \tag{5.3}$$

Where the superscript f stand for *fiber* and m for *matrix*. V^f is the fibers volume (in percentage), and V^m the matrix one. The Voigt's and Reuss's model is a simple proportional approach between the fibers and matrix performance. It is in use for simple calculations.

In calculating of performance of materials at the industrial level, in this collaborative work with Reglass S.R.L., Only the E_1 and ν_{12} are taken from these methods. It is important to note that the most famous methods share the same formulation for E_{11} because it well predicts and fits the experimental results.

5.2.2 MROM: Modified Rule of Mixture

The MROM (Modified Rule of Mixture) is a semi-empirical model with the same formulation for E_1 and ν_{12} of the ROM model. Otherwise, for E_2 and G_{12}, some corrections factors η^f and η_m have been defined as

$$\begin{aligned} \eta^f &= \frac{E_1^f V^f + ((1-\nu_{12}^f\nu_{21}^f)E^m + \nu^m\nu_{21}^f E_1^f)V^m}{E_1^f V^f + E^m V^m} \\ \eta^m &= \frac{((1-\nu^{m^2})E_1^f - (1-\nu^m\nu_{12}^f)E^m)V^f + E^m V^m}{E_1^f V^f + E^m V^m} \end{aligned} \tag{5.4}$$

and, considering $0 < \eta' < 1$ (frequently taken $\eta' = 0.6$) it's possible to write two equation for E_2 and G_{12}

$$\begin{aligned} \frac{1}{E_2} &= \frac{\nu^f V^f}{E_2^f} + \frac{\nu^m V^m}{E^m} \\ \frac{1}{G_{12}} &= \frac{\frac{V^f}{G_{12}^f} + \frac{\nu' V^m}{G^m}}{V^f + \nu' V^m} \end{aligned} \tag{5.5}$$

5.2.3 Halpin-Tsai model

The Halpin-Tsai model [37] is also a semi-empirical model with the same formulation for E_1 and ν_{12} of ROM and MROM models. For the transversal, Young's modulus E_2 and G_{12} proposes a solution that approximates experimental data very well.

For the cases of this work (aligned long and continuous carbon fibers in CFRP), he defines a parameter

$$\begin{aligned} \zeta &= 2 + 40V_f^{10} \\ \eta &= \frac{\frac{E_1^f}{E^m} - 1}{\frac{E_1^f}{E^m} + \zeta} \end{aligned} \tag{5.6}$$

and so

$$\begin{aligned} E_2 &= \frac{E_1^f E^m}{V_1^f E^m + (1-V_f)E_1^f} \\ G_{12} &= G^m \frac{1+\zeta\eta V^f}{1-\eta V^f} \end{aligned} \tag{5.7}$$

5.2.4 Other models and towards a final formulation

For completeness also other more advanced models are introduced but not developed. They are mainly derived from experimental and numerical analyses. The most famous are the Chamis model [38], Hasin and Rosen model [30], Christensen model [39], Mori-Tanaka (MT) model [40] with Benveniste formulation [41], Hill model [32], Budianski model [42], Huang [43] and s. Li [44].

After many experiments conducted for this work based on the performance analysis of CFRP tubes made by Reglass S.R.L. and throughout the study of the literature, the best model for long aligned and continues fibers in CFRP is the Halpin-Tsai one [37] with the same formulation for E_1 and ν_{12} of ROM and MROM models.

Finally, the Elastic properties for defined ζ and η

$$\begin{aligned} \zeta &= 2 + 40V_f^{10} \\ \eta &= \frac{\frac{E_1^f}{E^m} - 1}{\frac{E_1^f}{E^m} + \zeta} \end{aligned} \tag{5.8}$$

are

$$\begin{aligned} E_1 &= V^f E_1^f + V^m E^m \\ E_2 &= \frac{E_1^f E^m}{V_1^f E^m + (1 - V_f) E_1^f} \\ E_3 &= E_2 \\ \nu_{12} &= V^f \nu_1^f + V^m \nu^m \\ \nu_{13} &= \nu_{12} \\ G_{12} &= G^m \frac{1 + \zeta\eta V^f}{1 - \eta V^f} \\ G_{13} &= G_{12} \end{aligned} \tag{5.9}$$

5.3 Strength

Generally, the prediction of the resistance of plys in CFRP is not a very precise science because it depends on many variables often not known by the designer. These parameters depend on the fibers and matrix interaction, on the type (Pitch/Pan) of fibers, the formulation of the polymer of the matrix, etc.

The failure prediction of a ply is based on theories, but not a single theory in the literature that accurately predicts the failure of the CFRP ply exists. The most common approaches and their mathematical representation only try to give the best "fit" respect to experimental data and tests.

Thus, in this work and especially in this chapter, these complex models are not presented. Only a simple model is proposed and is based on the ROM theory.

Axial Tensile Strength

The first study of axial tensile strength in composite was proposed by Kelly at. al. [45]. Their model provided an analysis for the prediction of axial tensile strength in function of the fibers volume fraction percentile V_f and the matrix fraction one V_m. The resulting *composite ultimate tensile stress* σ_u^t is so expressed in terms of maximum fibers and matrix stresses and their relative volume fraction.

$$\sigma_u^t = \sigma_f' V_f + \sigma_m' V_m \tag{5.10}$$

in which σ_f' and σ_m' are the stress in the fiber and in the matrix respectively.

Axial Compressive Strength

Estimate the compressive strength of a lamina is challenging. Furthermore, it is equally challenging to carry out experimental tests due to the difficulty of setting up the test machine. For this reason, a correction coefficient is generally considered

$$\sigma_u^c = \beta \sigma_u^t \tag{5.11}$$

where β is included between 0.3 and 0.5.

There are some models, like the one presented by Hahn et. al. [46], in which a shear crippling with initial fibers curvature is presented. Hahn et. al. proposed, for an elastic-plastic composite with strong fibers and τ_y (shear yield stress), this equation

$$\sigma_u^c = V_f \frac{G_{12}\tau_y}{\tau_y + \frac{\pi f_0 G_{12}}{L}} \tag{5.12}$$

Other direction Strength

Generally, for the direction 2 and 3 (y and z), the strength performances of the lamina are considered equal to the strength performances of the matrix σ_m' with correction coefficient included between 0.8 and 1. Generally, the relation between tensile and compressive strength in these directions is not the same for axial tensile and compressive axial ties. In direction 2 and 3, the ply is considered an isotropic material made of the matrix material.

An example of strength properties for a common CFRP prepreg is reported in Table 3.1.

5.4 Failure criteria

A *failure criterion* is a model for predicting the failure of solid materials under the action of external loads. These models are expressed with equations and systems of equations with parameters adjusted to fit experimental data of failure for each ply. The most famous criteria were proposed by Tsai-Wu [47], Tsai-Hill (Hill [48] extension of energy criterion Von-Mises [49] for isotropic to anisotropic and after Tsai [50, 51, 52] extended this criterion for anisotropic to unidirectional lamina), Hoffman [53] (a Tsai-Hill extension), Hashin [54], Puck [55, 56, 57]. Other criteria like LaRC and Cuntze are recent and are implemented in commercial FEM software like the previously proposed.

In many books and papers, the notation used to represent failure criteria is varied and confusing. For this reason, in this section, the Ansys User Guide notation (which included all of the most famous criteria) is used.

5.4.1 Maximum Strain

The Maximum Strain Criterion compares the ratios of real strain to the failure strain in the lamina principal coordinate system. Defining different limit for *tensile* and *compressive* loads

$$\begin{aligned} \varepsilon_1 \geq 0 &\rightarrow X_\varepsilon = X_{\varepsilon t} \\ \varepsilon_1 < 0 &\rightarrow X_\varepsilon = X_{\varepsilon c} \\ \varepsilon_2 \geq 0 &\rightarrow Y_\varepsilon = Y_{\varepsilon t} \\ \varepsilon_2 < 0 &\rightarrow Y_\varepsilon = Y_{\varepsilon c} \\ \varepsilon_3 \geq 0 &\rightarrow Z_\varepsilon = Z_{\varepsilon t} \\ \varepsilon_3 < 0 &\rightarrow Z_\varepsilon = Z_{\varepsilon c} \end{aligned} \tag{5.13}$$

the Maximum Strain relation

$$f = max(|\frac{\varepsilon_1}{X_\varepsilon}|, |\frac{\varepsilon_2}{Y_\varepsilon}|, |\frac{\varepsilon_3}{Z_\varepsilon}|, |\frac{\gamma_{12}}{S_\varepsilon}|, |\frac{\gamma_{13}}{R_\varepsilon}|, |\frac{\gamma_{23}}{Q_\varepsilon}|) \tag{5.14}$$

5.4.2 Maximum Stress

The Maximum Stress Criterion compares the ratios of real stress to the failure stress in the lamina principal coordinate system. Defining different limit for *tensile*

and *compressive* loads, as shown before

$$\begin{aligned} \sigma_1 \geq 0 \rightarrow X = X_t \\ \sigma_1 < 0 \rightarrow X = X_c \\ \sigma_2 \geq 0 \rightarrow Y = Y_t \\ \sigma_2 < 0 \rightarrow Y = Y_c \\ \sigma_3 \geq 0 \rightarrow Z = Z_t \\ \sigma_3 < 0 \rightarrow Z = Z_c \end{aligned} \tag{5.15}$$

the Maximum Stress relation

$$f = max(|\frac{\sigma_1}{X}|, |\frac{\sigma_2}{Y}|, |\frac{\sigma_3}{Z}|, |\frac{\tau_{12}}{S}|, |\frac{\tau_{13}}{R}|, |\frac{\tau_{23}}{Q}|) \tag{5.16}$$

5.4.3 Tsai-Wu

Tsai-Wu criteria, like Tsai-Hill and Hoffman, is a quadratic failure criterion in which all the stress/strain components are combined in only one equation. Some coefficients F_i and F_{ij} have been determined as

$$\begin{aligned} F_{11} = \frac{1}{X_t X_c} \\ F_{22} = \frac{1}{Y_t Y_c} \\ F_{44} = \frac{1}{Q^2} \\ F_{66} = \frac{1}{S^2} \\ F_1 = \frac{1}{X_t} - \frac{1}{X_c} \\ F_2 = \frac{1}{Y_t} - \frac{1}{Y_c} \\ F_{55} = \frac{1}{R^2} \end{aligned} \tag{5.17}$$

The terms F_{12}, F_{13} and F_{23} should be determined through biaxial load test but in practice is a calculated in other form or approximated to $F_{12} = -\frac{1}{2}$,$F_{13} = -\frac{1}{2}$,$F_{23} = -\frac{1}{2}$.

Thus, the Tsai-Wu 3D criterion can be express as

$$\begin{aligned} f = \frac{\sigma_1^2}{X_t X_c} + \frac{\sigma_2^2}{Y_t Y_c} + \frac{\sigma_3^2}{Z_t Z_c} + \frac{\tau_{12}^2}{S_{xy}^2} + \frac{\tau_{13}^2}{S_{xz}^2} + \frac{\tau_{23}^2}{S_{yz}^2} + \\ 2F_{12}\frac{\sigma_1\sigma_2}{\sqrt{X_t X_c Y_t Y_c}} + 2F_{13}\frac{\sigma_1\sigma_3}{\sqrt{X_t X_c Z_t Z_c}} + 2F_{23}\frac{\sigma_2\sigma_3}{\sqrt{Y_t Y_c Z_t Z_c}} + \\ \sigma_1(\frac{1}{X_t} - \frac{1}{X_c}) + \sigma_2(\frac{1}{Y_t} - \frac{1}{Y_c}) + +\sigma_3(\frac{1}{Z_t} - \frac{1}{Z_c}) \end{aligned} \tag{5.18}$$

In Tsai-Wu 2D expression, the σ_3 and related τ, F, and Z terms are neglected.

5.4.4 Tsai-Hill

This criterion is similar of Tsai-Wu one. Tsai-Hill criterion use different equation for UD lamina and Woven plies. In Tsai-Hill 3D criterion, the coefficients F, G, and H[58] are expressed as

$$\begin{aligned} F &= \frac{1}{2}(-\frac{1}{X^2} + \frac{1}{Y^2} + \frac{1}{Z^2}) \\ G &= \frac{1}{2}(\frac{1}{X^2} - \frac{1}{Y^2} + \frac{1}{Z^2}) \\ H &= \frac{1}{2}(\frac{1}{X^2} + \frac{1}{Y^2} - \frac{1}{Z^2}) \end{aligned} \tag{5.19}$$

The other terms (L, M, and N) are also related to S_ij terms but only for the particular loads condition.

$$\begin{aligned} L &= \frac{1}{2S_{yz}^2} \\ M &= \frac{1}{2S_{xz}^2} \\ N &= \frac{1}{2S_{xy}^2} \end{aligned} \tag{5.20}$$

The coefficients F, G, H, L, M and N are the Hill parameters. they need to be interpreted as yield point values for ductile materials and breakable limit for brittle materials. Finally, the single equation became

$$\begin{aligned} (G+H)\sigma_1^2 + (F+H)\sigma_2^2 + (F+G)\sigma_3^2 - 2H\sigma_1\sigma_2 - 2G\sigma_1\sigma_3 - 2F\sigma_1\sigma_3 + \\ 2L\tau_{23}^2 + 2M\tau_{13}^2 + 2N\tau_{12}^2 = 1 \end{aligned} \tag{5.21}$$

The main problem with the Tsai-Hill formulation is that there is no difference between traction and compression.

5.4.5 Hoffman

Hoffmann's criterion is a generalization of Tsai-Hill, in which the difference in tensile and compressive strength is taking into account. In the case of equal tensile and compressive strength, the Hoffmann criterion is similar to the Tsai-Hill one. The F_{ij} parameters can be defined as

$$\begin{aligned} F_{12} &= \frac{1}{X_t X_c} + \frac{1}{Y_t Y_c} - \frac{1}{Z_t Z_c} \\ F_{13} &= \frac{1}{X_t X_c} - \frac{1}{Y_t Y_c} + \frac{1}{Z_t Z_c} \\ F_{23} &= -\frac{1}{X_t X_c} + \frac{1}{Y_t Y_c} + \frac{1}{Z_t Z_c} \end{aligned} \tag{5.22}$$

The Hoffman 3D criterion can be expressed as

$$\begin{aligned} f = \frac{\sigma_1^2}{X_t X_c} + \frac{\sigma_2^2}{Y_t Y_c} + \frac{\sigma_3^2}{Z_t Z_c} + \frac{\tau_{12}^2}{S_{xy}^2} + \frac{\tau_{13}^2}{S_{xz}^2} + \frac{\tau_{23}^2}{S_{yz}^2} - \\ (F_1 2\sigma_1\sigma_2 + F_2 3\sigma_2\sigma_3 + F_1 3\sigma_1\sigma_3) + \frac{\sigma_1}{X_t X_c} + \frac{\sigma_2}{Y_t Y_c} + \frac{\sigma_3}{Z_t Z_c} \end{aligned} \tag{5.23}$$

5.4.6 Hashin

Hashin Criterion is an interacting failure criterion that provides different failure modes: fiber, matrix, and delamination. In origin, it was developed for UD ply. This criterion provides a different approach between tensile and compressive loads.

In 3D case, for the fiber failure

$$\begin{aligned} f_{f,t} = (\frac{\sigma_1}{X_t})^2 + (\frac{\tau_{12}}{S})^2 + (\frac{\tau_{13}}{R})^2 \\ f_{f,c} = -\frac{\sigma_1}{X_c} \end{aligned} \tag{5.24}$$

In the case of transverse tensile and compression loads the matrix failure is predicted as

$$\begin{aligned} f_{m,t} = (\frac{\sigma_2}{Y_t})^2 + (\frac{\tau_{23}}{Q})^2 + (\frac{\tau_{12}}{S})^2 + (\frac{\tau_{13}}{R})^2 \\ f_{m,c} = (\frac{\sigma_2}{2Q})^2 + (\frac{\tau_{23}}{Q})^2 + (\frac{\tau_{12}}{S})^2 + ((\frac{Y_c}{2Q})^2 - 1)\frac{\sigma_2}{Y_c} \end{aligned} \tag{5.25}$$

For the delamination case

$$f_d = (\frac{\sigma_3}{Z})^2 + (\frac{\tau_{13}}{R})^2 + (\frac{\tau_{23}}{Q})^2 \tag{5.26}$$

Finally, the most critical failure mode is selected

$$f = max(f_f, f_m, f_d) \tag{5.27}$$

5.4.7 Puck

There are three different Puck criteria in literature, the oldest two are simpler, and the last one is the modified Puck. Both criteria consider failure mode loads separately. In this section, the most recent criterion and, probably, the most complex one is presented. For the Fiber Failure (FF) is the same as the maximum stress or maximum strain criterion

$$\begin{aligned} \sigma_1 > 0 \rightarrow \frac{\sigma_1}{X_t} = 1 \\ \sigma_1 < 0 \rightarrow \frac{\sigma_1}{X_c} = 1 \\ \varepsilon_1 > 0 \rightarrow \frac{\varepsilon_1}{X_{\varepsilon,t}} = 1 \\ \varepsilon_1 < 0 \rightarrow \frac{\varepsilon_1}{X_{\varepsilon,c}} = 1 \end{aligned} \tag{5.28}$$

A different mode is the Interfiber Failure (IFF). In this subsection, the 3D expression is presented. Generally Puck's action plane strength criterion is defined by seven parameters: $R^+_\perp$, $R_{\perp\parallel}$, $R^-_\perp$, $p^+_{\perp\parallel}$, $p^-_{\perp\parallel}$, $p^+_{\perp\perp}$ and $p^-_{\perp\perp}$ where R is the fracture resistance and p for slope of fracture curves. The parallel and perpendicular symbols stands for the reference direction respect fibers. For the 3D stress state:

$$\begin{aligned} \sigma_n \geq 0 \rightarrow f_E = \sqrt{((\frac{1}{R^+_\perp} - \frac{p^+_{\perp\psi}}{R^A_{\perp\psi}})\sigma_n)^2 + (\frac{\tau_{nt}}{R^A_{\perp\perp}})^2 + (\frac{\tau_{n1}}{R_{\perp\parallel}})^2} + \frac{p^+_{\perp\psi}}{R^A_{\perp\psi}}\sigma_n \\ \sigma_n < 0 \rightarrow f_E = \sqrt{(\frac{\tau_{nt}}{R^A_{\perp\perp}})^2 + (\frac{\tau_{n1}}{R_{\perp\parallel}})^2 + (\frac{p^-_{\perp\psi}}{R^A_{\perp\psi}}\sigma_n)^2} + \frac{p^-_{\perp\psi}}{R^A_{\perp\psi}}\sigma_n \end{aligned} \tag{5.29}$$

The stresses are expressed in the n plane with inclination θ. So

$$\begin{aligned} \sigma_n = \sigma_2 \cos^2\theta + \sigma_3 \sin^2\theta + 2\tau_{23}\sin\theta\cos\theta \\ \tau_{nt} = (\sigma_3 - \sigma_2)\sin\theta\cos\theta + \tau_{23}(\cos^2\theta - \sin^2\theta) \\ \tau_{n1} = \tau_{31}\sin\theta + \tau_{21}\cos\theta \end{aligned} \tag{5.30}$$

thus the *Exposure Factor* f_E is

$$f_E(\theta) = \begin{cases} \arccos(\sqrt{\frac{-R^A_{\perp\perp}}{-\sigma_2}}) \leftarrow \sigma_2 < -R^A_{\perp\perp} \\ 0 \leftarrow \sigma_2 \geq -R^A_{\perp\perp} \end{cases} \tag{5.31}$$

The precious criterion can be used to determinate delamination if we add an

additional factor for interface f_w^{if}. If applied

$$\begin{aligned}\sigma_3 \geq 0 \rightarrow \frac{1}{f_w^{if}}\sqrt{((\frac{1}{R_\perp^+}-\frac{p_{\perp\psi}^+}{R_{\perp\psi}^A})\sigma_3)^2+(\frac{\tau_{32}}{R_{\perp\perp}^A})^2+(\frac{\tau_{31}}{R_{\perp\parallel}})^2}+\frac{p_{\perp\psi}^+}{R_{\perp\psi}^A}\sigma_3=1\\ \sigma_3 < 0 \rightarrow \frac{1}{f_w^{if}}\sqrt{(\frac{\tau_{32}}{R_{\perp\perp}^A})^2+(\frac{\tau_{31}}{R_{\perp\parallel}})^2+(\frac{p_{\perp\psi}^-}{R_{\perp\psi}^A}\sigma_3)^2}+\frac{p_{\perp\psi}^-}{R_{\perp\psi}^A}\sigma_3=1\end{aligned} \tag{5.32}$$

Puck constant for carbon are set, for each ply, as

$$\begin{aligned}p_{\perp\parallel}^+ &= 0.35\\ p_{\perp\parallel}^- &= 0.30\\ p_{\perp\perp}^+ &= 0.25\\ p_{\perp\perp}^- &= 0.20\end{aligned} \tag{5.33}$$

Puck constant for glass are set, for each ply, as

$$\begin{aligned}p_{\perp\parallel}^+ &= 0.30\\ p_{\perp\parallel}^- &= 0.25\\ p_{\perp\perp}^+ &= 0.20\\ p_{\perp\perp}^- &= 0.20\end{aligned} \tag{5.34}$$

5.4.8 LaRC

LaRC (LaRC04 3D) is a failure criterion developed for FRP and stands for *Langley Research Center*. It is based on physical models for the mode of failure and makes different formulations distinguish between matrix and fiber failure for each direction (tensile and compressive loads included). LaRC04 3D considers the in-situ strength of a ply, which is different from the same ply in a full UD laminate [59, 60].

The required properties to use the criteria are based on material experimental tests. Some reference values can be taken from the literature [61]. Some parameters can be so defined G_{Ic} as fracture toughness in mode I, G_{IIc} fracture toughness in mode II, S_L the longitudinal shear strength, the fracture toughness ratio $g = \frac{G_{Ic}}{G_{IIc}}$, the fracture angle α_0.

Some coefficient need to be determined, like the Friction one and the in-situ strength

$$\begin{aligned}Y_{is}^T &= \sqrt{\frac{8G_{Ic}}{\pi t \Lambda_{22}}}\\ S_{is}^L &= \sqrt{\frac{8G_{IIc}}{\pi t \Lambda_{44}}}\end{aligned} \tag{5.35}$$

where

$$\begin{aligned} \Lambda_{22} &= 2(\frac{1}{E_2} - \frac{\nu_{21}^2}{E1}) \\ \Lambda_{44} &= \frac{1}{G_{12}} \end{aligned} \tag{5.36}$$

For the Fiber Misalignment Frame, in LaRC04 3D the model assumes that the fail occurs in the plane of the ply in which ψ is the angle of kink plane respect the lamina.

$$\psi = \frac{1}{2}\arctan(\frac{2\tau_{23}}{\sigma_2 - \sigma_3}) \tag{5.37}$$

Stresses can be rotated in the plane of the lamina in a misaligned frame. Besides, the stresses can be rotated into the misaligned coordinate system, but in this thesis, the formulation is not reported.

The fiber tensile failure is the same of the maximum stress criterion

$$\begin{aligned} \sigma_1 > 0 \rightarrow f_f &= \frac{\sigma_{11}}{X_t} \\ \sigma_1 < 0, \sigma_{2m2m} < 0 \rightarrow f_f &= (\frac{\tau_{1m2m}}{S_{is}^L - \eta^L \sigma_{2m2m}})^2 \end{aligned} \tag{5.38}$$

Ansys gives a function for the failure for fiber in compression and matrix in tension

$$\sigma_1 < 0, \sigma_{2m2m} \geq 0 \rightarrow f_{mf} = (1-g)\frac{\sigma_{2m2m}}{Y_{is}^T} + (\frac{\sigma_{2m2m}}{Y_{is}^T})^2 + (\frac{\tau_{1m2m}}{S^L})^2 + \frac{\Lambda_{23}}{2}(\frac{\tau_{2m3\psi}}{S^L})^2 \tag{5.39}$$

Otherwise, Ansys suggest for Matrix Failure

$$\begin{aligned} \sigma_2 \geq 0 \rightarrow f_m &= (1-g)\frac{\sigma_2}{Y_{is}^T} + g(\frac{\sigma_2}{Y_{is}^T})^2 + (\frac{\tau_{12}}{S^L})^2 + \frac{\Lambda_{23}}{2}(\frac{\tau_{23}}{S^L})^2 \\ \sigma_2 < 0, \sigma_1 < -Y_c \rightarrow f_m &= (\frac{\tau^{Tm}}{S^T - \eta^T \sigma_n^m})^2 - (\frac{\tau^{Lm}}{S_{is}^L - \eta^L \sigma_n^m})^2 \\ \sigma_2 < 0, \sigma_1 \geq -Y_c \rightarrow f_m &= (\frac{\tau^T}{S^T - \eta^T \sigma_n})^2 - (\frac{\tau^L}{S_{is}^L - \eta^L \sigma_n})^2 \end{aligned} \tag{5.40}$$

where σ_{nm}, τ_m^T and τ_m^L are in function of the angle α (formulation not reported here).

5.4.9 Cuntze

Cuntze's failure criteria is applicable for different materials but here is applied to transversely isotropic UD lamina [62].

Cuntze's model provide 5 different failure modes, FF1 tension, FF2 compression, IFF1 transverse tension, IFF2 transverse compression and IFF3 shear. For each one modes, the equivalent stress is provided.

$$\{\sigma_{eq}^{mode}\} = (\sigma_{eq}^{\parallel\sigma}, \sigma_{eq}^{\parallel\tau}, \sigma_{eq}^{\perp\ \sigma}, \sigma_{eq}^{\perp\tau}, \sigma^{\parallel\perp},)^T \tag{5.41}$$

Additional parameters and the final formulation for each failure mode is reported deeply in the Cuntze's literature[63, 64].

5.5 Appendix: Matlab Code

In this section, an example of MATLAB script for the calculation of the micromechanical properties of an UD an biaxial composite prepreg is reported. In particular, the routine proposed could be used for the calculation of the CTEs, strength and elastic properties of a general composite ply. The method to create the stiffness and compliance matrix for a general UD and biaxial ply is also presented.

```
%-------------------------------------------------------------------------

    pesC   = pesF / (1-Mm);                    % [g/m2]
    Mf     = 1 - Mm;                           % [%/100]
    Vf     = (Mf/rhoF)/((Mf/rhoF)+(Mm/rhoR));  % [%/100]
    Vm     = 1 - Vf;                           % [%/100]
    rhoC   = rhoF*Vf+rhoR*Vm;                  % [g/cm3]
    h      = pesF/(Vf*rhoF*1000);              % [mm]

    SpF=(pesF/rhoF/1000);
    SpR=((pesC-pesF)/rhoR/1000);
    SpC=(pesC/rhoC/1000);

    Pr.Vm=Vm*100;
    Pr.pesF=pesF;
    Pr.pesR=pesC-pesF;
    Pr.Vm=Vm;

    %CTE
    Pr.alpha1 = (alphaF*EF*Vf + alphaR*ER*Vm)/(EF*Vf + ER*
        Vm);
    Pr.alpha2 = alphaR*Vm + alphaF*Vf + (vF*ER - vR*EF)*(
        alphaF-alphaR)/(ER/Vf + EF/Vm);
```

```
22      Pr.alpha3 = Pr.alpha2;
23      %Stress Limit
24      ElR=RR/ER;
25      Pr.sig.lt = RF*Vf + RR*Vm;
26      Pr.sig.lc = -(ElR*(1-Vf^(1/3))*(EF*Vf+EF*Vm)/(vF*Vf+vR*
            Vm));
27
28  %-------------- Elasticity
29
30       xiE        = 2+40*Vf^10;
31       niE        = ((EF/ER)-1)/((EF/ER)+xiE);
32       E1         = Vm*ER + Vf*EF;
33       E2         = ER*(1+xiE*niE*Vf)/(1-niE*Vf);
34       E3         = E2;
35
36       xiG        = 1+40*Vf^10;
37       niG        = ((GF/GR)-1)/((GF/GR)+xiG);
38       G12        = GR*(1+xiG*niG*Vf)/(1-niG*Vf);
39       G13        = G12;
40
41       Kf         = EF/(3*(1-2*vF));
42       Km         = ER/(3*(1-2*vR));
43       K          = (Vf/Kf + Vm/Km)^-1;
44       v12        = Vf*vF + Vm*vR;
45       v23        = 1 - (v12*(E2/E1)) - E2/(3*K);
46       v13        = v12;
47
48       G23        = (2*((1+v23)/(E2)))^-1;
49
50    if strcmp(Tipo, 'UD')==1
51       %
```

```
52     C1  =       [1/E1          -v12/E1        -v12/E1        0
                                 0              0;
53                  -v12/E1        1/E2           -v23/E2        0
                                                  0              0;
54                  -v12/E1        -v23/E2        1/E3           0
                                                  0              0;
```

```
55                  0                   0                   0
                        2*((1+v23)/(E2))          0                   0;
56                  0                   0                   0          0
                                                    1/G12          0;
57                  0                   0                   0
                                          0                   0
                        1/G12];
58
59        K1   = inv(C1);
60
61  Pr.E1=E1;
62  Pr.E2=E2;
63  Pr.E3=Pr.E2;
64  Pr.v12=v12;
65  Pr.v23=v23;
66  Pr.v13=v13;
67  Pr.G12=G12;
68  Pr.G13=G13;
69  Pr.G23=G23;
70  Pr.SpC=SpC;
71  Pr.rhoC=rhoC;
72  Pr.pesC=pesC;
73  Pr.K=K1;
74
75    elseif strcmp(Tipo, 'FABRIC')==1
76
77            ni12=v12;
78            ni13=ni12;
79            ni21=ni12*(E2/E1);
80            ni23=v23;
81
82            K=1-2*ni12*ni21*(1+ni23)-ni23^2;
83            c11=(1-ni23^2)*E1/K;
84            c22=(1-ni12*ni21)*E2/K;
85            c33=(1-ni12*ni21)*E3/K;
86            c12=(1+ni23)*ni21*E1/K;
87            c13=c12;
88            c23=(ni23+ni12*ni21)*E2/K;
89            c44=G23;
90            c55=G13;
```

```
91          c66=G12;
92
93          C=[c11  c12  c13  0  0  0
94              c12  c22  c23  0  0  0
95              c13  c23  c33  0  0  0
96               0    0    0  c44  0  0
97               0    0    0  0  c55  0
98               0    0    0  0  0  c66];
99
100         lambda=a1*4;
101         c=0.10*a1  ;
102         a2=a1;
103
104             x=0:lambda/100:lambda;
105             lun=length(x)-1;
106
107     for  j=1:lun
108         a=(a1+(a2*0.5)-(0.5*c))+((c/2)*cos(2*pi*x(j)/lambda
                ));
109         b=(a1+(a2*0.5)-(0.5*c))+((c/2)*cos(2*pi*x(j+1)/
                lambda));
110         teta(j)=atan((b-a)/(x(j+1)-x(j)));
111         lung(j)=((b-a)^2+(x(j+1)-x(j))^2)^0.5;
112         Velem(j)=lung(j)*pi*(a1/2)^2;
113
114     end
115         lato=(pi*((a1/2)^2)/(Vf))^0.5;
116
117     Cs=0;
118     Csr=0;
119     for  j=1:lun
120         l=cos(teta(j));
121         m=cos(pi/2-teta(j));
122         n=0;
123         l1=cos(pi/2+teta(j));
124         m1=cos(teta(j));
125         n1=0;
126         l2=0;
127         m2=0;
128         n2=1;
```

```
129
130         T=[ l^2     m^2     n^2     2*m*n           2*l*n           2*l*m
131             l1^2    m1^2    n1^2    2*m1*n1         2*l1*n1         2*l1*
                    m1
132             l2^2    m2^2    n2^2    2*m2*n2         2*l2*n2         2*l2*
                    m2
133             l1*l2   m1*m2   n1*n2   m1*n2+m2*n1     l1*n2+l2*n1     l1*m2
                    +l2*m1
134             l*l2    m*m2    n*n2    m*n2+m2*n       l*n2+l2*n       l*m2+
                    l2*m
135             l1*l    m1*m    n1*n    m*n1+m1*n       l*n1+l1*n       l*m1+
                    l1*m];
136
137         Ci=(T')*C*T;
138         ki(j)=(lung(j)*lato^2)/((lambda^2)*2*a1);
139         Ck=ki(j)*Ci;
140         Cs=Cs+Ck;
141
142     end
143
144     Tr=[0  1  0  0  0  0;
145         1  0  0  0  0  0;
146         0  0  1  0  0  0;
147         0  0  0  1  0  0;
148         0  0  0  0  1  0;
149         0  0  0  0  0  -1];
150     Csr=(Tr')*Cs*Tr;
151
152         % stiffness Matrix RVE
153         K1=Csr+Cs;
154         C1=inv(K1);
155
156         % Ply properties
157      xiE         = 2+40*Vf^10;
158      niE         = ((EF/ER)-1)/((EF/ER)+xiE);
159      E1          = Vm*ER + Vf*EF;
160      E2          = ER*(1+xiE*niE*Vf)/(1-niE*Vf);
161      Pr.E3           = E2;
162
163      xiG         = 1+40*Vf^10;
```

```
164         niG         = ((GF/GR)-1)/((GF/GR)+xiG);
165         G12         = GR*(1+xiG*niG*Vf)/(1-niG*Vf);
166         G13         = G12;
167
168         Kf          = EF/(3*(1-2*vF));
169         Km          = ER/(3*(1-2*vR));
170         K           = (Vf/Kf + Vm/Km)^-1;
171         v12         = Vf*vF + Vm*vR;
172
173         v13         = v12;
174         G23         = (2*((1+v23)/(E2)))^-1;
175
176             Pr.E1=(C1(1,1))^-1;
177             Pr.E2=(C1(2,2))^-1;
178             Pr.v23      = 1 - (v12*(Pr.E2/Pr.E1)) - Pr.E2/(3*K);
179             Pr.G12=(C1(6,6))^-1;
180             Pr.G13= G13;
181             Pr.v12=v12;
182             Pr.v23   = v23;
183             Pr.G23   = G23;
184             Pr.SpC=SpC;
185             Pr.rhoC=rhoC;
186             Pr.pesC=pesC;
187             Pr.K=K1;
188
189
190 elseif strcmp(Tipo, 'BIAX')==1
191     %-------------------------------------------------------
192     C1  = [1/E1         -v12/E1     -v12/E1     0  0  0;
193            -v12/E1        1/E2      -v23/E2     0  0  0;
194            -v12/E1     -v23/E2        1/E3      0  0  0;
195               0                0                  0
                      2*((1+v23)/(E2))   0  0;
196               0                0                  0    0     1/
                      G12   0;
197               0                0                  0    0     0
                      1/G12];
198
199     K1  = inv(C1);
200
```

```
201     ang=deg2rad(ang);
202     ang=[+ang -ang];
203     t=[-SpC/2 0 SpC/2];
204     A=zeros(3);
205     B=zeros(3);
206     D=zeros(3);
207     for i = 1 : 2
208             z(i)=t(i+1)-t(i);
209             z2(i)=((t(i+1))^2)-((t(i))^2);
210             z3(i)=((t(i+1))^3)-((t(i))^3);
211
212         coseno=cos(ang(i));
213         coseno2=(cos(ang(i)))^2;
214         coseno3=(cos(ang(i)))^3;
215         coseno4=(cos(ang(i)))^4;
216         seno=sin(ang(i));
217         seno2=(sin(ang(i)))^2;
218         seno3=(sin(ang(i)))^3;
219         seno4=(sin(ang(i)))^4;
220
221         A11(i)=((K1(1,1)*coseno4)+(2*(K1(1,2)+2*K1(6,6))*
                seno2*coseno2)+(K1(2,2)*seno4)).*z(i);
222         A12(i)=(((K1(1,1)+K1(2,2)-4*K1(6,6))*seno2*coseno2)
                +(K1(1,2)*(seno4+coseno4))).*z(i);
223         A22(i)=((K1(1,1)*seno4)+(2*(K1(1,2)+2*K1(6,6))*
                seno2*coseno2)+(K1(2,2)*coseno4)).*z(i);
224         A16(i)=(((K1(1,1)-K1(1,2)-2*K1(6,6))*seno*coseno3)
                +((K1(1,2)-K1(2,2)+2*K1(6,6))*seno3*coseno)).*z(
                i);
225         A26(i)=(((K1(1,1)-K1(1,2)-2*K1(6,6))*seno3*coseno)
                +((K1(1,2)-K1(2,2)+2*K1(6,6))*seno*coseno3)).*z(
                i);
226         A66(i)=(((K1(1,1)+K1(2,2)-2*K1(1,2)-2*K1(6,6))*
                seno2*coseno2)+(K1(6,6)*(seno4+coseno4))).*z(i);
227
228         B11(i)=((K1(1,1)*coseno4)+(2*(K1(1,2)+2*K1(6,6))*
                seno2*coseno2)+(K1(2,2)*seno4)).*z2(i);
229         B12(i)=(((K1(1,1)+K1(2,2)-4*K1(6,6))*seno2*coseno2)
                +(K1(1,2)*(seno4+coseno4))).*z2(i);
```

```
230         B22(i)=((K1(1,1)*seno4)+(2*(K1(1,2)+2*K1(6,6))*
                seno2*coseno2)+(K1(2,2)*coseno4)).*z2(i);
231         B16(i)=(((K1(1,1)-K1(1,2)-2*K1(6,6))*seno*coseno3)
                +((K1(1,2)-K1(2,2)+2*K1(6,6))*seno3*coseno)).*z2
                (i);
232         B26(i)=(((K1(1,1)-K1(1,2)-2*K1(6,6))*seno3*coseno)
                +((K1(1,2)-K1(2,2)+2*K1(6,6))*seno*coseno3)).*z2
                (i);
233         B66(i)=(((K1(1,1)+K1(2,2)-2*K1(1,2)-2*K1(6,6))*
                seno2*coseno2)+(K1(6,6)*(seno4+coseno4))).*z2(i)
                ;
234
235         D11(i)=((K1(1,1)*coseno4)+(2*(K1(1,2)+2*K1(6,6))*
                seno2*coseno2)+(K1(2,2)*seno4)).*z3(i);
236         D12(i)=(((K1(1,1)+K1(2,2)-4*K1(6,6))*seno2*coseno2)
                +(K1(1,2)*(seno4+coseno4))).*z3(i);
237         D22(i)=((K1(1,1)*seno4)+(2*(K1(1,2)+2*K1(6,6))*
                seno2*coseno2)+(K1(2,2)*coseno4)).*z3(i);
238         D16(i)=(((K1(1,1)-K1(1,2)-2*K1(6,6))*seno*coseno3)
                +((K1(1,2)-K1(2,2)+2*K1(6,6))*seno3*coseno)).*z3
                (i);
239         D26(i)=(((K1(1,1)-K1(1,2)-2*K1(6,6))*seno3*coseno)
                +((K1(1,2)-K1(2,2)+2*K1(6,6))*seno*coseno3)).*z3
                (i);
240         D66(i)=(((K1(1,1)+K1(2,2)-2*K1(1,2)-2*K1(6,6))*
                seno2*coseno2)+(K1(6,6)*(seno4+coseno4))).*z3(i)
                ;
241
242     AA=[A11(i) A12(i) A16(i);
243         A12(i) A22(i) A26(i);
244         A16(i) A26(i) A66(i)];
245     BB=[B11(i) B12(i) B16(i);
246         B12(i) B22(i) B26(i);
247         B16(i) B26(i) B66(i)];
248     DD=[D11(i) D12(i) D16(i);
249         D12(i) D22(i) D26(i);
250         D16(i) D26(i) D66(i)];
251
252     A=A+AA;
253     B=B+BB;
```

```
254     D=D+DD;
255     end
256     B=B./2;
257     D=D./3;
258     K1=[A./SpC (2/SpC^2).*B ; (2/SpC^2).*B (12/SpC^3).*D];
259     a=inv((A-B*inv(D)*B));
260     d=inv((D-B*inv(A)*B));
261     b=-inv((A-B*inv(D)*B))+B*inv(D);
262     astar=a*SpC;
263     dstar=d*((SpC^3)/12);
264
265      C1=inv(K1);
266
267      xiE       = 2+40*Vf^10;
268      niE       = ((EF/ER)-1)/((EF/ER)+xiE);
269      E1        = Vm*ER + Vf*EF;
270      E2        = ER*(1+xiE*niE*Vf)/(1-niE*Vf);
271      Pr.E3         = E2;
272
273      xiG       = 1+40*Vf^10;
274      niG       = ((GF/GR)-1)/((GF/GR)+xiG);
275      G12       = GR*(1+xiG*niG*Vf)/(1-niG*Vf);
276      G13       = G12;
277
278      Kf       = EF/(3*(1-2*vF));
279      Km       = ER/(3*(1-2*vR));
280      K        = (Vf/Kf + Vm/Km)^-1;
281      v12      = Vf*vF + Vm*vR;
282      v13      = v12;
283
284      G23      = (2*((1+v23)/(E2)))^-1;
285
286          Pr.E1=(C1(1,1))^-1;
287          Pr.E2=(C1(2,2))^-1;
288          Pr.G12=(C1(6,6))^-1;
289          Pr.G13= G13;
290          Pr.v12=v12;
291          Pr.v13=Pr.v12;
292          Pr.v23      = 1 - (v12*(E2/E1)) - E2/(3*K);
293          Pr.G23   = G23;
```

```
294
295
296             Pr.SpC=SpC;
297             Pr.rhoC=rhoC;
298             Pr.pesC=pesC;
299             Pr.K=K1;
300     end
```

Part II

Damping analysis

Chapter 6

Damping theory

6.1 Introduction

> "Damping is the phenomenon by which mechanical energy is dissipated (usually by conversion into internal thermal energy) in dynamic systems" De Silva[65].

The following theoretical treatment in this chapter is inspired by the work carried out by Professor De Silva [65]. His book, very complete, elegantly exposes every aspect of damping.

Knowledge of the phenomenon of damping is of fundamental importance both in the design phase and in analyzing a dynamic system. Knowledge of the damping of structures and the materials that compose them is crucial for predicting behaviors through numerical calculations and simulations.

To properly study the dynamic behavior of a system, it is necessary to identify the damping mechanisms that are part of a system representing a current challenge. Next, it is required to choose a model that can represent, within an acceptable error, the dissipation of energy. Finally, the parameters of the damping model can be identified in the test phase.

The damping phenomenon is not yet fully understood [65, 66, 67], but three main forms can be identified:

- Internal/Material damping.
- Structural damping (connections, joints and interfaces).
- Fluid damping (air/fluid system interaction).

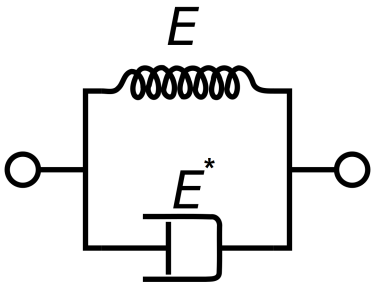

Figure 6.1: Schematic representation of Kelvin–Voigt model.

6.1.1 Internal/Material Damping

It is impossible to define a model for damping that represents all types of material. The main two material damping models are Hysteretic Damping and Viscoelastic Damping.

For both models, stress and strain relations could be represented as a hysteresis loop in a stress and strain diagram. The energy dissipated (the damping power) could be so associated with the hysteresis loop area.

In terms of per-unit volume damping capacity d

$$d = \oint \sigma d\varepsilon \tag{6.1}$$

The force of damping depends not only on the displacements but also on the speed. The motivation is straightforward: to form a hysteresis cycle, it's necessary a function consisting of a variable and its first derivative ($f(x, \dot{x})$).

Viscoelastic damping

For a viscoelastic material, such as rubber, the strain stress relationship can be represented by a linear differential equation with constant coefficients. This equation is known as the Kelvin-Voigt model [68] and can be represented by an elastic spring and a viscous damper connected in parallel, as shown in Figure 6.1.

$$\sigma = E\varepsilon + E^* \frac{d\varepsilon}{dt} \tag{6.2}$$

In which E is the Young Modulus and E^* an independent viscoelastic parameter. It can be noticed that the elastic therms ($E\varepsilon$) do not contribute to damping. So, the damping capacity per unit volume is

$$d_v = E^* \oint \frac{d\varepsilon}{dt} d\varepsilon\pi \tag{6.3}$$

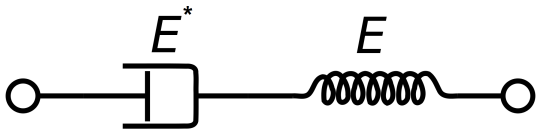

Figure 6.2: Schematic representation of Maxwell model.

For a harmonic excitation applied on a material

$$\varepsilon = \varepsilon_{max} \cos(\omega t) \tag{6.4}$$

The Equation 6.4 can be substituted in Equation 6.3 to obtain

$$d_v = \pi \omega E^* \varepsilon_{max}^2 \tag{6.5}$$

According to the previous equation $\sigma_{max} = E\varepsilon_{max}$ so

$$d_v = \frac{\pi \omega E^* \sigma_{max}^2}{E^2} \tag{6.6}$$

In this model (Kelvin-Voigt model [68]) it can be noticed that d_v depends on the frequency of excitation ω.

There are also other famous models, such as the Maxwell model (1867) [69] with his schematic representation of a viscous damper and an elastic spring connected in series as shown in Figure 6.2.

$$\sigma + c_s \frac{d\sigma}{dt} = E^* \frac{d\varepsilon}{dt} \tag{6.7}$$

The combination of the Kelvin-Voigt model and the Maxwell model, called the standard-linear-solid model (or Zener model) [70], is more proper respect the previous ones and can be represented as shown in Figure 6.3.

$$\sigma + c_s \frac{d\sigma}{dt} = E\varepsilon + E^* \frac{d\varepsilon}{dt} \tag{6.8}$$

For simple cases, however, the Kelvin-Voigt model adequately represents the viscous damping phenomena.

Hysteretic damping

For some material types, the damping power does not depend on the frequency of variation of the strains. This type of internal damping is called Hysteretic damping.

In this particular case, the per-unit volume damping capacity d_h can be represented as

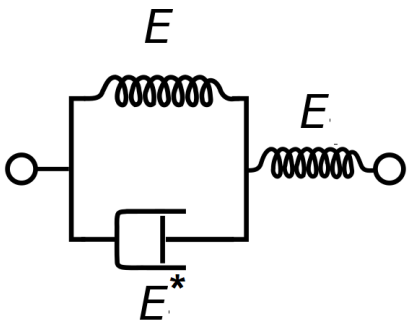

Figure 6.3: Schematic representation of Standard-Linear-Solid model.

$$d_h = J\sigma_{max}^n \tag{6.9}$$

A simple model, with $n = 2$, that satisfies Equation 6.9, could be written as

$$\sigma = E\varepsilon + \frac{\widetilde{E}}{\omega}\frac{d\varepsilon}{dt} \tag{6.10}$$

The parameter $\widetilde{E}$ is equivalent to E^* that depends on the frequency of motion, according to $\widetilde{E} = E^*\omega$. For a harmonic motion, $\varepsilon = \varepsilon_0 \cos(\omega t)$, the hysteric damping can be represented by using the complex Modulus of Elasticity composed by a real part which corresponds to the Young's Modulus and an imaginary one which corresponds to the Hysteric loss Modulus.

$$\sigma = (E + j\widetilde{E})\varepsilon \tag{6.11}$$

It also possible to combine the Kelvin-Voigt model with this one to obtain a simple Viscoelastic-Hysteric model.

$$\sigma = E\varepsilon + (E^* + \frac{\widetilde{E}}{\omega})\frac{d\varepsilon}{dt} \tag{6.12}$$

6.1.2 Structural damping

Structural damping involves many phenomena and is generally not solely and merely determinable. For this reason, it is not possible to identify an analytical model that allows for understanding all the structural damping.

Usually, structural damping is measured or obtained from complex models that exclude damping due to interaction with the material's air and internal damping.

The predominant element in this type of damping in the structures is the friction between the various parts, such as joints or interfaces, called Coulomb

damping. The relation for an idealized hysteresis loop for frictional Coulomb damping is

$$f = c\,\mathrm{sgn}(\dot{q}) \tag{6.13}$$

f is the force of damping, q the displacement at the joint/interface, and c the friction parameter. From this, it possible to write a simple structural damping model due to deformation

$$f = c|q|\,\mathrm{sgn}(\dot{q}) \tag{6.14}$$

6.1.3 Fluid damping

The resistance (force) per unit area that a body undergoes in a fluid, such as air or water, is based on fluid damping. When a body oscillates in the air, it dissipates energy and experiences a force based on its drag coefficient.

This force is usually expressed as

$$f_d = \frac{1}{2}c\rho\dot{q}^2\,\mathrm{sgn}(\dot{q}) \tag{6.15}$$

In which c is the drag coefficient that derives from Reynold's number, and ρ is the fluid density.

For this kind of damping, in terms of per-unit volume fluid damping capacity d_f is

$$d_f = \frac{\oint \int_0^{l_x} \int_0^{l_y} f_d dz dx dq(x,z,q)}{l_x l_y q_0} \tag{6.16}$$

l_x and l_y are the dimensions of the element cross-section in the x and y-directions, respectively. q_0 is the normalized amplitude parameter for the displacement of the structure.

6.2 Vibration Analysis

It is considered a system with n degrees-of-freedom (DOF) in which the vector x represents the n degrees of movement of the inertial subsystems.

Every elastic element could be considered a spring if it is assumed the condition of small-displacement. The equation of motion could be so defined as

$$M\ddot{x} + d + Kx = f(t) \tag{6.17}$$

Table 6.1: Common damping Models used in Dynamic System Equations.

Class of Damping	Type of Damping	Model (d_i)
Internal/Material	Viscous	$\sum_j C_{ij}\dot{x}_j$
	Hysteric	$\sum_j \frac{1}{\omega}C_{ij}\dot{x}_j$
Structural	-	$\sum_j C_{ij}\lvert x_j\rvert \operatorname{sgn}\dot{x}_j$
	Friction (Coulomb)	$\sum_j C_{ij}\operatorname{sgn}\dot{x}_j$
Fluid	-	$\sum_j C_{ij}\lvert\dot{x}_j\rvert\dot{x}_j$

in which M is the mass-inertia matrix, K is the stiffness matrix, $f(t)$ is the excitation vector and finally d is the damping vector component, usually in function of x and $\dot{x}$ (so $d(\dot{x}, x)$.

The previous equation could be analytically solved if the therm d is in function only of $\dot{x}$. As can be seen from Table 6.1, only the Viscous model satisfies this condition. Thus, damping analysis is usually done using this model, which then defines the called *Equivalend Viscous Damping* parameter.

In the case of the Equivalent Viscous model, the resulting equations of motion are

$$M\ddot{x} + C\dot{x} + Kx = f(t) \tag{6.18}$$

6.2.1 Equivalent Viscous Damping Model

For example, a single degree of freedom system subjected to an external excitation can be considered. In this case, the equation of motion for a mass unit is

$$\ddot{x} + 2\zeta\omega_n\dot{x} + \omega_n^2 x = \omega_n^2 u(t) \tag{6.19}$$

With a harmonic excitation, the response of the system is given by

$$x = x_0\cos(\omega t + \phi) \tag{6.20}$$

in which x_0 is the response amplitude and is

$$x_0 = u_0\frac{\omega_n^2}{\sqrt{(\omega_n^2 - \omega^2) + 4\zeta^2\omega_n^2\omega^2)}} \tag{6.21}$$

so the damping energy dissipation (or the *damping capacity*)per mass unit is

$$\Delta U = \oint f_d dx = \int_{-\frac{\phi}{\omega}}^{(2\pi-\phi)\omega} f_d\dot{x}dt \tag{6.22}$$

The damping force f_d, normalized with respect to Equation 6.19, is

Table 6.2: Equivalent Damping formulation for common types of damping in a single *dof* system.

Class of Damping	Type of Damping	damping force $(d(x,\dot{(x)}))$	Eq. Damp. Ratio ζeq
Internal/Material	Viscous	$2\zeta\omega_n\dot{x}$	ζ
	Hysteric	$\frac{c}{\omega}\dot{x}$	$\frac{c}{2\omega_n\omega}$
Structural	-	$c\lvert x\rvert \operatorname{sgn}\dot{x}$	$\frac{c}{\pi\omega_n\omega}$
	Friction (Coulomb)	$c\operatorname{sgn}\dot{x}$	$\frac{2c}{\pi x_0\omega_n\omega}$
Fluid	-	$c\lvert\dot{x}\rvert\dot{x}$	$\frac{4\omega x_0 c}{3\pi\omega_n}$

$$f_d = 2\zeta\omega_n\dot{x} \tag{6.23}$$

and so the *damping capacity* for viscous damping ΔU_v is

$$\Delta U_v = 2\zeta\omega_n \int_0^{\frac{2\pi}{\omega}} \dot{x}^2 dt = 2\pi x_0^2\omega_n\omega\zeta \tag{6.24}$$

In a generic form, for a generic type of damping, the Equation 6.19 becomes

$$\ddot{x} + d(\dot{x}, x) + \omega_n^2 x = \omega_n^2 u(t) \tag{6.25}$$

and so the Equation 6.22 becomes

$$\Delta U = \int_{-\frac{\phi}{\omega}}^{(2\pi-\phi)\omega} d(\dot{x}, x)\dot{x}dt \tag{6.26}$$

in which the therm $d(\dot{x}, x)$ can be replaced with different type given in Table 6.1. In the same manner, the different type of damping reported in Table 6.1 can be normalized to an *Equivalent Damping Ratio* ζ_{eq} as reported in Table 6.2.

If the total energy of the system is assumed U_{max} it is possible to write the *loss factor* η as the damping capacity per damping cycle (in a radiant form)

$$\eta = \frac{\Delta U}{2\pi U_{Max}} \tag{6.27}$$

For a simple viscous damped oscillator, the loss factor is

$$\eta = \frac{2\omega\zeta}{\omega_n} \tag{6.28}$$

As an approximation, for a free decay system, it is possible to assume that $\omega = \omega_d = \omega_n$ so the loss factor

$$\eta = 2\zeta \tag{6.29}$$

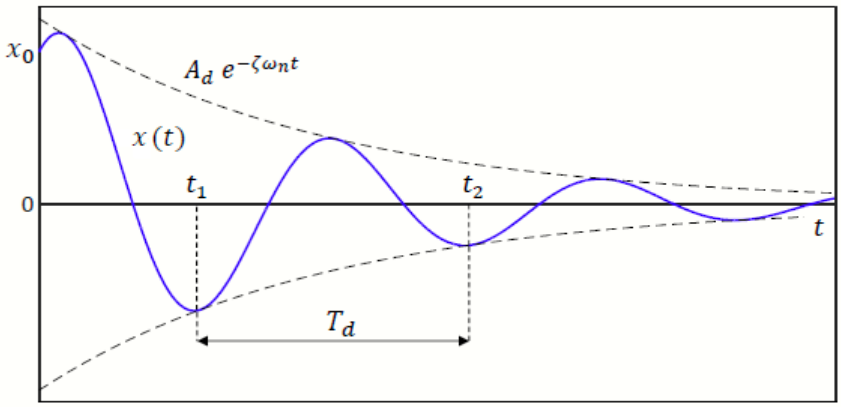

Figure 6.4: Logarithmic Decrement Method time decay.

6.3 Methods for measuring damping

Damping can be represented through various Parameters such as damping capacity, loss factor, damping ratio, etc. as seen in the previous section and Models (Table 6.1 and Table 6.2).

Before making the measurement, it is necessary to choose the model that best represents the system. Next, it is required to determine which parameters to evaluate and by which method.

As mentioned above, this is the most challenging part of the analysis since damping is a highly nonlinear phenomenon not fully understood. Furthermore, many external components influence the measurement, such as air (fluid damping), interfaces, viscoelastic materials in the system, etc.

6.3.1 Logarithmic Decrement Method

The logarithmic decrement method is the simplest method for estimating damping and works in the absence of external forcing, and viscous damping is the only predominant form of energy dissipation. This method determines damping by operating the ratio between the amplitudes of two consecutive peaks in the response considering the acquisition of a signal in the free-response time of a system.

Two instants are considered, t_1 and $t_2 = t_1 + T_D$ with $T_D = 2\pi/\omega_d$. So the response in amplitude, as a function of t_1 and t_2 (Figure 6.4), can be written as

$$\begin{aligned} x(t_1) &= A_d e^{-\zeta\omega_n t_1}\cos(\omega_d t_1 - \phi_d) \\ x(t_2) &= A_d e^{-\zeta\omega_n t_2}\cos(\omega_d t_2 - \phi_d) \end{aligned} \tag{6.30}$$

the fraction between the two responses

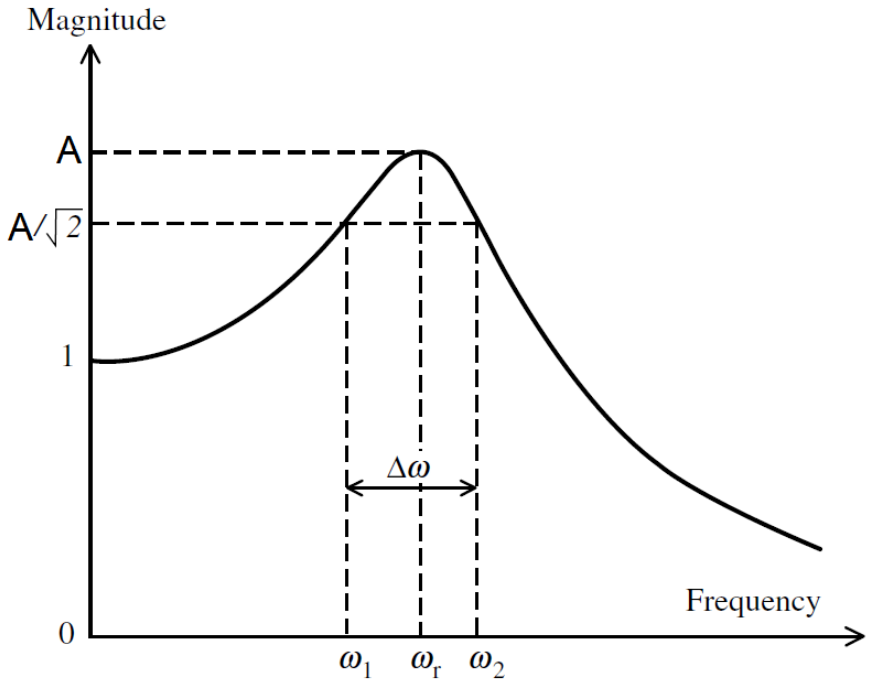

Figure 6.5: Bandwidth Method - frequency response.

$$\frac{x(t_2)}{x(t_1)} = \frac{e^{-\zeta\omega_n(t_1+T_D)}}{e^{-\zeta\omega_n t_1}} = e^{-\zeta\omega_n T_D} = e^{-\frac{2\pi\zeta}{\sqrt{1-\zeta^2}}} \tag{6.31}$$

The ratio between the two peaks depends only on ζ so the logarithmic decrement δ is therefore defined as

$$\delta = ln\frac{x(t_2)}{x(t_1)} = 2\pi\zeta\sqrt{1-\zeta^2} \tag{6.32}$$

Once the amplitudes of the two peaks have been detected, ζ can be calculated from δ with the expression

$$\zeta = \frac{\delta}{\sqrt{4\pi^2+\delta^2}} = \frac{\delta}{2\pi} \tag{6.33}$$

6.3.2 Bandwidth Method

One of the most famous damping estimation methods, based on frequency response, is the Bandwidth Method (also called half-power Method) Figure 6.5.

Starting from the peak frequency ω_r, $\Delta\omega$ could be define as $\Delta\omega = \omega_2 - \omega_1$. ω_1 and ω_2 values can be obtained from the peak amplitude value divided by the root of two, as visible in Figure 6.5.

The damping value is so defined as

$$\zeta = \frac{1}{2}\frac{\Delta\omega}{\omega_r} \tag{6.34}$$

The value of $\sqrt{2}$ corresponds to a decrease of 3 dB respect to the peak amplitude.

6.3.3 Others Method

Several other methods will not be considered, such as the Magnification Factor Method and Hysteresis Loop Method. The following discussion will be conducted using time-domain methods as they are generally more accurate.

6.4 Modified Coulomb Damping Model

In this model, all the different damping types are grouped under three main categories: fluid in nature (including viscous), Coulomb, and hysteretic. The energy dissipation relative to the literature's material is generally treated similarly to the ordinary sliding friction between bodies in contact. For this reason, the Coulomb sliding friction law seen so far is modified here, assuming not a constant kinematic friction coefficient, but rather an internal friction coefficient dependent on the oscillation energy E according to the expression:

$$m\ddot{x} + cm[\frac{2E}{k}]^{\lambda} sgn(\dot{x}) + kx = 0 \tag{6.35}$$

where

$$E = \frac{1}{2}m\dot{x}^2 + \frac{1}{2}kx^2 \tag{6.36}$$

For Coulomb sliding friction $\lambda = 0$. For hysteretic damping dependent on the amplitude $\lambda = 1/2$. For the damping deriving from fluid contributions, always dependent on the oscillation amplitude, $\lambda = 1$.

It is possible to rewrite the equation in canonical form to include the Q factor, obtained for the three cases in which the only damping component considered is predominant. For the case of hysteretic damping ($\lambda = 1/2$), the equation becomes:

$$\ddot{x} + \frac{\pi\omega}{4Q_h}\sqrt{\omega^2x^2 + \dot{x}^2}sgn(\dot{x}) + \omega^2 x = 0 \tag{6.37}$$

Case $\lambda = 1$ (fluid)

$$\ddot{x} + \frac{\pi}{4y_0 Q_{f0}}(\omega^2 x^2 + \dot{x}^2) sgn(\dot{x}) + \omega^2 x = 0 \tag{6.38}$$

With y_0 initial amplitude of x and Q_{f0} initial value of Q at the beginning of the oscillation. Experimentally it has been verified that the factor Q increases with the reduction of the amplitude during the oscillation. On the contrary, the Q of an oscillator influenced only by Coulomb friction (sliding, $\lambda = 0$) decreases with the amplitude, and the equation takes the following form:

$$\ddot{x} + \frac{\pi\omega^2 y_0}{4Q_{c0}} sgn(\dot{x}) + \omega^2 x = 0 \tag{6.39}$$

The subscript zero identifies the initial value of the time-varying factor Q. Obviously, it is possible for an oscillator to be affected by all three types of damping simultaneously. The inherent motion equation is therefore the composition of the previous ones:

$$\ddot{x} + [\frac{\pi\omega^2 y_0}{4Q_{c0}} + \frac{\pi\omega}{4Q_h}\sqrt{\omega^2 x^2 + \dot{x}^2} + \frac{\pi}{4y_0 Q_{f0}}(\omega^2 x^2 + \dot{x}^2)] sgn(\dot{x}) + \omega^2 x = 0 \tag{6.40}$$

The analytical solution for the dependence on time of the maximum amplitude of the decay, when all the factors $Q >> 1$ (low damping), is obtained from energy considerations. It can be noted that the change in energy over time is zero in the absence of friction.

$$\dot{E} = \frac{d}{dt}(\frac{1}{2}m\dot{x}^2 + \frac{1}{2}kx^2) = \dot{x}(m\ddot{x} + kx) = 0 \tag{6.41}$$

dE/dt is determined by the amount of work in contrast to the friction force and is proportional to $\omega y f$ where f is the friction force. For Coulomb friction, f is constant and so dE/dt is proportional to $E^{1/2}$. For hysteretic damping, dE/dt is proportional to E^1 and for fluid damping dE/dt is proportional to $E^{3/2}$.

The general case is so described by

$$\dot{E} = -(c_1 + c_2\sqrt{E} + c_3 E)\sqrt{E} \tag{6.42}$$

For the time-varying amplitude, it is possible to write the equation in this form

$$\dot{y} = -c - by - ay^2 \tag{6.43}$$

In which a, b, and c are constants. The solution, in the case the Coulomb damping is not predominant, and using $r = \sqrt{(b^2 - 4ac)}$ where $4ac < b^2$ and considering

$$\begin{aligned} \alpha &= 2ay_0 + b - r \\ \beta &= 2ay_0 + b + r \\ p &= \frac{\alpha}{\beta} e^{-rt} \end{aligned} \tag{6.44}$$

the solution is

$$y = \frac{b(p-1) + r(p+1)}{2a(1-p)} \tag{6.45}$$

for the case in which $c = 0$, the previous Equation 6.45 can be write as

$$\frac{1}{y} = (\frac{a}{b} + \frac{1}{y_0})e^{bt} - \frac{a}{b} \tag{6.46}$$

for the case in which $a = 0$, the previous Equation 6.45 can be write as

$$y = (y_0 + \frac{c}{b})e^{-bt} - \frac{c}{b} \tag{6.47}$$

Finally, this equation can be used in the fitting software to determine parameters a, b, and c. Subsequently, zeroing the parameters a and c and solving the equation with the value found of b, we can obtain the value of ζ.

Chapter 7

Experimental Damping Analysis

7.1 Introduction and Instrumentation

The damping is measured through specific instrumentation and the use of specific software for data processing. In this thesis, instrumentation owned by the University of Bologna and Reglass H.T. Srl (Italy), which kindly gave availability, have been used.

Before performing the analyzes, it is necessary to establish a setup and not change it during the entire analysis. At the current state of the art, the measurement of damping is exclusively comparative. Tests were carried out on specimens of different materials mounted on cantilever support, characterizing each of them' vibratory behavior and validating the damping models. The setups of the tests carried out are briefly reported below.

The laser detector (Figure 7.1) works with signals in analog form from which it is possible to obtain acceleration, speed, and displacement of the sample concerning its quiet position. Subsequently, thanks to the converter, the signal is converted into a digital one. The measurement includes a specific offset corresponding to the initial pointer-specimen distance; this will be discussed later. The drivers necessary for its use with Matlab were then downloaded, and then a script already available was used for reading and acquiring the signals from the latter. All the instruments used are shown in detail in the next Chapter.

A unidirectional prepreg specimen, one of SMC (short fiber composite made by Sheet Moulding Compound), and one in aluminum were analyzed to validate the mathematical models. All the samples were equipped with tape on end to ensure that the laser did not have reading problems due to reflected beams. Therefore, the setup was completed by locking the detector position and connecting it appropriately to the control unit via the CAN line. The specimen was cantilevered, blocking its movement with bolted joints. The excitement was provided through

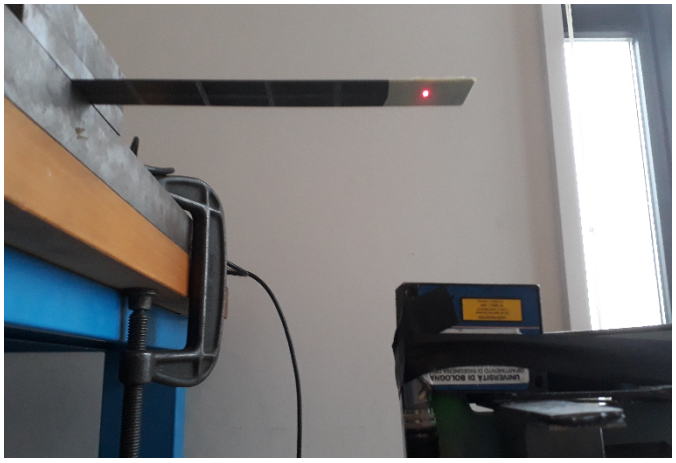

(a) Cantilever setup.

(b) Laser sensor.

Figure 7.1: Basic setup for comparative tests and validation.

```
close all; clearvars; clc;
% -------------------- Acquisizione segnale dall'Excel ------------------- %

[t,y]=ImportaSegnale('Segnale Onda - 1');
```

(a) Main function.

```
function [x,y]=ImportaSegnale(Nomefile)
% Passandole il nome del file excel in cui è contenuto il segnale la funz
% immagazzina in due vettori colonna x ed y il tempo e lo spostamento
% rispettivamente.
% ------------------------------------------------------------------------
x=xlsread(Nomefile,'A:A');
y=xlsread(Nomefile,'B:B');
end
```

(b) Import function.

Figure 7.2: Starting code.

the use of different weights resting on the end of the sample.

After the validation of the software and the mathematical models, it was possible to analyze the behavior of innovative composite materials (next Chapter) with rubber nanofibers to increase the damping of the specimens. It was also possible to evaluate the vibratory and damping behavior of innovative hybrid metal-carbon tubes with a viscoelastic interface. These tubes, used as mandrels in the printing industry, require high damping. This part will be explored deeply in the next Chapter.

7.2 Software and GUI

7.2.1 Signal Acquisition and first operations

As previously mentioned, the editor used for writing the software was Matlab. The code was first developed without a graphical interface, and subsequently, a GUI was adapted on the code.

The analysis starts from an Excel file bearing the signal samples acquired by the laser detector, respectively. The syntax of the code used was as intuitive as possible at the beginning to extract the values. The signal import function (visible in Figure 7.2) has the purpose of putting time (s) and amplitude (m/s^2) in two one-dimensional arrays, using a simple predefined reading function for columns, different for the two formats. The same function was called at the beginning of a main program. This way of proceeding was adopted several times during the drafting of the code.

The software performs the second function. It derives the fundamental param-

```
1   function [num_campioni,int_osservaz,ts,fs,max_risposta,min_risposta]=GetSignParam(t,y)
2 -   num_campioni=length(t);
3 -   int_osservaz=0;
4 -   ts=0;
5 -   for i=1:num_campioni-1
6 -       ts=t(i+1)-t(i);
7 -       int_osservaz=int_osservaz+ts;
8 -   end
9 -   ts=int_osservaz/(num_campioni-1);
10 -  fs=1/ts;
11 -  max_risposta=max(y);
12 -  min_risposta=min(y);
13 -  end
```

Figure 7.3: Signal parameters function.

eters of the signal, such as the sampling frequency, the signal length, the number of samples, maximum and minimum amplitudes, etc. (Figure 7.3). The signal was sampled at regular intervals, so the cycle shown in Figure 7.3 could be simplified by simply inserting $t(2) - t(1)$. The for loop way is preferred to perform further checking. The parameters obtained from this stage will be used later.

The third function (Figure 7.4), in order of execution, provides for the initial cut of the signal to eliminate the noise existing between the start of the acquisition and the start of the free response of the specimen. An energy method was used to cut the signal entirely automatically. The integral of the signal was carried out and, after establishing a percentage value of amplitude below which to cut, a new signal is recreated without the first part of noise. In a second revision of the code, it was noted that the part from lines 16 to 24 can be simplified by directly cutting the vectors without creating a new one, optimizing the software.

It was then necessary to center the signal on the x-axis to prevent alignment errors of the data acquired by the laser on the reference position. The amplitude offset is operated with a specific function visible in Figure 7.5. The code averages the signal amplitudes and then subtracts that same average from each amplitude value. Thus, a new vector is stored and centered on the abscissa axis but utterly unchanged in its performance. Figure 7.6b shows the differences in the case of offset execution on a signal acquired with the laser, before and after processing. The difference is visible on the ordinates of the two graphs.

The *signal cutting function* was adopted for excluding from the the original signal the part in which the excitation has occurred. The vibration transient is now exhausted from the interpolation of data by damping models. It was chosen to have the user manually enter the instant of start and end of the window of interest, in milliseconds. A suitable algorithm (Figure 7.7) was created to take the samples closest to the time instants entered and thus obtain the signal in the desired time window.

```
function [t_int,y_int,taglio_iniz,time_offset_i] = CutOff(t,y)
%  Per trovare il campione in cui si opera il taglio del segnale e
%  l'offset temporale iniziale, sulla base di considerazioni
%  energetiche ad ogni step di calcolo.
% -------------------------------------------------------------------------
[num_campioni,~,ts,~,~,~] = GetSignParam(t,y);
e_y      = zeros(num_campioni,1);
e_y(1,1) = ts*(abs(y(1,1)))^2;
taglio_iniz = 0;
for i=1:num_campioni-1
    e_y(i+1,1) = e_y(i,1)+ts*(abs(y(i+1,1)))^2;
    if e_y(i,1)<0.05 && e_y(i+1,1)>0.05
        taglio_iniz = i;
    end
end
time_offset_i = ts*taglio_iniz;

t_int = zeros(num_campioni-taglio_iniz,1);
y_int = zeros(num_campioni-taglio_iniz,1);
for i=1:num_campioni-taglio_iniz
    t_int(i,1) = t(taglio_iniz+i,1)-time_offset_i;
    y_int(i,1) = y(taglio_iniz+i,1);
end
end
```

Figure 7.4: Cut off function.

```
function [sign] = OffsetAmp(s)
rs = 0;
n = ceil((s.info.fs*s.info.int_osservaz)/2);
for i=(s.info.num_campioni-n):s.info.num_campioni
    rs = rs+s.dat.y(i,1);
end
rm = rs/n;  % media ampiezze
sign.dat.y = s.dat.y(1:end,1)-rm;
sign.dat.t = s.dat.t;

[num_campioni,int_osservaz,ts,fs,max_risposta,min_risposta] = GetSignParam(sign.dat.t,sign.dat.y);
sign.info.num_campioni = num_campioni;
sign.info.int_osservaz = int_osservaz;
sign.info.ts           = ts;
sign.info.fs           = fs;
sign.info.max_risposta = max_risposta;
sign.info.min_risposta = min_risposta;
end
```

Figure 7.5: Offset function.

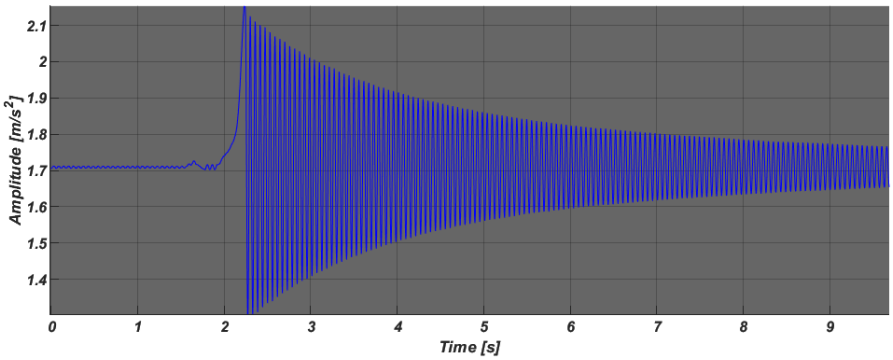

(a) Original.

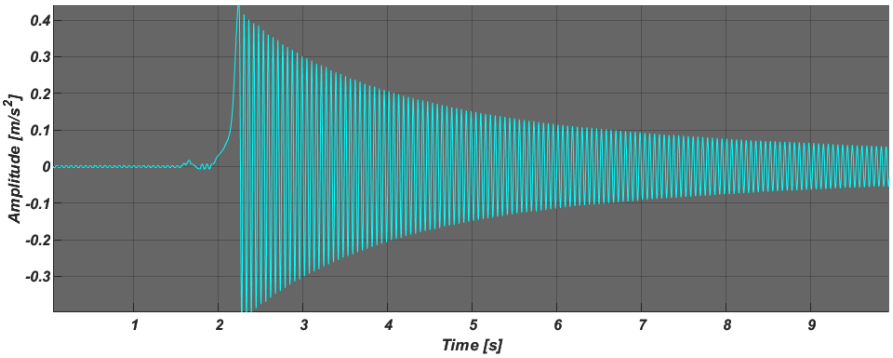

(b) Off-set.

Figure 7.6: Comparison between original and offset-signal.

```
function [sign] = Finestra(s,time_i,time_f)
time_iniz = time_i;
time_fin  = time_f;
start_sample = 0;
end_sample   = 0;
for i=1:s.info.num_campioni
    if time_iniz>=s.dat.t(i,1) && time_iniz<s.dat.t(i+1,1)
        start_sample = i;
    end
    if time_fin>=s.dat.t(i,1) && time_fin<s.dat.t(i+1,1)
        end_sample = i;
    end
end
InitialCut = s.dat.t(start_sample+1,1);
for i=1:end_sample-start_sample
    sign.dat.t(i,1) = s.dat.t(i+start_sample,1)-InitialCut;
    sign.dat.y(i,1) = s.dat.y(i+start_sample,1);
end
[num_campioni,int_osservaz,ts,fs,max_risposta,min_risposta] = GetSignParam(sign.dat.t,sign.dat.y);
sign.info.num_campioni = num_campioni;
sign.info.int_osservaz = int_osservaz;
sign.info.ts           = ts;
sign.info.fs           = fs;
sign.info.max_risposta = max_risposta;
sign.info.min_risposta = min_risposta;
return;
end
```

Figure 7.7: Window-cut function.

```
function [s]=TransformSignal(s)
NFFT = 2^nextpow2(s.info.num_campioni);
% Next power of 2 from length of y: da qualche step in più per facilitare algoritmo fft
Y = fft(s.dat.y,NFFT)/s.info.num_campioni;
% Discrete Fourier Transform divided by num_campioni: da i coefficienti della serie di Fourier
% ovvero le ampiezze per cos e sin ad ogni frequenza
f = s.info.fs/2*linspace(0,1,NFFT/2+1);

fris_fft=f(2);  % risoluzione in frequenza fft

nfmax=1;    % Impongo limite frequenza da analizzare
for i=1:length(f)
  if f(i)<s.info.fs/2
    nfmax=nfmax+1;
  else
      break
  end
end

s.f=f;
s.Y=Y;
s.freq_res=fris_fft;
s.nfmax=nfmax;
end
```

Figure 7.8: FFT funcion.

7.2.2 FFT and filtering

After the previous functions, it is now possible to do the actual analysis of the signal. The Fast Fourier Transform (FFT) was adopted to carry out analyzes in the frequency domain on the signal sampled at regular intervals. Fortunately, this function is already integrated into Matlab, so the script was simple to implement (Figure 7.8). Besides, band-pass filters have been added to eliminate any noise present in the signal and harmonic components outside the range considered. The frequency response of a typical signal is visible in Figure 7.9.

A simple mathematical function to derive the resonance peaks was used to search for the maximum value within a range (Figure 7.10).

7.2.3 STFT, Spectrogram and Decay

The Short-Time Fourier Transform (STFT) was also adopted to evaluate the trend of amplitudes over time. Thanks to the Matlab function called Spectrogram, it was possible to analyze the time domain peaks by appropriately setting the function parameters. These parameters (window length, overlap, zero-padding, window type) have often been obtained experimentally based on the type of signal acquired (Figure 7.11).

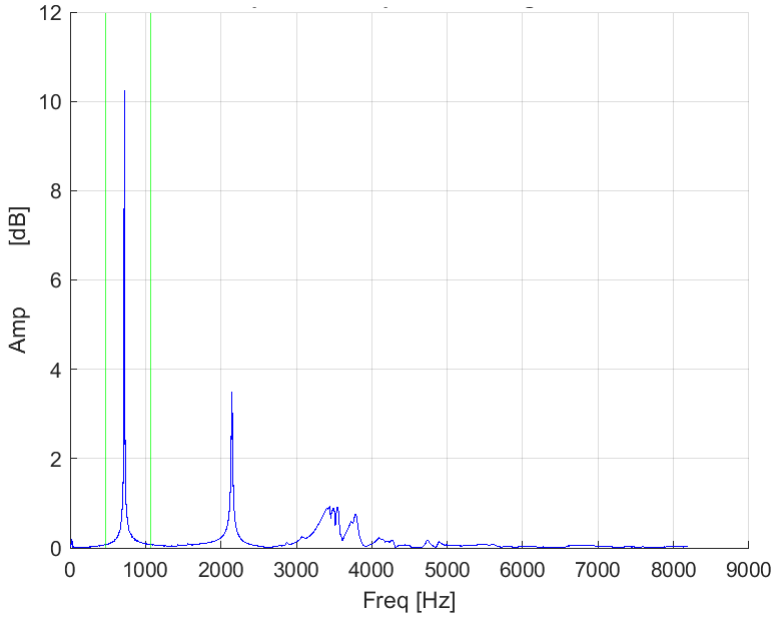

Figure 7.9: Frequency response.

```
function [freq,ampl]=DetectResFreq(s,f_inf,f_sup)
k=0;
for i=1:length(s.f)
    if s.f(1,i)>f_inf && s.f(1,i)<f_sup
        k=k+1;
        fl(k)=s.f(1,i);
        Yl(k)=2*abs(s.Y(i,1));
    end
end
[pks,loc]=findpeaks(Yl,fl);
[ampl,pos]=max(pks);
freq=loc(pos);
end
```

Figure 7.10: Resonance peaks searching function.

```
function [sign] = ZeroPadding(s,f_res,growfin,growpoints,growoverlap)
Lfinestre = 1/f_res*growfin;                    % Spectrogram  uses nswindow to  divide the sign
nswindow  = 2^nextpow2(s.info.fs*Lfinestre);    % into segments and perform windowing.
nsnfft    = nswindow*growpoints;                % Spectrogram uses nsnfft sampling points to cal
nsoverlap = ceil(nswindow*growoverlap);         % Spectrogram uses nsoverlap samples of overlap

% Spettrogramma sul segnale filtrato: ------------------------------------
% S - (Matrice (n°complessi)) STFT del segnale yfilt. Ogni colonna di S è una
%     stima del termine della trasformata in un diverso istante di tempo.
%     Ogni riga contiene il valore della trasformata ad un certo valore di frequenza.
% F - Vettore colonna delle frequenze cicliche in cui è calcolato lo spettrogramma.
% T - Vettore riga degli istanti di tempo in cui è calcolato lo spettrogramma
% P - (Matrice con stesse dimensioni di S) I suoi termini contengono i
%     valori del power spectrum (o power spectral density PSD) di ogni
%     segmento. (Il num complesso per il suo complesso coniugato, se ne si
%     facesse la radice quadrata si otterrebbe il suo modulo/ampiezza).
%     (Matrice di valori reali).
[S,F,T,P] = spectrogram(s.dat.yfilt,hamming(nswindow),nsoverlap,nsnfft,s.info.fs);

% Fris_stft = F(2);           % risoluzione in frequenza della STFT
% Tris_stft = T(3)-T(2);      % risoluzione nel tempo della STFT
```

Figure 7.11: STFT function start.

Particular attention had to be paid to the type of window. The application of the window alters the values of the actual amplitudes of the signal. The Effective Noise Bandwidth (ENBW), to recover the real value of the amplitudes, is calculated according to the formulas corresponding to the Hamming Window [71], the window used for the STFT (Figure 7.12).

In the last instance, anti-aliasing filtering was carried out again. With a small addition to the code, the sample relating to the resonance peak identifiable in the Spectrogram was stored, so that it could then be highlighted in its graph (Figure 7.13).

Subsequently, the analysis of the amplitudes of the first natural frequency was

```
% Peso funzione finestra (Hamming window) -> val ampiezze reale
s1 = 0;
for j=0:(nswindow-1)
    s1 = s1+0.54-0.46*cos(2*pi*j/nswindow);
end
s2 = 0;
for j=0:(nswindow-1)
    s2 = s2+(0.54-0.46*cos(2*pi*j/nswindow))^2;
end

ENBW = s.info.fs*s2/(s1^2); % peso funzione finestra
```

Figure 7.12: Hamming Window amplitude correction function.

```
35      % ---- Impongo limite frequenza massima da analizzare e trovo le ampiezze
36      % ---- corrispondenti alle armoniche in frequenza di risonanza nello
37      % ---- spettrogramma a sezioni nel tempo.
38 -    r = length(F);
39 -    nfmax = 2;
40 -    trova_res = 0;
41 -    verify_res = zeros(r,1);
42 -    for i=2:r
43 -      if F(i)<s.info.fs/2
44 -          nfmax = nfmax+1;
45 -      else
46 -          break
47 -      end
48 -      verify_res(i,1) = abs(F(i)-f_res);
49 -      if verify_res(i,1)<verify_res(i-1)
50 -          trova_res = i;
51 -      end
52 -    end
53      % ------ Salvataggio parametri spettrogramma nella struttura dati ----- %
54 -    sign.S = S;
55 -    sign.F = F;
56 -    sign.T = T;
57 -    sign.P = P;
58 -    sign.ENBW  = ENBW;
59 -    sign.nfmax = nfmax;
60 -    sign.trova_res = trova_res;
61 -    sign.windowLength = nswindow;
62 -    sign.npointSTFT   = nsnfft;
63 -    sign.overlap      = nsoverlap;
64
65 -    end
```

Figure 7.13: STFT function end.

```
function [sign] = GetTimeDecay(s)
r = length(s.T);   % Si usa qui la lunghezza del vettore tempo (vett. riga).
ff = zeros(1,r);   % Inizializzazione vettori di dati.
aa = zeros(1,r);
for i=1:r
    [~,I] = max(s.P(:,i)); % è il valore massimo del modulo della trasformata per l'istante i.
    ff(1,i) = s.F(I);                          % freq corrispondente all'ampiezza massima in qu
    aa(1,i) = sqrt(max(s.P(:,i))*s.ENBW*2);    % ampiezza massima in quell'istante temporale.
end
sign.freq = ff;         % freq dove si ha l'ampiezza massima nell'istante di tempo.
sign.fn   = median(ff); % freq modo: valore di frequenza più frequente.
sign.temp = s.T;        % vettore degli istanti di tempo.
sign.amp  = aa;         % vettore delle ampiezze massime (in ogni istante).
end
```

Figure 7.14: Amplitude peaks extracting function.

carried out over time. Once the decay of the amplitudes over time was obtained with a simple extraction function (Figure 7.14), it is possible to apply the damping models previously reported subsequently. The decay over time of a signal relating to a fair and correct excitation is qualitatively shown in Figure 7.15.

7.2.4 Fitting of Damping Models

Lastly, the code for data interpolation according to various models has been written. Since the signal over time can be decidedly long, another signal selection and cutting function has been implemented. In this way, it was possible to select only some specific parts of the signal to be interpolated (Figure 7.16).

Matlab already has all the functions necessary to fit the curves according to various logics. In Figure 7.17, for example, the equation of the Modified Coulomb model is reported, with the coefficients of fluid damping a, hysterical damping b, r, and the initial amplitude y_0. The variable r was used instead of the friction damping coefficient c not to have an excessively long string, more than it already was. c was obtained by inverse formula at a later time.

Moreover, the coefficients must have adequate boundary conditions and initial values for convergence to the result. This can be specified in the fit function by the interpolation options passed to the input. For this purpose, the opts structure was defined by the fitoptions function, containing the starting values and the real limits of the coefficients (which therefore did not lead to complex solutions or trivial solutions). Another option specified in opts was present to ensure interpolation without the excessive overhang of the derivative and speed up convergence. The opts structure was then moved to the fit routine for interpolation. Finally, a structure was obtained with the coefficients of the model. Therefore, the values were extracted and replaced in the expression of the model itself to obtain the interpo-

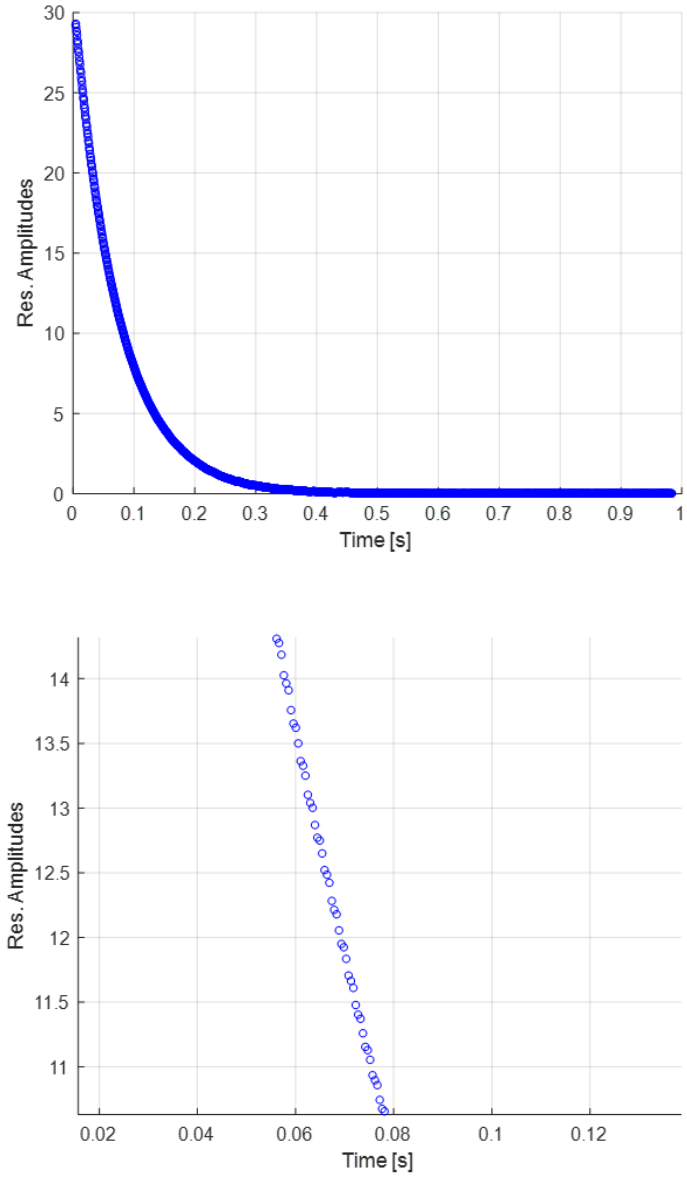

Figure 7.15: Amplitude decay of the peaks over time.

```
118 -    tempo_i = input('Inserire l''istante di tempo iniziale dal quale si vuol far partire il fitting
119 -    tempo_f = input('Inserire l''istante di tempo finale per il fitting [ms]\n');
120 -    t_iniz = tempo_i/1000;    t_fin = tempo_f/1000;
121
122 -    t_res = s.selected.timeDecay.temp(1,2)-s.selected.timeDecay.temp(1,1);
123 -    t_start = 1; t_end = 1;
124 -    for i=1:length(s.selected.timeDecay.temp)
125 -        if s.selected.timeDecay.temp(1,i)>=t_iniz && s.selected.timeDecay.temp(1,i)<t_iniz+t_res
126 -            t_start = i;
127 -        end
128 -        if s.selected.timeDecay.temp(1,i)>=t_fin && s.selected.timeDecay.temp(1,i)<t_fin+t_res
129 -            t_end = i;
130 -        end
131 -    end
132
133 -    s.selected.timeDecay = CurveFit(s.selected.timeDecay,t_start,t_end);
```

Figure 7.16: Interval of interpolation function.

lating curve. Figure 7.18 shows an example of an interpolated signal according to the Modified Coulomb model.

Since all the architecture necessary for implementing several damping models in the software has been built, the classic viscous damping model has also been implemented. As seen in the previous Chapter, this model is one of the simplest and simplifies the problem. In the subsequent analyzes, a comparison of the models will be made.

An algorithm for this model has been written and is shown in Figure 7.19. As can be seen, the procedure is similar to the previous one. Once the equation of the model has been defined, it is passed to Matlab's fit function, the boundary conditions and the start point of the single coefficient are set, and through the fitting, the value is obtained. Once the value has been extracted, the interpolated curve can be recreated and superimposed on the points.

7.3 Validation

7.3.1 Fictitious signals

As mentioned in the previous section, tests to verify the program have been carried out. For this reason, fictitious signals were generated through a specially designated script. An example is visible in Figure 7.20. A vector of spaced equal time samples has been defined with a function. It is therefore immediate to obtain the number of samples, the frequency, and the sampling period. Amplitudes, pulsations, and phases were then written to simulate two harmonics, and with the time values, the corresponding signal amplitude samples were obtained. This resulted

```
function [s] = CurveFit(s,t_start,t_end)
ft   = fittype('(b*((2*a*y0+b-r)/(2*a*y0+b+r)*exp(-r*x)-1)+r*((2*a*y0+b-r)/(2*a*y0+b+r)*exp(-r
opts = fitoptions( ft );
opts.Display = 'Off';

% Limiti & Star point: a, b, r, y0.
% Limite r. r>0 per evitare soluzioni complesse e crash del fitting.
opts.Lower = [1e-10 1e-20 1e-20 0];   % Limiti dei coefficienti : a b r y0 rispettivamente.
opts.StartPoint = [0 0 0 0];
opts.Upper = [1000 1000 1000 100*s.amp(1,t_start)];

opts.Robust = 'Bisquare';

[curva,~] = fit(s.temp(1,t_start:t_end)',s.amp(1,t_start:t_end)', ft, opts );
a  = curva.a;           % Coeff Smorz Fluido
b  = curva.b;           % Coeff Smorz Isterico
r  = curva.r;           % Coeff r
c  = (b^2-r^2)/(4*a);   % Coeff Smorz Coulomb
y0 = curva.y0;          % Ampiezza iniziale
```

```
tempfit = s.temp(1,t_start:t_end);   % Inizializzazione vettori
ampfit  = zeros(1,t_end-t_start+1);  % della curva interpolante.

for i=1:t_end-t_start+1
    ampfit(1,i) = (b*((2*a*y0+b-r)/(2*a*y0+b+r)*exp(-r*tempfit(1,i))-1)+...
                   r*((2*a*y0+b-r)/(2*a*y0+b+r)*exp(-r*tempfit(1,i))+1))/...
                  (2*a*(1-(2*a*y0+b-r)/(2*a*y0+b+r)*exp(-r*tempfit(1,i))));
end
s.damp.a = a;
s.damp.b = b;
s.damp.c = c;
s.damp.y0 = y0;
s.tempfit   = tempfit;
s.ampfit    = ampfit;
end
```

Figure 7.17: Interpolation (Fitting) function.

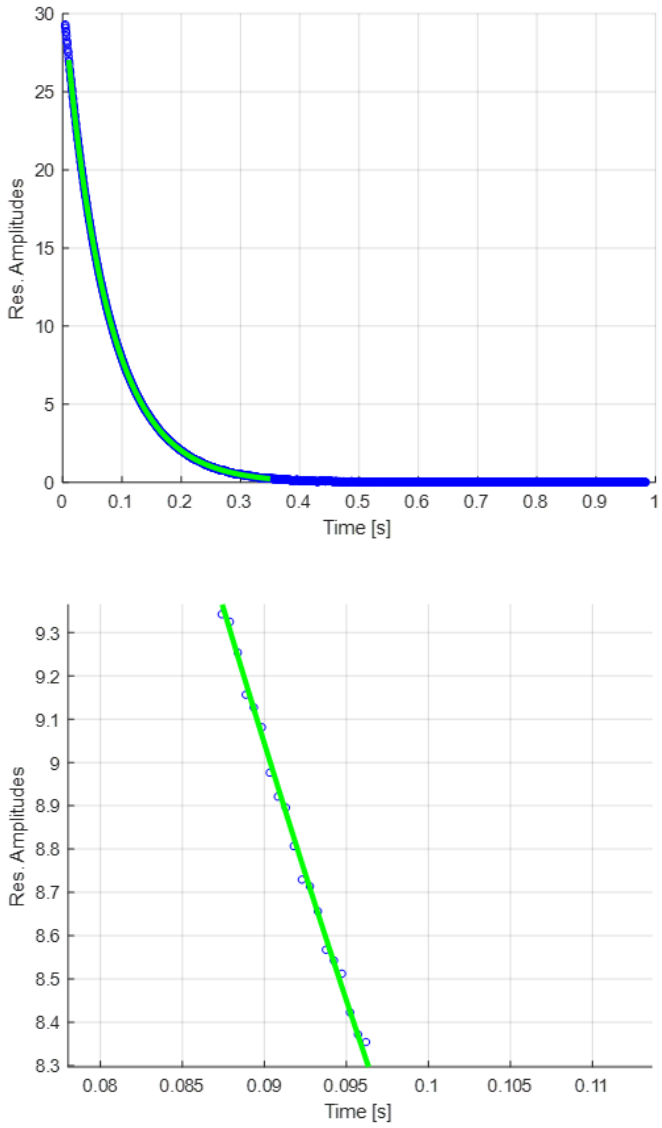

Figure 7.18: Decay (blue) and interpolating model (green).

```
function [s] = CurveFitViscous1(s,t_start,t_end,y0,freq_res)
leggepr  = 'y0*exp(-xeta*2*pi()**x)';
leggepr1 = strrep(leggepr,'y0',num2str(y0));
legge    = insertAfter(leggepr1,'()*',num2str(freq_res));
ft   = fittype(legge,'independent','x','dependent','y','coefficients',{'xeta'});
opts = fitoptions( ft );
opts.Display = 'Off';

% Limiti & Star point: xeta
% Limite xeta. Deve essere compreso fra 0 e 1.
opts.Lower      = 1e-10;   % Limiti coefficienti : xeta.
opts.StartPoint = 1e-10;
opts.Upper      = 0.9999999;

opts.Robust = 'Bisquare';

[curva,~] = fit(s.temp(1,t_start:t_end)',s.amp(1,t_start:t_end)', ft, opts );
xeta = curva.xeta;     % Coef Smorz Viscoso

tempfit = s.temp(1,t_start:t_end);
ampfit = zeros(1,t_end-t_start+1);

for i=1:t_end-t_start+1
    ampfit(1,i) = y0*exp(-xeta*2*pi()*freq_res*tempfit(1,i));
end
s.damp.y0   = y0;
s.damp.xeta = xeta;
s.damp.freq = freq_res;
s.tempfit = tempfit;
s.ampfit  = ampfit;
end
```

Figure 7.19: Viscous model fit function.

```
clearvars;  close all;  clc;

%-------------------------------------------
t   = linspace(0,10,1000);  % [s]
% t è un vettore tempo equispaziato di 1000 campioni.
% t va da zero a dieci secondi con step 0.01 s in questo caso.
% ---> 0.01 s è Ts: il periodo di campionamento.
% ---> La frequenza di campionamento sarà fs.
% ---------> fs = 1/Ts = 100 Hz. <--------
% Definisco le variabili.
num_campioni = length(t);
Ts = t(1,end)/length(t);
fs = 1/Ts;
% Creo il segnale.
A1   = 30;           % [m] Ampiezze.
A2   = 20;
wn1  = 9*pi;         % [rad/s] Pulsazioni segnale.
wn2  = 3*pi;
fn1  = wn1/(2*pi);   % Questa è la frequenza naturale del segnale: %
fn2  = wn2/(2*pi);
phi1  = pi/2;         % [rad] Questa è la fase.
phi2  = pi/4;

Xcf = A1*cos(wn1*t - phi1)+A2*cos(wn2*t-phi2);  % Segnale
```

Figure 7.20: Fictitious signals generation function.

in a fictitious signal, however simple, with known natural frequencies and known damping.

By analyzing the signals generated in a fictitious way with the previously illustrated software, the same damping values were obtained (in addition to the other parameters). They were the first validation of the software. The second, however, concerns the models and the experimental part.

7.3.2 Real signals

Experimental tests have been performed to validate the software and compare the implemented models. In particular, reference specimens (Figure 7.21) were examined, and weights and flaps were added in the cantilever damping test. These additions were made to verify the modified Coulomb model. For example, if a flap is added (pasting it on), the fluid damping of the specimen (the coefficient a) should increase with respect standard configuration while the coefficient b (material) should remains the same. Conversely, with the classic viscous model, the addition of weights or flaps is expected to significantly change the material damping, thus making the damping analysis very prone to errors. The model is expected to show a consistent result between the two tests.

Exaggeratedly large values of the constant c, which directly binds the amplitude

Figure 7.21: Specimen with flap pasted to increase the fluid damping.

to the energy dissipated by the sliding friction with other bodies (Coulombs), are considered unusable or otherwise without physical sense. The reason is that the implemented differential equation was obtained mathematically, assuming Coulomb damping relating to the sliding between bodies not preponderant for the others, with a value of the coefficient c of at least one order magnitude lower than the product ab. This assumption should not be a problem in the tests, nearly for two reasons: blocking with bolts on one end of the beam certainly involves relative movements between the specimen and the locking bracket. Secondly, as mentioned, in literature, it is found experimentally that the presence of a sliding dissipation tends to be of the "all or nothing" type. Therefore, we expect results that confirm virtually negligible values of c, especially concerning ab, with b coefficient that links the amplitude to the energy dissipation due to the material.

Table 7.1 summarizes the numerical results of the damping tests. Figure 7.22 instead represents the values obtained graphically.

It can be noticed, especially from Figure 7.22, that the damping value ζ obtained according to the viscous model is generally higher than that obtained with the Modified Coulomb model. This discrepancy is because the viscous model assimilates all the phenomena (linear and nonlinear) that condition the damping in a single value.

It can be seen that the Modified Coulomb model returns an almost constant damping value of the material even under different conditions. Its ability to split the fluid and friction component from that material is therefore potent. Therefore, the software and models can be considered valid in the first instance, having

Table 7.1: Damping test results with different model, flaps and weights on aluminum specimens.

Test Type	Modified Damping Model ζ	Viscous Model ζ
Aluminum Weight 1	0.001750	0.002351
Aluminum Weight 2	0.001811	0.002463
Aluminum Weight 3	0.001907	0.002670
Aluminum Flap 1	0.001845	0.002710
Aluminum Flap 2	0.001956	0.003227
Aluminum Flap 3	0.001975	0.003712

Table 7.2: Damping test results with different model, flaps and weights on UD specimens.

Test Type	Modified Damping Model ζ	Viscous Model ζ
UD Weight 1	0.002291	0.002750
UD Weight 2	0.002078	0.002540
UD Weight 3	0.002160	0.002706
UD Flap 1	0.002112	0.003972
UD Flap 2	0.002260	0.004068
UD Flap 3	0.002572	0.005079

obtained consistent results. In subsequent tests, both models will always be used to have a comparison between the results.

For completeness, the results obtained with tests on unidirectional prepreg material (Table 7.2) and SMC (Table 7.3) are also reported.

7.4 Appendix: Graphical User Interface (GUI)

The graphical interface is simply the mask of the functions seen in the previous sections. Initially, the GUI appears as shown in Figure 7.23. The only push button ("pick signal") allows the user to select the data file to be analyzed. Once pressed, the functions previously seen are launched as the signal import function and the signal parameters function.

The result of this operation is visible in Figure 7.24.

Subsequently, the signal is windowed, and the offset on the x-axis is done. The functions performed are the cut off function, the offset function, and the Window-cut function. Results visible in Figure 7.25.

After processing the signal in the first part, it is now possible to perform the FFT and analyze it in the frequency domain (7.26). The functions performed are

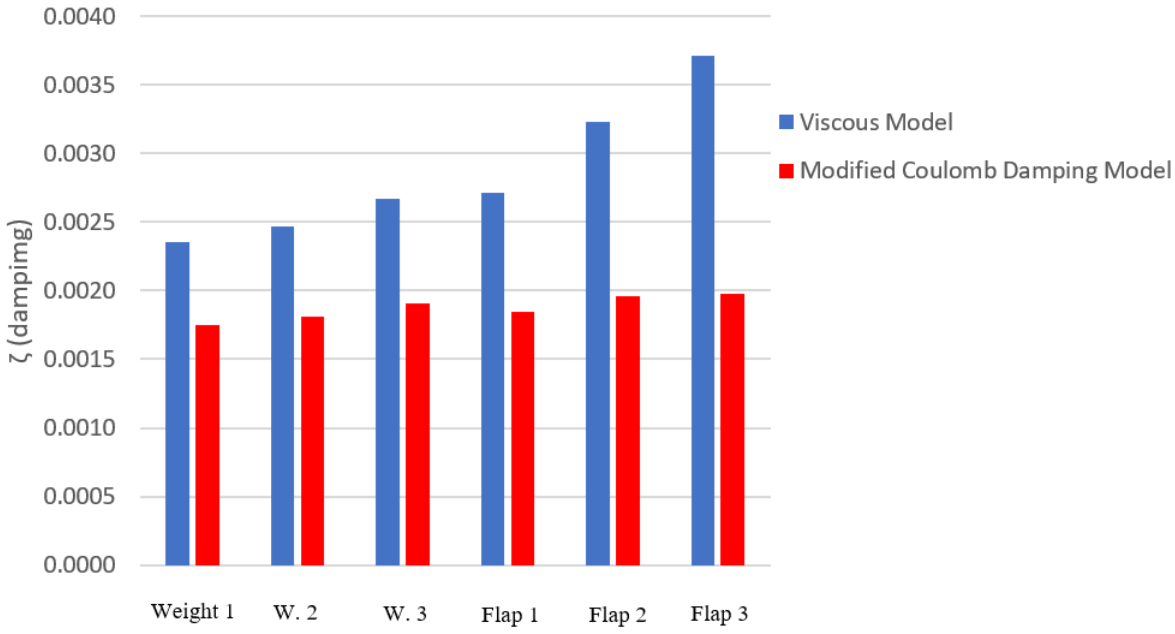

Figure 7.22: Damping test results with different model, flaps and weights.

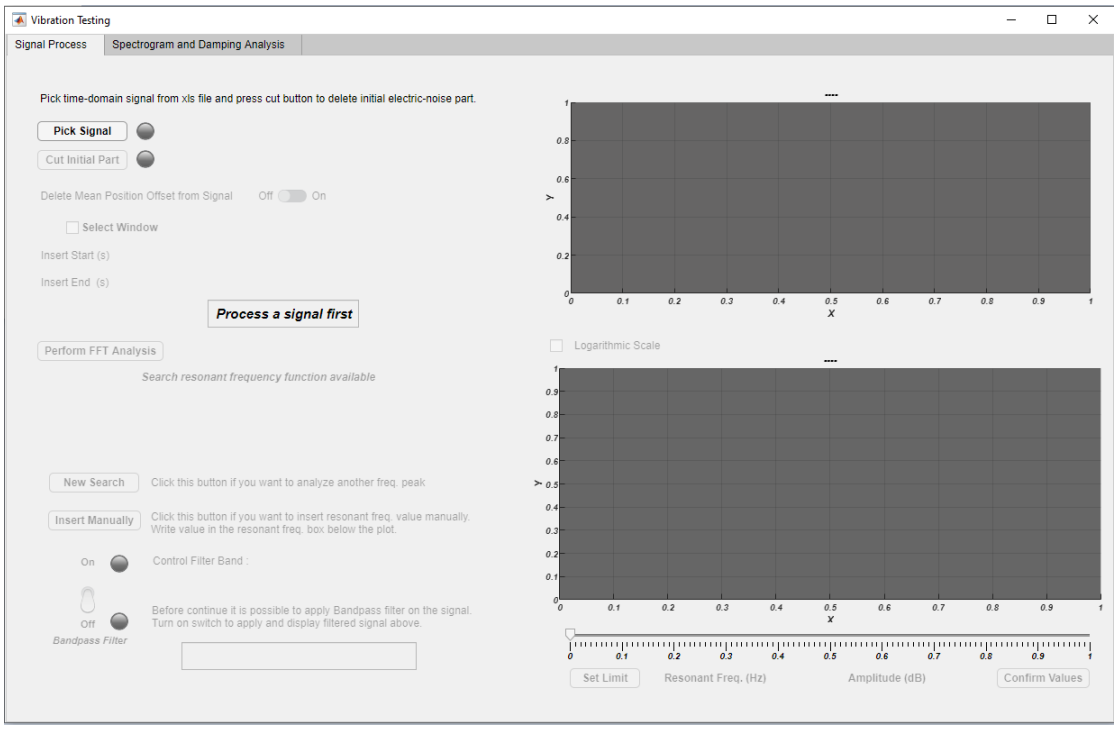

Figure 7.23: GUI: step 1

Table 7.3: Damping test results with different model, flaps and weights on SMC specimens.

Test Type	Modified Damping Model ζ	Viscous Model ζ
SMC Weight 1	0.002564	0.003294
SMC Weight 2	0.002585	0.003373
SMC Weight 3	0.002768	0.003916
SMC Flap 1	0.002474	0.004026
SMC Flap 2	0.002589	0.004453
SMC Flap 3	0.002632	0.004745

the previous FFT function and the resonance peaks searching function.

After completing this step, it is possible to move on to the tab. By pressing the button visible in Figure 7.27, the previous STFT function and amplitude peaks extracting function are launched.

The result of these operations is shown in Figure 7.28. It can be noticed, in blue color, the decay over time of the amplitudes.

Instead, the last step provides for the interpolation of the curve according to the damping model chosen from the drop-down menu. Finally, the results must be noted or saved (Figure 7.29).

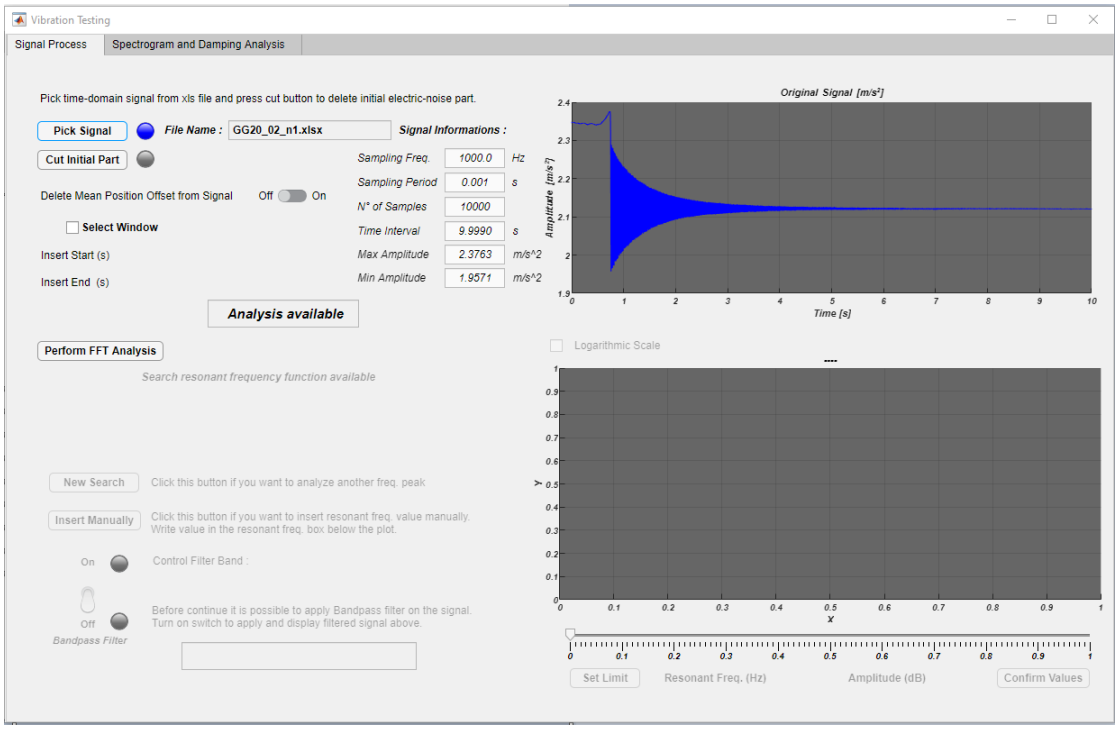

Figure 7.24: GUI: step 2

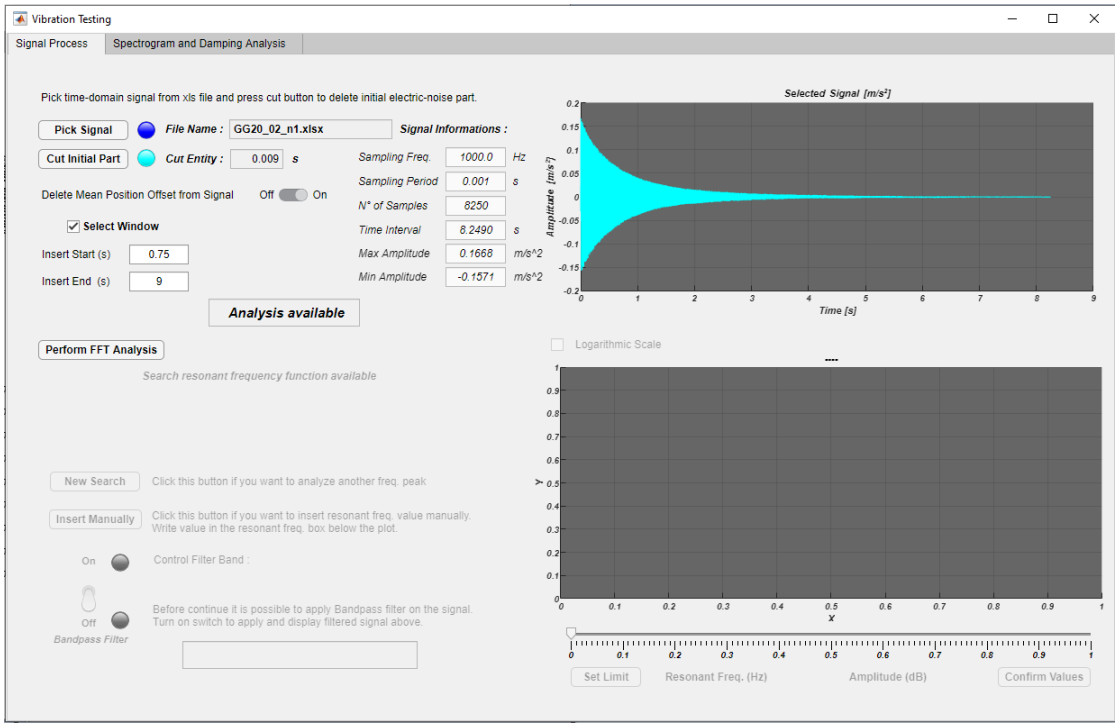

Figure 7.25: GUI: step 3

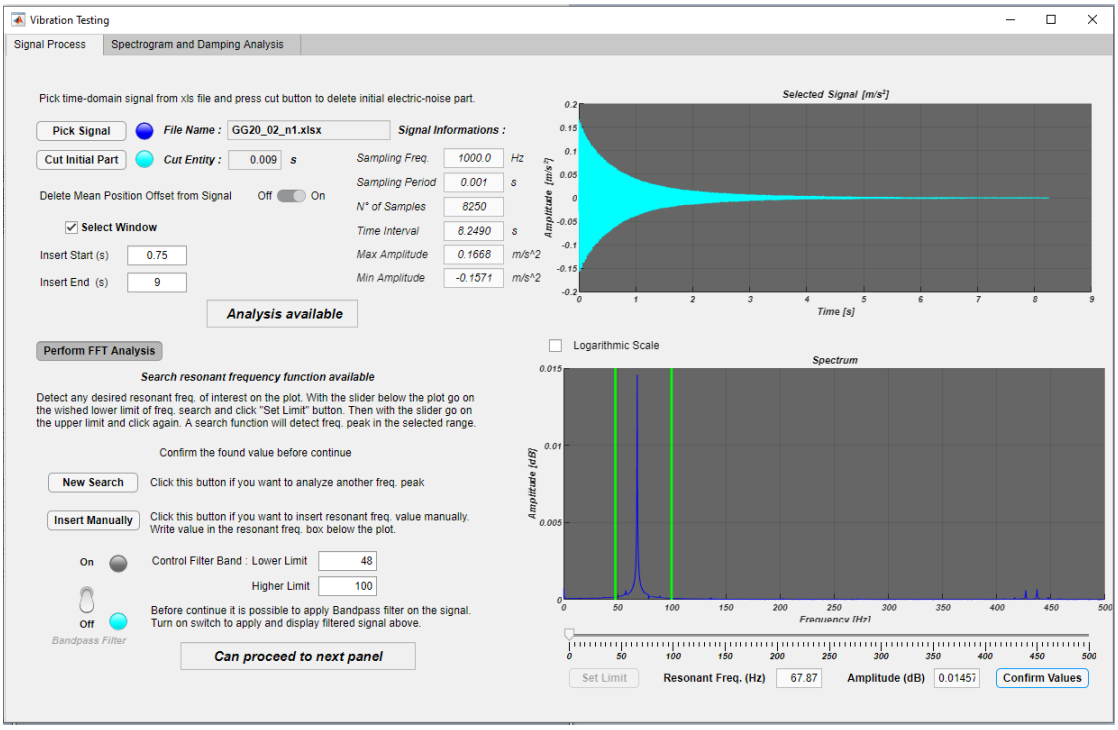

Figure 7.26: GUI: step 4

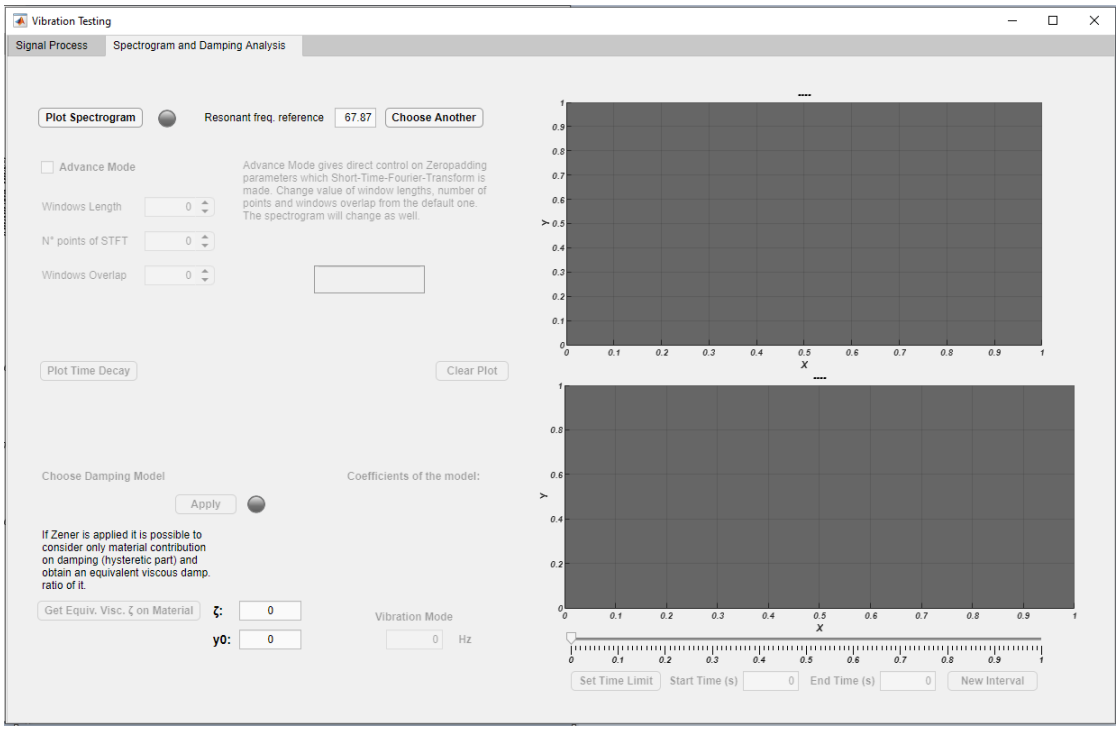

Figure 7.27: GUI: step 5

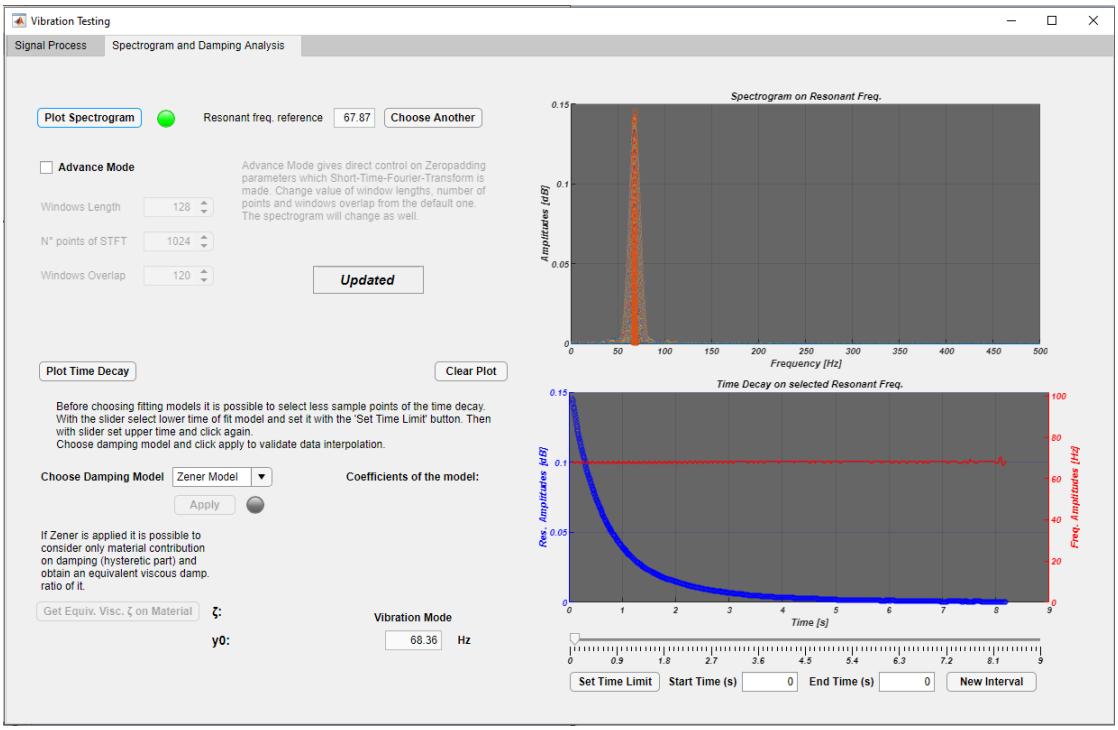

Figure 7.28: GUI: step 6

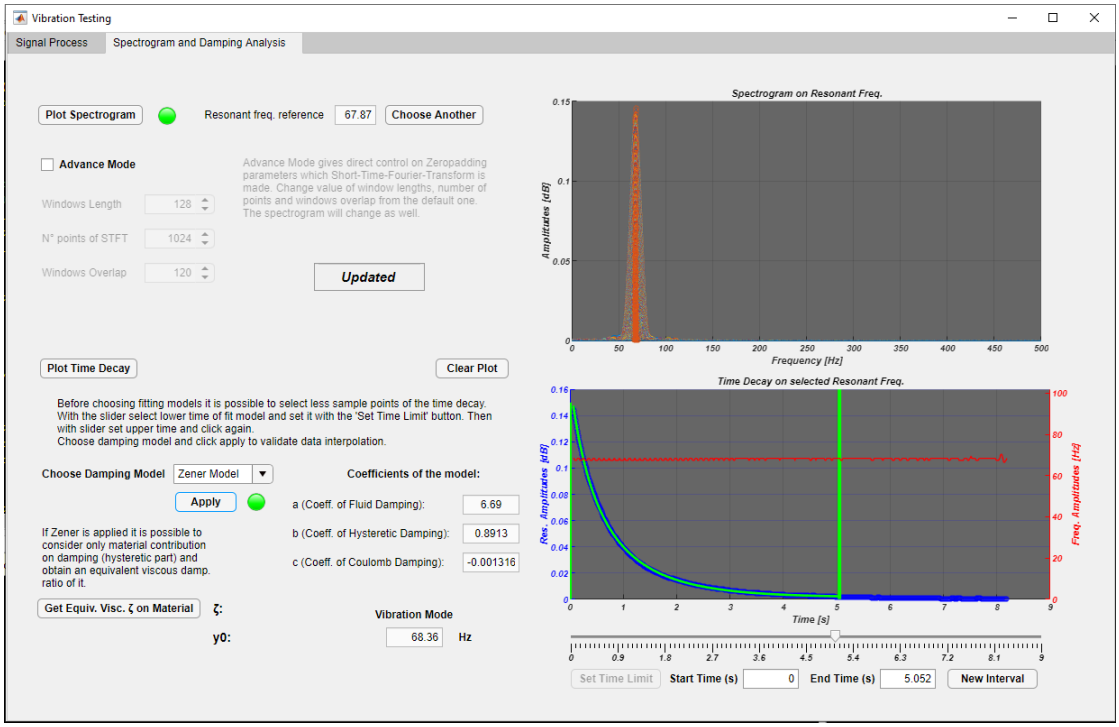

Figure 7.29: GUI: step 7

Chapter 8

Damping and mechanical behavior of rubbery nanofibrous-reinforced UD-CFRP

The following discussion derives from a joint research work conducted with the Ph.D. student Davide Cocchi. However, the long work carried out has involved more people than I want to thank. In particular, the Ph.D. student Emanuele Maccaferri, dr. Tommaso Brugo, Professor Laura Mazzocchetti, Professor Loris Giorgini and finally Professor Andrea Zucchelli. In this research, ready to be published, a new kind of structural composite was produced by interleaving random NBR/PCL (nitrile butadiene rubber / poly(*varepsilon*-caprolactone)) blend nanofibrous nonwoven mats into unidirectional Carbon Fiber Reinforced Plastic (CFRP) prepregs. Different specimen configurations were manufactured using different rubbery nano-reinforcement layers grammages. Mechanical properties were experimentally evaluated as a function of temperature using three-point bending (3PB) tests, while damping behaviour was evaluated by single cantilever beam vibration tests using the advanced Modified-Coulomb-Model (MCM). Moreover, Dynamic Mechanical Analyses (DMA) were performed to evaluate the impact of the rubbery nanofibrous layers on the overall thermomechanical properties of the modified laminates. The interleaved NBR/PCL nanofibrous mats improved the composite damping properties, with a significant influence on flexural strength and modulus only at high temperatures. Moreover, no significant impact on laminate weight and thickness, respect to reference samples without nano-reinforcement, were found. These results suggest that rubbery nano-reinforced unidirectional carbon fiber composite could be a good candidate for applications that need high energy dissipation, good specific stiffness, and specific strength without increasing the weight of the laminate. In particular hybrid metal-CFRP tubes with a viscoelastic interface layer, I developed in the first two years of Ph.D. program, could

be the first products will be designed with this methodology.

8.1 Introduction

Carbon fiber-reinforced composite materials have many advantages over traditional materials mainly because of their favorable specific stiffness, specific strength, and the capacity of dissipating energy. These characteristics make them suitable for high-performance applications like aerospace, automotive, industrial, sport, etc.

Traditional materials, like metals, have low damping capabilities resulting in high amplitude vibrations that can cause damages to structures [72]. Carbon fiber-reinforced composite materials, on the other hand, show good damping properties due to various factors that have not yet been fully explored in literature. At the micromechanical level, the energy dissipation is induced by different phenomena such as the viscoelasticity of the matrix, the damping of fibers and matrix, their interfaces, or by damages [73]. At the laminate level, instead, damping depends on the layer orientations, stacking sequence, and interlaminar effects [74, 75, 76]. Probably other phenomena could influence the damping behavior of composites, but to date, they have not been investigated.

Early work on the importance of damping in the theory of vibrations was conducted by Crandall [77] in which he studied damping as a method to control vibrations. In the 1970s, static and dynamic tests were conducted on Fiber Reinforced Plastic (FRP) composite materials. However, due to the high specific stiffness of FRPs, the standard analyses carried out to characterize polymeric materials, such as Dynamic Mechanical Analysis, are not reliable [78] since the sample reaches very high resonance frequencies that some machines are not able to reach. Subsequently, Adams and Bacon carried out a more detailed study on the damping capacities of the FRP composites [79]. In particular, they investigated the influence of the geometry and the orientation of the fibers on the performance of unidirectional laminates [80]. These studies presented analytical formulations that attempted to interpolate the tests carried out in the laboratory, which used an accelerometer to determine the natural frequencies of the tested specimen. However, the grips system and the weight of the accelerometer itself can influence the measurement. Therefore, Wright [81] developed a method in which the specimen was released and excited with sinusoidal vibrations, and an optical sensor detected its displacement. Using the logarithmic decrement method, he calculated the damping factor.

Adams et al. [82]used an energetic approach and electromagnetic waves to excite the specimen, calculating the Specific Damping Capacity (SDC). In this case, the weight of the coil was considered, which was comparable to the weight of the specimen and influenced its measurement. Furthermore, by the same authors, vacuum tests were performed as the air damping was not negligible in high

length and width specimens [79]. In the following years, other configurations were developed to improve the accuracy of the SDC measurement, such as the fixed beam or free-free configuration [83] in which the coils that excite the specimen were positioned differently. Other similar configurations used elastomeric foams to limit edge effects [84].

At the end of the 80s, Suarez [85] proposed two methods to determine the damping: the first using an electromagnetic exciter and a parasitic current probe, while the second involved the use of a suitable hammer to induce a pulse to the composite. The last method turned out to be very flexible, even in existing structures for determining defects in the composite, correlating them with an increase in damping [86].

In the following years, other authors like Maheri abandoned the classic accelerometers in favor of the LASER technology to identify the vibrations of the specimen due to an induced excitation [87].Subsequently, hybrid methods that exploit a theoretical/numerical approach for the calculation of damping were used [88]. While, other authors focused on the difference between material and structural damping [89] and on external factors that influence the measurement, providing advice on how to limit these effects [90].

In recent years, some authors have focused on maximizing damping by inserting viscoelastic layers between the FRP plies, providing useful information to optimize fiber orientation, type of gripping, excitation frequency, and stacking sequence [72, 91, 92]. While, others have studied the insertion of aramid fibers maintaining similar mechanical properties respect to pristine CFRP [93].The fiber type also influences the damping value of the composite. More recently, carbon fiber composites containing flax fibers hybridized with carbon nanotubes in an epoxy matrix showed an increase of up to 60 % in the loss factor due to the internal sliding friction between flax fibers [94].

Kevlar shows a greater damping power compared to glass and carbon fibers [74, 95]. Otherwise, flax fiber composites show good damping behaviors, but the mechanical properties of the composite quickly decay as the fiber content increases compared to carbon ones [75].

Regarding CFRP, composites with thermoplastic matrix have higher damping values, but, usually, the thermosetting polymers are to be preferred for structural applications as they are more rigid and show greater adhesion to the fiber [96], besides higher service temperature. As shown by Ni [97],the damping capacities of thermoplastic polymers increase parabolically with the matrix volume. In addition, epoxy resins are better than PEEK in terms of damping [95]. When the composite is excited by a force along the principal axis, the movement of the fibers into the viscoelastic matrix generates energy dissipation[98]. The more this movement is accentuated, the more the damping increases [99]. Detachments, de-

laminations, and generally, all damage phenomena are sources of energy dissipation and therefore increase the damping of the composite [100].

All the polymers used as a matrix in FRP composites show an increase in damping capacity when the temperature increases, while reducing their mechanical properties. In fact, at high temperatures, polymers soften, making their properties decay quickly [101]. It has also been noted that an increase in cross-linking times reduces damping capacities since more bonds are formed in the polymeric matrix, but the mechanical properties increase [102].

The damping capabilities of composite material are also influenced by the size and length of the fibers. Concerning short fibers, an increase in the damping coefficient is obtained when the shear stress along the fiber is maximum, as a function of the length/diameter shape ratio [103].Furthermore, the terminal areas of the short fibers are responsible for an increase in energy dissipation, due to the combination of high efforts and weak bonds [104]. In addition, the arrangement of the fibers in the matrix also influences the damping [105]. As for the fiber geometries, the work presented by Lei [106]compares the behavior of 5 different fabrics where the same matrix volume is maintained and showed that the woven structure has a strong effect on the fiber volume fraction, resin-rich area, and the warp architectures of the composites. Tests conducted with laminae with unidirectional fibers return different damping coefficients along with the different directions of the laminate plane [72]. These studies are not always in agreement on which is the optimal angle to maximize the damping, but they agree that it is necessary to maximize the shear effects. Generally, for unidirectional sheets, the maximum damping value is for angles of 35° in bending and 45° in torsion, while for angle-ply laminates, the maximum is between 40° - 50° both for bending and for torsion [80, 107, 108].

In addition to the direction of the fibers, the stacking sequence also plays an important role. Maheri [92] and Hwang [109, 110], analyzed the three-dimensional stress state to study its dependency. The lack of stiffness at the interface between laminae positioned at different angles leads to an increase in shear stress, both in-plane and out-of-plane.

A common solution to increase the damping capacities of composite materials is the use of bulk viscoelastic layers between FRP plies. Not all authors agree on the correct placement of the viscoelastic layers in the stacking sequence. Some authors place them near the center plane [111], while others in the outer layers [112]. From Berthrlot's works [113, 114] it can be noticed that by optimizing the orientation of the structural layers, the damping can be highly increased and that a single thicker layer of viscoelastic material is more efficient than two interspersed with a structural layer. Good results were obtained applying viscoelastic patches of different sizes and thicknesses on beams where the shear effect is greater

[115, 116]. The damping enhancement using viscoelastic layers appears to be an effective, constructively simple, and low-cost solution. However, their integration compromises the overall stiffness and integrity of the laminate besides causing an increase in its weight and size [117].

A novel method to increase the dynamic performance of composite laminates is to integrate nano-reinforcements into the matrix, like nanoparticles, carbon nanotubes, or nanofibers. It has been verified that carbon nanotubes offer a greater surface to volume ratio of interfacing than classic fibers, ensuring a higher creep resistance and, consequently, higher damping [78, 118, 94, 119, 120]. Polymeric nanofibers are also used for hindering delamination by increasing the interlaminar fracture toughness [121, 122].

Since the electrospun nanofibrous mats are made of thermoplastic polymers, mainly polyamides and poly(*varepsilon*-caprolactone) [123], these layers may well hindering composite delamination, but do not improve its damping properties [121]. On the contrary, rubber polymers may positively contribute to the damping enhancement, thanks to their viscoelastic nature [124]. Few attempts to producing rubbery nanofibers are reported in the literature due to difficulties in their production, arising from the rubber cold flow which leads to the formation of a compact bulk film. Usually, papers report just the proof of concepts of the possibility to electrospin rubber polymeric solutions [125, 126, 127, 128] or they attain microfibers rather than nanofibers [129, 130]. Often, the rubbery nanofibers need to be cross-linked for avoiding nanofiber coalescence. The rubber cold flow phenomenon may be so important that the cross-linking step has to be applied during electrospinning [131] or immediately after the process [129, 132] , thus strongly limiting the obtainable final membrane thickness. Recently, the production of rubbery nanofibers by single-needle electrospinning of polymeric blends made of nitrile butadiene rubber and poly(ε-caprolactone) (NBR/PCL) was reported by the Authors [121]. This method allows producing rubbery nanofibers with a high amount of NBR fraction without the need for a cross-linking step: the nanofibrous morphology is stable at room temperature, and there are no restrictions to the obtainable mat thickness. The same rubbery nanofibrous mats were successfully interleaved in CFRP epoxy laminates [121], resulting in the first reported work of composite laminates rubbery nano-modification. The rubbery nanofibers greatly increase the energy release rate in Mode I (up to +480%), and they may strongly influence the overall composite thermomechanical properties.

In this work, a new kind of structural composite was prepared by interleaving NBR/PCL blend nanofiber layers in unidirectional CFRP laminates. Mechanical properties were experimentally evaluated as a function of temperature using 3PB tests. Damping behaviour was evaluated by single cantilever beam vibration tests. To perform an accurate measurement of damping and separating the damping

contribution of the air and the joint from the contribution of the material, the advanced Modified-Coulomb-Model (MCM) was adopted [133, 134, 135]. Moreover, DMA were performed to evaluate the impact of the rubbery nanofibrous layers on the overall thermomechanical properties of the modified laminates. The interleaved NBR/PCL nanofibrous mats improved the composite damping properties, with a negligible influence on flexural strength and modulus. Moreover, no significant impact on laminate weight and thickness, respect to reference samples without nano-reinforcement, were found.

8.2 Materials and Methods

8.2.1 Materials

Carboxylated nitrile butadiene rubber (NBR) NIPOL 1072CGX was purchased from Zeon Chemicals [68 %mol butadiene (Bu), 28 %mol acrylonitrile (ACN), 4 %mol methacrylic acid (MAA)]. Poly(*varepsilon*-caprolactone) (PCL), Mw 70,000-90,000, was purchased from Sigma-Aldrich. Polymers were both used without any preliminary treatment. N,N-dimethylacetamide (DMAc), N,N-dimethylformamide (DMF) and chloroform (CHCl3) were purchased from Sigma-Aldrich and used without further purifications. To prepare the rubbery NBR/PCL nanofibrous layers with 60 %wt of NBR (named n-60/40), the same method and the same electrospinning parameters proposed by the Authors in a previous work were adopted [121]. To achieve different nanofiber thicknesses/grammages, only the electrospinning time has been changed. The carbon fiber epoxy unidirectional prepreg was T700S-24K/DT210 epoxy-based resin provided by Deltapreg (Toray group, Italy), with Vf = 53% and 350 g/m2 of carbon fibers. To assess the thickness of the nanofibrous layers, a digital comparator (Alpa MegaRod) was used. To calculate the mat grammage (i.e. the mat weight per square meter), the nanofibrous layers were weighted by a scale with a resolution of 0.01 mg (Radwag AS 60/220.R2). Nanofibers images, reported in Figure 8.1, were acquired through a Scanning Electron Microscope (SEM, Phenom ProX) to evaluate both their morphology and mean diameter (268 ± 43 nm).

8.2.2 Sample preparation

The samples for mechanical (3PB), thermomechanical (DMA), and dynamic (damping) tests were obtained from plates manufactured using vacuum bag technology. All the specimen configurations were produced using 7 prepreg layers, resulting in a total laminate thickness of 2.6 mm. Nanofibrous mats of different thicknesses were manually interleaved at the interface of the CFRP layers during the lamina-

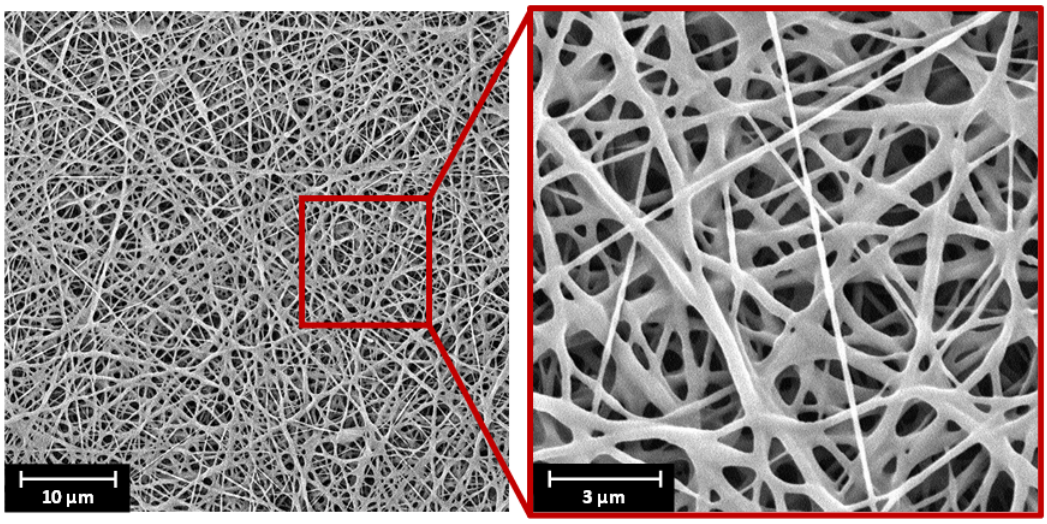

Figure 8.1: Rubbery nanofibers morphology at 5,000x magnification and (B) 20,000x magnification.

Table 8.1: Specimen configurations.

Configuration	MAT thickness (μm)	MAT grammage (g/m^2)
ref.	-	-
int. 5	5	2.5
int. 10	10	5.1
int. 20	20	9.6

tion process. Four laminate configurations, reported in Table 8.1, were made. A reference configuration i) composed only of 7 CFRP plies without interleaved layers (ref.) and other three nano-structured ones with ii) 5 μm iii) 10 μm, and (iv) 20 μm thick nanofibrous layers interleaved at each interface (named int. 5, int. 10, and int. 20, respectively) were produced. Each sample was therefore composed of 7 plies and 6 possible interfaces. The geometries of the 3PB specimens and of the damping test ones were defined according to ASTM D7264 and ASTM E756-05, respectively, as well as DMA specimens as per ISO 6721-1 (Table 8.2).

8.2.3 Thermomechanical, mechanical, and damping tests

Overall thermomechanical properties of CFRPs were evaluated via DMA, using a Netzsch DMA 242 E Artemis instrument in a three-point bending configuration with a fixed span of 40 mm. DMA analyses were carried out in temperature ramp, in the 0–170 ℃ range at 3 ℃/min heating rate, 1 Hz frequency, amplitude 20

Table 8.2: Specimen geometries.

Test	length (mm)	Width (mm)	Thickness (mm)
3PB	110	15	2.6
Damping	280	25	2.6
DMA	50	7.5	2.6

µm, static force / dynamic force ratio = 1.5. For each laminate configuration 3 specimens were tested.

Flexural tests were carried out to assess the effect of the nanofibrous rubbery membranes on the mechanical properties of the different laminate configurations. Two different types of flexural tests under different conditions were performed: i) the classic one, carried up to failure, to evaluate the elastic modulus and the flexural strength at three different temperatures (20, 50, and 80 ℃) and ii) a cyclic loading-unloading test performed in the elastic regime at a frequency of 1 Hz to evaluate the elastic modulus degradation as a function of the temperature.

Regarding type i) 3PB test, the temperatures were chosen because 20 ℃ is the reference RT, 50 ℃ because it is slightly lower than the melting of the PCL crystalline fraction of the rubbery blend, and 80 ℃ because it is enough above the PCL melting temperature.

Regarding type ii) 3PB test, despite similar to the DMA one, it allowed a more precise assessment of the flexural modulus as a function of the temperature. In fact, since UD CFRP laminates exhibit a very high flexural stiffness, the evaluation of storage modulus (E') by the DMA may be not accurate.

3PB tests were performed on Instron Model 8033 equipped with a climatic chamber using a 2 kN load cell and at a crosshead speed of 2 mm/min. A total of 12 3PB specimens were manufactured for each laminate configuration.

The dynamic tests for damping evaluation were performed with a laser sensor optoNCD 1402 and a four-channel control unit NI-9215 (National Instruments) in a fixed-free beam setup as shown in Figure 8.2 and according to ASTM E756-05. The specimens were excited by a step signal. For each laminate configuration, 2 specimens were produced and for each one 5 repetitions were made. The setup parameters, depicted in Figure 8.2, were L = 255 mm, d = 105 mm, C = 25 Nm, a = 5 mm.

The analog signal, acquired at 2,000 Hz by the laser, was converted into digital one by NI-9215 and processed by the MATLAB 2019Rb software. First, the signal was cut with a 10 s time window (Figure 8.3A). Subsequently, a Fast Fourier Transform (FFT) was performed to determine the first bending resonance frequency of the samples (Figure 8.3B).

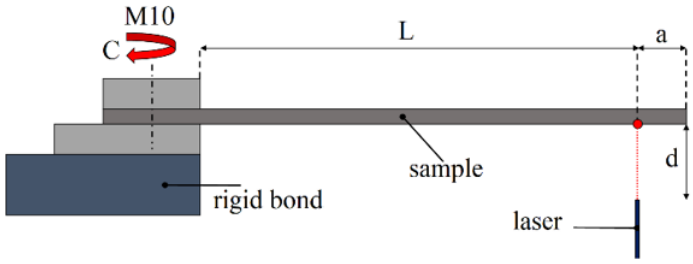

Figure 8.2: Damping test setup scheme.

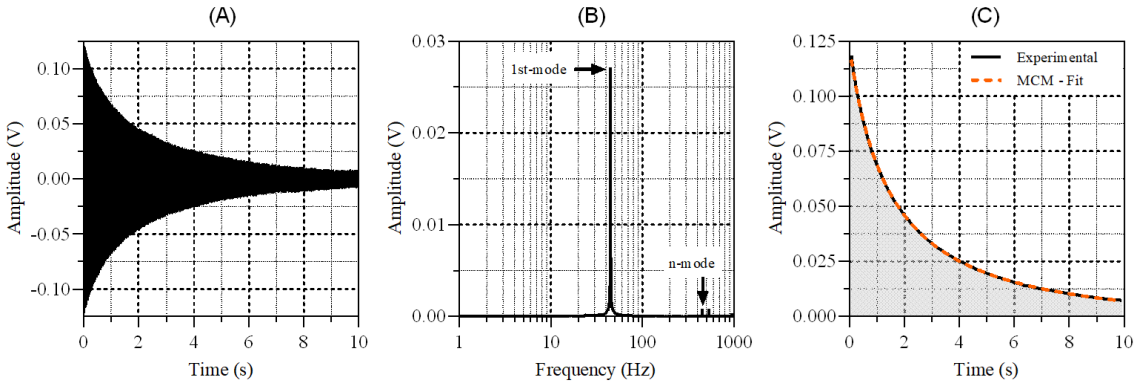

Figure 8.3: (A) Original signal acquired by laser sensor; (B) Fast Fourier Transform of the signal; (C) Experimental amplitude decay as a function of time and MCM-fit.

Therefore, the MATLAB spectrogram function was used on the entire signal by entering the previously found natural frequency. In this way, it was possible to find the amplitude decay curve in the time domain. After, a fitting algorithm based on the MCM was applied (Figure 8.3C). To have the most accurate damping measurement, the material damping contribution was separated from the air and the joint ones.

8.3 Results

An overview of the thermomechanical properties of the different laminate configurations was evaluated via DMA (Figure 8.4). The laminates int. 5 and int. 10 show an E' behaviour similar to the reference one. The conservative modulus is comparable to the one displayed by the unmodified CFRP, while the E' onset slightly lowers (107 ℃ vs 113 ℃ for the ref.). By contrast, int. 20 shows a first E' onset at 55 ℃ , and a main ℃ drop characterized by an onset at 99 ℃ . The behaviour of the last sample is similar to what evidenced by a previous study.

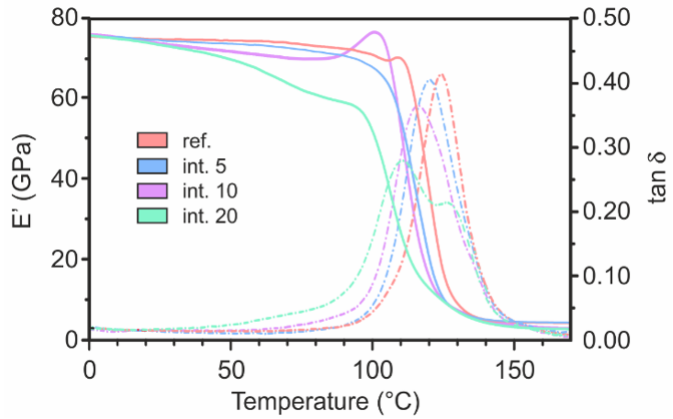

Figure 8.4: DMA analyses for the different laminate configurations.

Regarding the tan*delta*, the peaks do not show relevant shifts for increasing grammage of interleaved mats, except for int. 20 configuration (main peak at 111 ℃ vs 124 ℃ for the ref. one). Besides, the shape of the curve is different, displaying two peaks. The first peak accounts for the toughened epoxy resin thanks to the NBR/PCL mixing, while the second one, at 128 ℃, is probably due to the unmodified resin fraction. It is to underline that in almost all the modified laminates, the presence of the NBR/PCL blend widens the window dissipation energy of the composite to lower temperature, indicating a potentially damping enhancement also at room temperature. From the destructive 3PB analyses, it was found that the elastic modulus and flexural strength of the different specimen configurations do not show a significant difference at RT. As reported in Figure 8.5, with increasing temperature, the effect of the nanomat becomes more noticeable, especially for higher mat grammages. Indeed, at 80 ℃ the int. 20 configuration shows a reduction of 13 % in elastic modulus and 20 % in flexural strength compared to the ref. configuration. These results are in good accordance with the overall performance of E' identified by the DMA test.

Figure 8.6 shows the flexural modulus as a function of temperature for the different specimen configurations, obtained by 3PB cyclic loading-unloading tests. As can be noticed, the elastic modulus shows a significant reduction only when high temperatures (above 80 ℃) and high grammages (5 $g/m2$, int. 10) are combined. However, during the life-cycle of common composite components, these high temperatures are almost never reached, except for special applications. This phenomenon is probably due both to the small amount of interspersed nanofibrous membranes and to the curing cycle, that partially melt the nanofibers allowing the NBR/PCL blend mixing with the epoxy resin. Although the qualitative trends of E' and flexural modulus are similar, the numerical values shown in Figure 8.6 are much more accurate than those obtained from the DMA analysis. In fact,

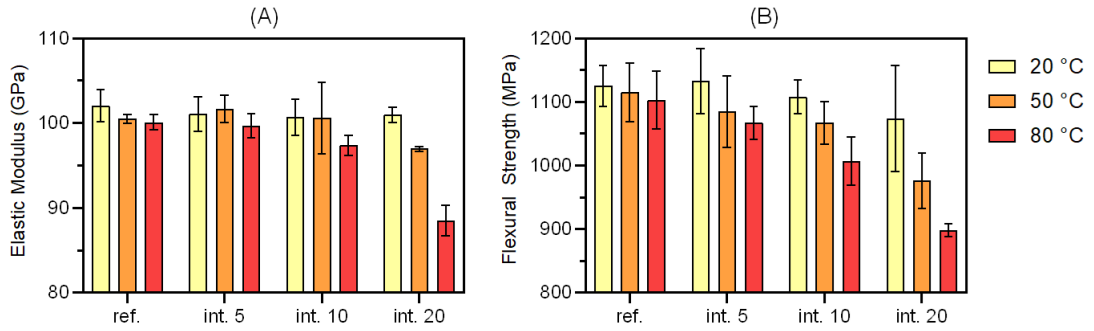

Figure 8.5: (A) Flexural elastic modulus and (B) flexural strength for different specimen configurations and temperatures.

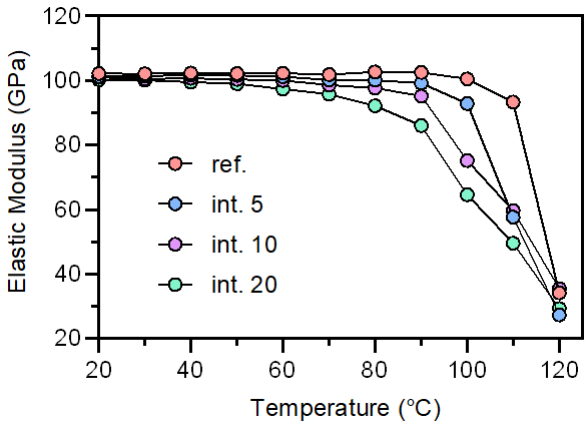

Figure 8.6: Flexural modulus dependence on temperature for the different specimen configuration.

DMA analysis is strongly influenced by the specimen specific loading region and the reduced length span. On the contrary, in the 3PB test, since the imposed deformation is macroscopic, the local effects become negligible because the stressed volume is increased.

Regarding damping tests, the fitting of the experimental signal with MCM has always guaranteed a R2 over 0.99. It was therefore possible to calculate the normalized material damping value for each configuration by excluding the contribution of both the air and the joint. This method was adopted because the damping impact of the air is predominant compared to the material one, while the influence of the joint is negligible. As shown in Figure 8.7A, the material damping factor ranges from 1.75 E-3 to 3.10 E-3 for the ref. and int. 20 configurations, respectively. Figure 8.7B shows the increase in material damping factor versus the laminate weight variation due to the rubbery nanofibrous mats integration. By

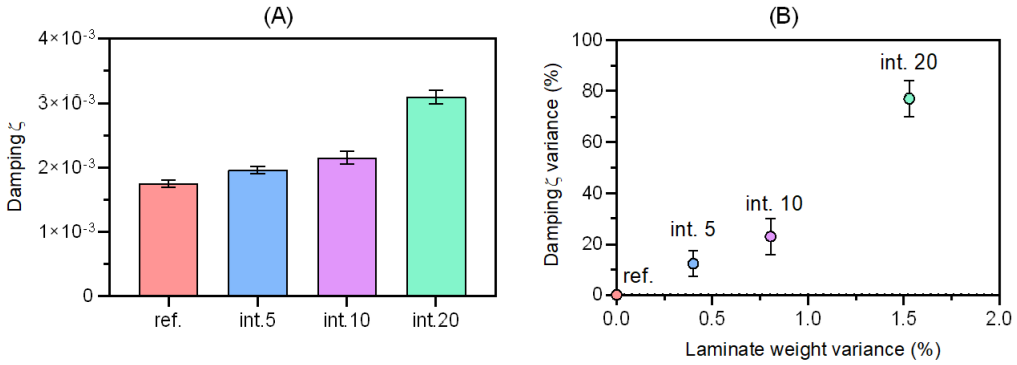

Figure 8.7: (A) Material damping values for the different specimen configurations and (B) material damping percentage variance as a function of the laminate percentage weight variance.

comparing the obtained results, it is interesting to note that as the grammage of the nanofibrous membranes increases an exponential trend of the material damping is observed. The major damping enhancement was obtained with the int. 20 configuration, which shows a material damping factor improvement of 77 % for a laminate weight increment of only 1.5 %.

8.4 Conclusion

In this part of the thesis, a new kind of structural composite was prepared by interleaving rubbery NBR/PCL nanofibers layers between unidirectional CFRP prepreg laminates. Mechanical properties were experimentally evaluated as a function of temperature using 3PB tests. Damping behaviour was evaluated by single cantilever beam vibration tests and, thanks to the advanced Modified-Coulomb-Model, an accurate measurement of the material damping was obtained excluding the contribution made by the air and joint. In addition, DMA was performed to evaluate the impact of the rubbery nanofibrous layers on the overall thermomechanical properties of the modified laminates. Flexural tests show no significant differences at room temperature in elastic modulus and flexural strength between reference and modified specimen configurations. With increasing temperature, the effect of the nanomat becomes more noticeable, especially for higher mat grammages. Flexural modulus shows a significant reduction only for temperatures over 80 ℃ . These results are in good accordance with the overall performance of E' identified by the DMA. The interleaved NBR/PCL nanofibrous mats greatly improved the composite damping properties with a maximum increase of 77 % in the composite loss factor, with a negligible influence on flexural strength and modu-

lus. No significant impact on laminate weight and thickness, respect to reference samples without nano-reinforcement, were found. This new kind of nano-modified composite material is suitable for all those applications that require high energy dissipation ensuring at the same time high mechanical performance even at intermediate in-service temperature. The integration of nanofibrous rubbery membranes interspersed between the composite layers overcome the limits related to the use of bulk viscoelastic layers, which could negatively affect the laminate weight and integrity, even increasing its fracture toughness. This novel technique may allow engineers to design advanced composite components with high damping capacity by ultra-low grammage rubbery nanofibrous layers addition. One parameter that has not been analyzed but which is worthy of investigation is the interlaminar fracture toughness. This parameter identifies the shear strength of a composite and is very important in composite structural engineering. It will be investigated in the near future.

Part III

Hybrid tubes

Chapter 9

Hybrid tubes

The following discussion concerns a topic on which I have published, to date, scientific papers in international journals [3, 5, 6, 9]. Therefore, I have tried to summarize my works in this Part (III) and expose them clearly without going too far and omitting superfluous details.

9.1 Introduction

It is desirable to achieve high critical speed when designing rollers and tubes for printing, converting industry, and other industrial sectors. Full CFRP tubes can guarantee higher natural frequencies with respect to their metal counterparts due to their higher specific modulus (E/ρ). However, they are traditionally associated with poor and difficult machinability, which is necessary to guarantee the strict geometrical tolerance requirements. Moreover, the coating applications, which are often required in converting industries, are generally not feasible on CFRP compared to a metal surface. The coupling of an outer metal tube and an internal CFRP tube has been identified as a new design and manufacturing pathway to develop hybrid tubes that can combine good dynamic performances with good machinability and feasible coating applications. Many authors in recent years have verified that hybrid tubes also possess excellent compressive strength, impact resistance, and energy absorption capabilities [136, 137, 138, 139, 140, 141, 142, 143, 144, 145].

Hybrid tubes have been successfully manufactured using different methods and technologies, each one with their specific limitations. The adhesive bonding of two originally separate tubes is a common technique. Still, it can be applied only for short-length components and requires a two-step manufacturing process [146, 147, 148, 149, 150, 151]. Thermal interference coupling is usually obtained by heating or cooling the metal component. Still, it is a time-consuming method

that slows down the entire production process. Again, two manufacturing steps are required, and only short-length components can be produced.

A novel and promising technology is the co-curing of the CFRP with an external metal tube. This technology allows for the production of hybrid components in one manufacturing step, thus yielding cost and time savings. However, despite their attractive advantages, the manufacturing tasks associated with hybrid metal-composite co-cured tubes are still a challenge with their design process. Additionally, few recent studies have been published to date.

A manufacturing process of co-cured hybrid aluminum-core shaft was studied by Cho and others [152, 153, 154]. Their investigation showed that the final quality of the component is strictly connected with the axial residual thermal stresses due to the massive difference in the coefficient of thermal expansion (CTE) of the two materials. A compressive preload, by use of a steel jig, was introduced during the entire curing phase to reduce the residual thermal stresses. This limits of this methodology include the complexity of the whole process and the ability to compensate for the axial stress only, thus neglecting the triaxial stress effects against failure.

Lee and others [155] suggested an initial solution for designing and manufacturing co-cured hybrid aluminum driveshafts with an external metal and composite applied inside. Again, the effects of the thermal axial stresses were reduced by inducing a compressive preload on the outer metal tube. The stacking sequence of CFRP layers was designed to minimize the failure index according to Tsai-Wu criterion [47]. This study focuses mainly on the stresses along the tube subjected to torque, without studying residual stresses.

Another solution for the design and manufacturing of hybrid co-cured components was proposed by Han [156] and others. They created a hybrid pantograph upper arm using a PTFE (Polytetrafluoroethylene) layer between two conical tubes made by metal and composite laminate, respectively. This solution was adopted to prevent residual thermal stresses and possible failure due to the decoupling of the two tubes. The resulting component demonstrated the possibility of reducing the overall arm mass and enhancing the structural stiffness with respect to conventional metal solutions. Moreover, the PTFE interlayer has proven effectiveness in avoiding the failure of the CFRP. Nevertheless, based on the decoupling of two tubes, such a solution is non-recommended for high-speed rotational systems because it could manifest criticality in balancing and mutual sliding of CFRP and with a consequent onset of wear phenomena on the CFRP.

Finally, I presented works [3, 6], where a viscoelastic material was introduced in the metal-CFRP interface to produce the hybrid tube in one step. This solution avoided the problems related to the residual stresses which develop during the curing process.

9.1.1 Co-curing technique

The previous co-curing techniques were implemented using autoclave or ovens, and it was found that they are not efficient from the energetic, cost, and time consumption point of view. The main reason is that those methods have an extended curing cycle, need massive capital investment, and much space. Besides, the autoclave needs to be cooled after curing.

Therefore, several curing methods and processes have been studied and implemented over the last decade but are not discussed in detail in this work. One of these curing methods is resistance heating. This method exploits the Joule heating effect that involves a material with an electric current applied. The previous studies involving Joule heating were focused on using carbon fibers as heating elements by directly applying electricity to them[157, 158, 159]. However, this method presents great difficulties in industrial applications, since each bundle of fibers must be insulated and fed individually. Another similar technique was provided by Asanuma et al. [160], which made a hybrid aluminum/CFRP plate by applying electrodes directly on CFRP but with an insulator to avoid lowering the resistance of the plate.

Another technique for electrical resistance curing is the addition of nanomaterials to the matrix. Mas et al. [161] directly cured epoxy resins through the Joule effect by adding carbon nanotubes (CNTs) and graphene to the matrix. Nguyen et al. [162] successfully cured hybrid carbon fiber prepreg with current applied on layers of nanotubes in an out-of-autoclave (OOA) process.

Several other works [163, 164, 165, 166] investigated the curing of composite materials with the use of different embedded resistive heating elements, which is a similar approach to the one proposed in the present work.

However, in the field of hybrid metal-CFRP tubes, the current can be applied directly on the metal tube using it as a resistive heating element, resulting in great time and costs saving. Due to the thermal conductivity of metal and CFRP, a high thickness tube can be cured. The flexibility of the entire process suggests that other geometries could also be taken into consideration. To date, I have published a paper dealing with this method [9].

The main problem with this technique is the low resistance of the metal. Still, with a relatively large transformer (i_1 amps 75 to i_2 2500 amps), the Joule effect can cure various tube formats for printing and converting industrial sector.

9.1.2 Achievements

This thesis presents a detailed analysis of a hybrid tube obtained by a single-step curing process. I discuss the effect of rubber-like material at the metal-CFRP interface and compare its impact with the case of an epoxy layer as interface ma-

Table 9.1: Test tubes Configurations.

ID	Interface type	$D_{e,AL}$ (mm)	$D_{i,AL}$ (mm)	$D_{e,CFRP}$ (mm)	$D_{i,CFRP}$ (mm)	l (mm)
Epoxy-Config	EP210	75	70	69.6	65.2	900
Rubber-Like-Config	Kraibon HAA	75	70	69.0	64.6	900

terial. In particular, an experimental and numerical study of the stress distribution at the free edges of hybrid tube is presented. Besides, the influence of length, total tube radius, and thickness on residual thermal stress peaks have been numerically evaluated. As a conclusion of the topic, I present and discuss the effect of the characteristics of rubber-like material on the hybrid tube design.

This thesis also presents a methodology for co-curing hybrid metal-CFRP tubes in an out-of-autoclave (OOA) technology. Besides, an analytical model, based on Joule effect, is proposed and verified by experimental tests and FEA.

9.2 Materials and Method

9.2.1 Geometry

For the experimental study, and for the first numerical analysis, one geometry for the hybrid tube, in terms of total tube radius and length, has been chosen. Two interface materials have been investigated, an epoxy layer and a rubber-like layer, as reported in Table 9.1 and Figure 9.3a. The difference in thickness of the interlayer was dictated by process and industrial requirements.

It is worth mentioning that the chosen geometry, in terms of external diameter and length of the tube, is one of the most commonly adopted in the converting and printing automatic machines. Moreover, the other geometrical parameters, such as the thickness of the metal and CFRP tubes, were chosen to have a theoretical increment of the first natural frequency by 30% compared to a standard full aluminum tube, which has a first natural frequency of 250 Hz, measured in a pinned-pinned configuration constraint (570 Hz in free-free condition), according to [167].

9.2.2 Materials

The external metal tube was a commercially extruded aluminum alloy 6082-T6. The carbon fiber epoxy prepreg was M23350R manufactured by Reglass Srl (Italy), whose properties are similar to T300/5208. The mechanical properties of the carbon fiber epoxy prepreg are reported in Table 9.3.

Table 9.2: Material properties.

	λ $(\frac{W}{mK})$	C_p $(\frac{J}{kgK})$	ρ (kg/m^3)	th (mm)
Al 6082-T6	160	875	2770	2.50
Interface	0.20	220	1250	0.50
CFRP	0.20	120	1490	4.75
Silicone	0.20	702	2330	5.00

The epoxy interface material was a film of EP210, with an average thickness of 0.2 mm, supplied by Reglass Srl. The rubber-like interface film was Kraibon HAA9275/45, with an average thickness of 0.5 mm, provided by KRAIBURG TPE GmbH & Co. KG (Waldkraiburg, Germany). Reglass Srl provides the mechanical properties of the epoxy resin EP210. The properties of the rubber-like interface materials are provided by KRAIBURG TPE Gmbh and acquired with tensile tests according to DIN 54504. The mechanical properties of aluminum alloy 6082-T6 are provided by The Aluminum Association, Inc. from Aluminum Standards and Data 2000 and International Alloy Designations and Chemical Composition Limits for Wrought Aluminum and Wrought Aluminum Alloys (Revised 2001). All materials properties are listed in Table 9.3 and Table 9.4.

The material properties, reported in Table 9.2, were measured by the manufacturers according to regulations, excluding the properties of the silicone, which are similar to those present in Ansys Data libraries[168].

The thermocouple logger was an MTM-380SD supplied by Lutron Electronic, and an optical microscope and a DSC20 Mattler machine were used to evaluate the final post-cure quality of the product.

The custom electrical resistance curing machine was designed by Reglass Srl (Italy) and is composed of a mono-phase transformer (i_1: $75A$, V_1: $0-400$, i_2: $2500A$, V_2: $0-12$) coupled with a thermocouple feedback control system (Figure 9.1 and Figure 9.2).

9.2.3 Manufacturing Process

The manufacturing process, depicted in Figure 9.3b, is an evolution of the one presented by Povolo et al. [3] to produce hybrid tubes and can be summarized in 6 steps:

1. A cylindrical mandrel is prepared and cleaned with methylethylketone and coated with a releasing agent.

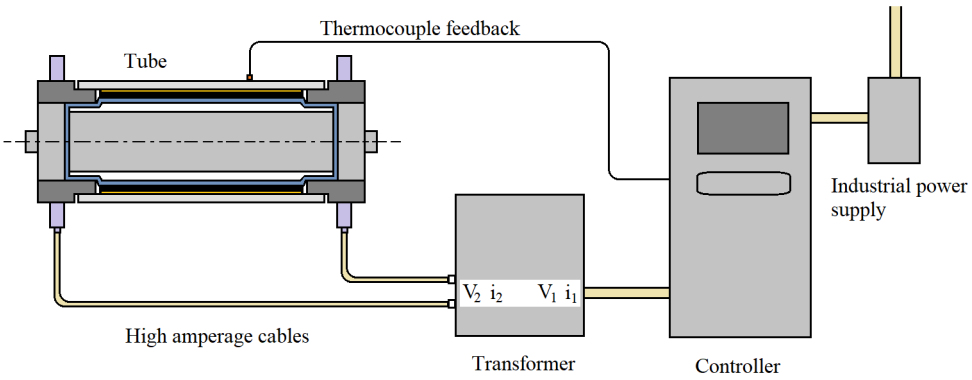

Figure 9.1: Electrical curing system scheme.

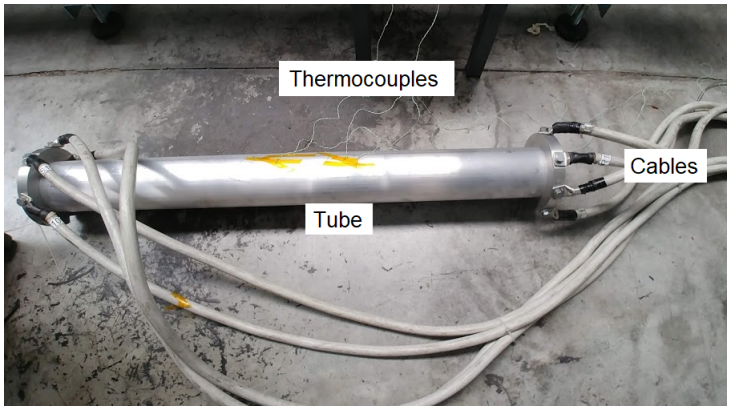

Figure 9.2: Electrical curing system setup.

Table 9.3: Prepreg properties.

Properties		UD Carbon fiber epoxy prepreg
ρ	(kg/m^3)	1480
E_1	(MPa)	121000
E_2, E_3	(MPa)	8600
G_{12}, G_{13}	(MPa)	4700
G_{23}	(MPa)	3100
ν_{12}, ν_{13}		0.27
ν_{23}		0.40
α_1	(1/℃)	-2.7 $\times$ 10^{-7}
α_2, α_3	(1/℃)	4.1 $\times$ 10^{-5}
S_1^t	(MPa)	2000
S_1^c	(MPa)	-1200
S_2^t, S_3^t	(MPa)	30
S_2^c, S_3^c	(MPa)	-100
S_{12}, S_{13}	(MPa)	60
S_{23}	(MPa)	30

ρ: density, E_1: longitudinal elastic modulus; E_2, E_3: transverse elastic modulus; G_{12}, G_{13}, G_{23}: shear modulus; ν_{12}, ν_{13}, ν_{23}: poisson's ratio; α_1, α_2, α_3: directional CTEs; S_1^t, S_2^t, S_3^t: tensile strength; S_1^c, S_2^c, S_3^c: compressive strength; S_{12}, S_{13}, S_{23}: shear strength.

2. Prepreg layers are stacked with a suitable overlap on the surface of the mandrel, and the interface layers are applied to the last layer of UD.

3. The mandrel is inserted into the metal tube together with metal bushings to ensure the co-axiality of component.

4. The pneumatic system is gradually increased to a pressure of 4 bar to expand the elastic surface of the mandrel. The prepreg and the interface layer are thus forced to adhere to the metal tube inner side. In this condition, the curing phase of the entire component can take place with the electrical custom system.

5. Once the curing cycle is over, the pressure is released, and the mold is extracted and cleaned.

6. The component is machined and finished.

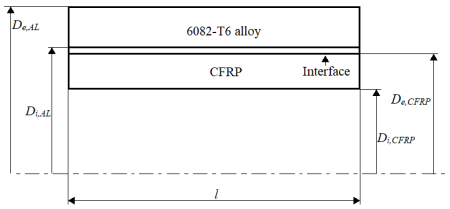

(a) Geometry scheme.

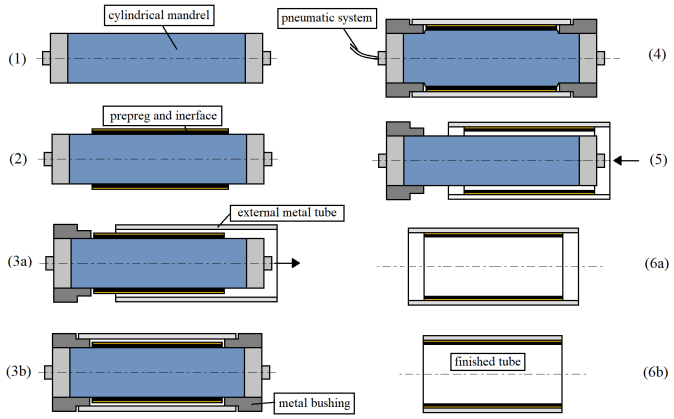

(b) Povolo [3] process.

Figure 9.3: Tube geometry diagram and novel manufacturing process diagram.

Table 9.4: Aluminum, Rubber-Like (Kraibon) and Epoxy Resin properties.

	E (MPa)	G (MPa)	ρ (kg/m^3)	α (1/℃)	S_y^t (MPa)
6082-T6 alloy	70000	26000	2700	2.4×10^{-5}	250
Kraibon HAA9275/45	275*	92*	1250	-	7.4*
Epoxy EP210	2200	810	1160	6.0×10^{-5}	40.0

*Tested according to DIN 53504; S_y^t: yield strength.

9.2.4 Numerical Model

Stress and Strain Analysis

Finite element analysis (FEA) was performed to study residual stress distribution at the free edges, the influence of interface layer material, and the geometrical parameters (length, diameters, thickness). The cooling phase was simulated into a commercial FEM software ANSYS Workbench through a static structural analysis with an implicit solver. A unitary radiant slice of a half-cylinder was modeled, and proper boundary conditions were applied to reduce the computational time. This assumption was following the axial symmetry of the geometry and load conditions, as represented in Figure 9.4.

Solid 186 elements (a high order, 3-D, 20 nodes solid element), which exhibits quadratic displacement formulation, were used. Full-solid, layer-by-layer modeling has been adopted to evaluate the out-of-plane stresses. A reduced integration formulation was set to minimize locking phenomena. A bilinear isotropic hardening material model was used to simulate the rubber-like layer, as shown in Figure 9.5 by the continuous line, while the dotted line represents the results of the tensile test provided by KRAIBURG TPE Gmbh according to DIN 53504

The cooling ramp of the curing cycle was modeled by a uniform thermal load from 110℃ to 20℃. A mesh convergence test was performed with respect to the zero-stress condition for τ_{rz} at the free-edges. The mesh was refined at the free edge, and a value of 0.02 mm was found to be a fair compromise between accuracy and computational time.

Thermal curing analysis

The first model and simulation were made to verify the air convection coefficient experimentally, determined, and adopted in the analytical model for a simple aluminum tube subjected to heating and cooling.

Instead, the second model concerns a complete hybrid tube during the curing heating phase with the resistance heating method. The simulations were performed

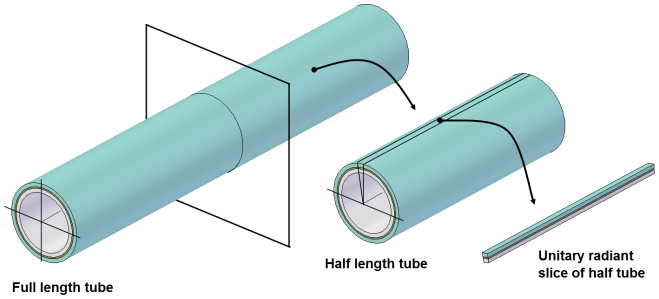

(a) Full and simplified geometrical model.

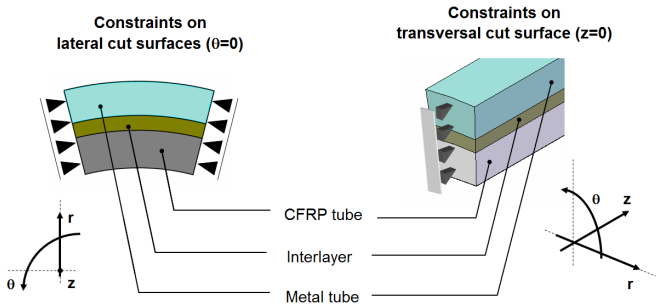

(b) Constraints condition on the simplified geometrical model

Figure 9.4: FEM model representation.

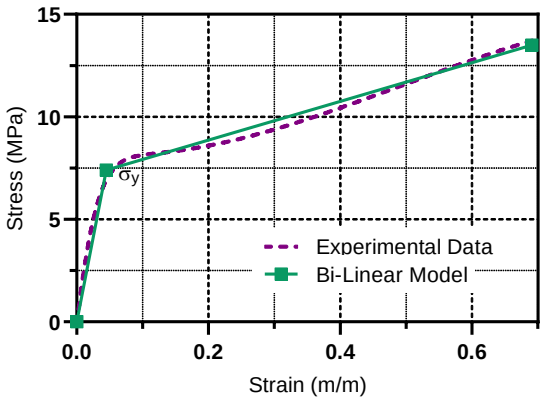

Figure 9.5: Bi-linear isotropic hardening material model representation of Kraibon HAA9275/45.

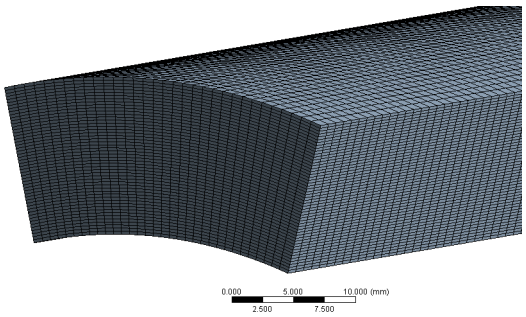

Figure 9.6: FEA model.

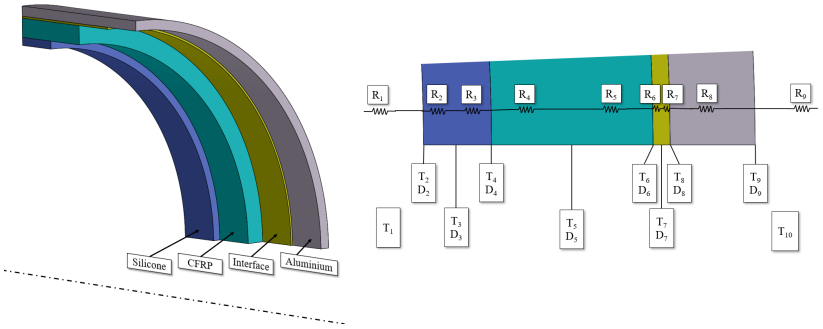

Figure 9.7: Part of cross section of hybrid aluminum/CFRP tube and geometric parameters.

to estimate the amperage required for the cure of the hybrid tube, sizing the transformer for the experimental part, and verifying the accuracy of analytical model by comparing the temperature trend of the tube over time and thickness.

To reduce the computation time some simplifications of the model (Figure 9.6 were adopted:

- Only a minor part of the length of the tube was considered.
- Only a six radiant slice of the tube was considered.
- The element size was 0.5 mm.

A constant Internal Heat Generation simulated the resistance heating. On the internal and external faces, the convection previously determined through experiments was applied. The FEA was started from the room temperature through a Transient Thermal Analysis with four steps and program-controlled substeps.

9.3 Thermal analytic model

An analytical model was developed from a balance equation between the produced energy, the stored, and the dissipated energy. The produced energy is created by the resistance heating (Joule effect) which introduces energy in the system. The stored energy is the energy that the materials absorb, and the dissipated is the energy which comes out of the system.

The analytical model was based on Fourier's law of thermal conductivity, in which the R_i terms are the *Equivalent Thermal Resistance* for each material.

Besides, as shown in Figure 9.7, the R_i terms are two for each material, excluding aluminum, because it was assumed, as an approximation, that the stored energy depends on the *middle temperature* of each material (T_3, T_5, T_7) and so the materials need to be divided into two equal parts which have half the thickness of the design one.

9.3.1 Dynamic of Heating

At first, the energy balance of the entire system can be written as shown in Equation 9.1.

$$dW_p = dW_s + dW_d \tag{9.1}$$

where dW_p, dW_s, and dW_d are the amount of produced energy with Joule effect, the energy stored, and the energy dissipated by the entire system in an infinitesimal time dt respectively.

Energy produced with Joule effect

The energy produced with Joule effect in dt with the aluminum tube is

$$dW_p = i^2 R_0(1 + \alpha T)dt \tag{9.2}$$

where i is the *effective current* (RMS) applied, R_0 is the electrical resistance of the aluminum tube calculated on his entire section, and α is the resistance coefficient of temperature.

The other electrical resistance of materials has not been taken into consideration, since the electrical resistance of the aluminum is several orders of magnitude lower. The system can be schematized as a set of resistors in parallel, in which one of these (aluminum tube) has an extremely low resistance value. For this reason, the set of resistors in parallel can be simplified to an equivalent resistance with the value of the smaller one, through which all the electric current will pass.

Energy Dissipated

The total energy dissipated in dt is given by the sum of the internal and external energy dissipated $dW_d = dW_{d,i} + dW_{d,e}$. The R_i terms are the equivalent thermal resistance of the material component (based on Fourier's law of thermal conductivity), T_{amb} is the room temperature, and T_{al} is the aluminum temperature. In this part, the Conduction relations for cylindrical geometry were used [169, 170]

$$\begin{aligned} dW_{d,i} &= \frac{T_{al} - T_{amb}}{\sum_{i=1}^{7} R_i} dt \\ dW_{d,e} &= \frac{T_{al} - T_{amb}}{R_9} dt \end{aligned} \tag{9.3}$$

so

$$\begin{aligned} dW_{d,i} + dW_{d,e} &= \frac{T_{al} - T_{amb}}{\sum_{i=1}^{7} R_i} dt + \frac{T_{al} - T_{amb}}{R_9} dt \\ &= \frac{(T_{al} - T_{amb})(\sum_{i=1}^{7} R_i + R_9)}{(R_9)(\sum_{i=1}^{7} R_i)} dt \end{aligned} \tag{9.4}$$

and defining

$$\begin{aligned} \Delta T &= (T_{al} - T_{amb}) \\ \gamma &= \frac{(\sum_{i=1}^{7} R_i + R_9)}{(R_9)(\sum_{i=1}^{7} R_i)} \end{aligned} \tag{9.5}$$

the total amount of dissipated energy in dt can be expressed as

$$dW_d = \gamma \Delta T dt \tag{9.6}$$

where R_1, R_2, R_3, R_4, R_5, R_6, R_7, R_8 and R_9 terms are

$$\begin{aligned} R_1 &= \frac{1}{h_{air,i}\pi D_2 L} \\ R_2 &= \frac{\ln(\frac{D_3}{D_2})}{2\pi\lambda_{sil}L} \\ R_3 &= \frac{\ln(\frac{D_4}{D_3})}{2\pi\lambda_{sil}L} \\ R_4 &= \frac{\ln(\frac{D_5}{D_4})}{2\pi\lambda_{CFRP}L} \\ R_5 &= \frac{\ln(\frac{D_6}{D_5})}{2\pi\lambda_{CFRP}L} \\ R_6 &= \frac{\ln(\frac{D_7}{D_6})}{2\pi\lambda_{int}L} \\ R_7 &= \frac{\ln(\frac{D_8}{D_7})}{2\pi\lambda_{int}L} \\ R_8 &= \frac{\ln(\frac{D_9}{D_8})}{2\pi\lambda_{al}L} \\ R_9 &= \frac{1}{h_{air,e}\pi D_9 L} \end{aligned} \tag{9.7}$$

in which λ terms are the thermal conductivity for each material, and the h_{air} ones are the air convection coefficients.

Energy Stored

The amount of stored energy depends on the material and the respective temperatures ΔT in the middle thickness as an approximation, so dW_s could be written as a sum of the contributions of the individual materials where the terms m and C are the mass of the material and the specific heat coefficient, respectively.

$$dW_s = (m_{al}C_{al}\frac{d(\Delta T)}{dt} + m_{int}C_{int}\frac{d(\Delta T_7)}{dt} + m_{CFRP}C_{CFRP}\frac{d(\Delta T_5)}{dt} + m_sC_s\frac{d(\Delta T_3)}{dt})dt \tag{9.8}$$

For example, ΔT_7 can be expressed as

$$\begin{aligned} \Delta T_7 &= \Delta T - \frac{dW_{d,i}}{dt} R_7 \\ &= \Delta T - \frac{T_{al} - T_{amb}}{dt \sum_{i=1}^{7} R_i} dt R_7 \\ &= \Delta T (1 - \frac{1}{\sum_{i=1}^{7} R_i} R_7) \end{aligned} \tag{9.9}$$

Similar considerations can be made for other internal positions, and in generic form, it can be represented as follows:

$$\Delta T_n = \Delta T (1 - \frac{\sum_{i=n}^{7} R_i}{\sum_{i=1}^{7} R_i}) \tag{9.10}$$

Finally, at this point, the stored energy can be determined. Simplifying the Equation 9.8 and inserting the terms of Equation 9.10

$$\begin{aligned} dW_s = (m_{al} C_{al} \frac{d(\Delta T)}{dt} + m_{int} C_{int} \frac{d(\Delta T (1 - \frac{\sum_{i=7}^{7} R_i}{\sum_{i=1}^{7} R_i}))}{dt} + \\ m_{CFRP} C_{CFRP} \frac{d(\Delta T (1 - \frac{\sum_{i=5}^{7} R_i}{\sum_{i=1}^{7} R_i}))}{dt} + m_s C_s \frac{d(\Delta T (1 - \frac{\sum_{i=3}^{7} R_i}{\sum_{i=1}^{7} R_i}))}{dt}) dt \end{aligned} \tag{9.11}$$

and defining ζ as

$$\zeta = m_{al} C_{al} + m_{int} C_{int} (1 - \frac{\sum_{i=7}^{7} R_i}{\sum_{i=1}^{7} R_i}) + m_{CFRP} C_{CFRP} (1 - \frac{\sum_{i=5}^{7} R_i}{\sum_{i=1}^{7} R_i}) + m_s C_s (1 - \frac{\sum_{i=3}^{7} R_i}{\sum_{i=1}^{7} R_i}) \tag{9.12}$$

the stored energy can be expressed as

$$dW_s = \zeta \frac{d(\Delta T)}{dt} dt \tag{9.13}$$

Dynamic of Heating solution

The extended form of Equation 9.1 divided by dt is

$$i^2 R_0(1 + \alpha\Delta T) = \zeta\frac{d(\Delta T)}{dt} + \gamma\Delta T \tag{9.14}$$

which can be written in the form

$$\frac{d\Delta T}{dt} + \delta\Delta T = \beta \tag{9.15}$$

where

$$\begin{aligned} \delta &= \frac{\gamma - \alpha R_0 i^2}{\zeta} \\ \beta &= \frac{R_0 i^2}{\zeta} \end{aligned} \tag{9.16}$$

The Equation 9.15 is a first order linear differential equation, which can be easily written and solved in function of time with initial condition $\Delta T(0) = 0$, so

$$\Delta T(t) = \frac{\beta}{\delta}(1 - e^{-t\delta}) \tag{9.17}$$

The temperature as function of time is shown here:

$$T(t) = \Delta T(t) + T_{amb} \tag{9.18}$$

The maximum reachable temperature is

$$\begin{aligned} \Delta T_{lim} &= \frac{\beta}{\delta} \\ T_{lim} &= \Delta T_{lim} + T_{amb} \end{aligned} \tag{9.19}$$

9.3.2 Dynamic of Cooling

As shown in Section 9.3.1, particularly the energy balance Equation 9.1 for the heating phase, the balance Equation for the cooling phase of the system is the sum of the energy stored and the energy dissipated in dt

$$dW_s + dW_d = 0 \tag{9.20}$$

dividing the Equation 9.20 by γ and defining $\phi = \frac{\gamma}{\zeta}$, the Equation 9.20 becomes

$$\phi\frac{d(\Delta T)}{dt} + \Delta T = 0 \tag{9.21}$$

This is also a first order linear differential equation whit the initial condition $\Delta T(0) = T_{mo}$, where T_{mo} is the maximum operating temperature. The cooling phase can be written in t domain in the form

$$\Delta T(t) = T_{mo} e^{-t\phi} \tag{9.22}$$

The temperature in function of time for the cooling phase is a similar exponential form expressed in Equation 9.17.

9.4 Experimental tests

9.4.1 Stress and strain tests

The Epoxy-Config and Rubber-Like-Config tubes were manufactured according to the process described above. Two biaxial, self-compensated strain gauges for aluminum were applied at each centerline of tube to monitor the axial and hoop strain evolution during the whole curing cycle. A Micro Measurement (Tee Rosette) 062UT was used and connected to a P3 model Strain indicator from Micro-Measurement. Two K types, RS 123-6306 thermocouples, connected to an AZ Instrument 88598 data logger, were used to monitor the temperature of the tube continuously.

The unconstrained aluminum tube was heated from room temperature up to 120 ℃ , and the resulting strain-temperature curve was interpolated by a 4^{th} order polynomial law, to describe the thermal conductivity of the materials. This procedure was adopted to try to reduce the approximation of the coefficient of thermal expansion which is linear by definition. The conductivity-coefficient obtained for the cooling tube was used for the heating test, confirming the obtained value.

9.4.2 Stress and Strains models validation

Figure 9.8 shows the temperature and strain evolution during the whole curing cycle for Epoxy-Config and Rubber-Like-Config, respectively. During the heating stage, the strain developed in the aluminum is similar for both configurations. Except for the initial hoop strain induced by the internal pressure application, the aluminum tube is in a stress-free condition until the resin begins to crosslinking at 90℃. After the reticulation of the resin occurs, a stress transfer between the components takes place. In this intermediate phase, the resulting residual thermal stresses were of the opposite sign of the one detected in the cooling phase. Indeed, during the cooling phase, due to CTEs mismatch, the aluminum tube undergoes in traction in longitudinal direction (aluminum $\alpha >$ CFRP α_1) and compression in the circumferential one (aluminum $\alpha <$ CFRP α_2). Only for the Epoxy-Config,

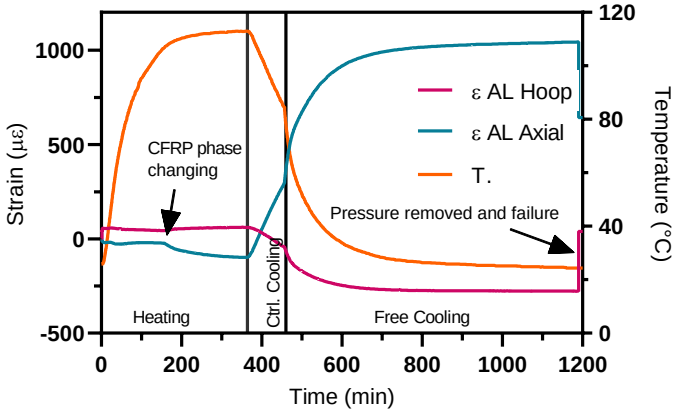

(a) Epoxy-Config tube.

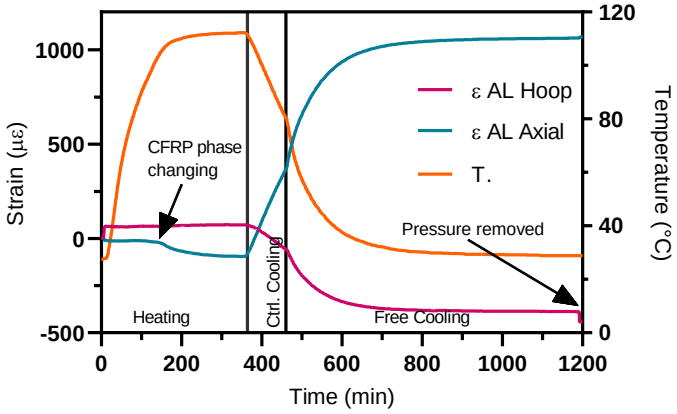

(b) Rubber-Like-Config tube.

Figure 9.8: Evolution of temperature and strains during curing cycle.

just after releasing the internal pressure at the end of the cooling phase, a sudden drop of the strain in both directions was recorded, proving that this configuration was in an unstable critical condition.

For both configurations, it can be observed that the absolute values of the strains developed during the cooling phase are reduced by the prestress induced during the intermediate phase mentioned above. For this reason, the starting temperature of the thermal simulations was tuned to avoid an overestimation of the strains due to the phenomenon mentioned above. Another phenomenon worthy of consideration in the numerical model is the temperature dependency of the elastic properties of the materials. For this reason, the axial and hoop strains were correlated to temperature for the whole cooling phase, as depicted in Figure 9.9. For

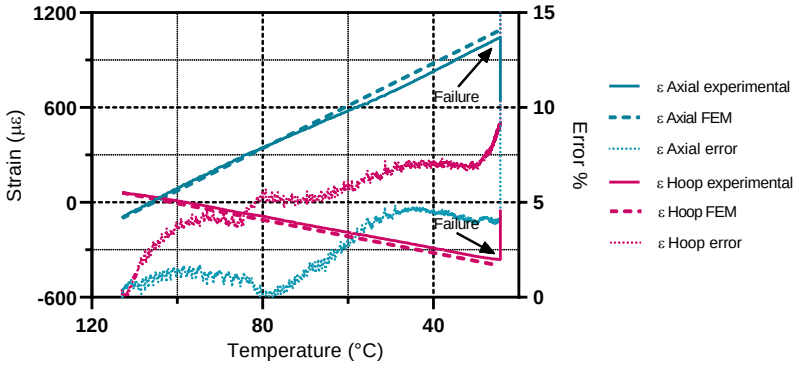

(a) Epoxy-Config tube.

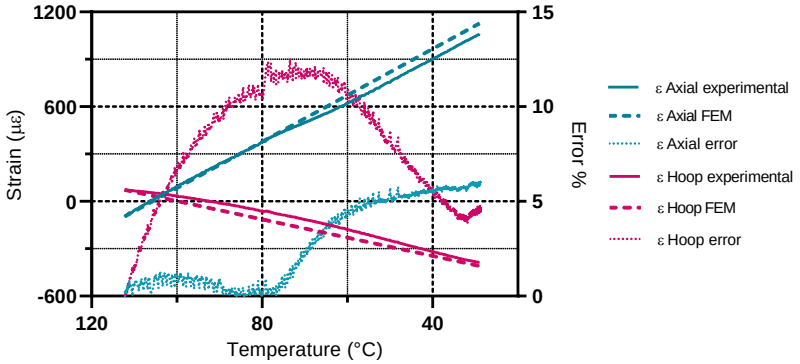

(b) Rubber-Like-Config tube.

Figure 9.9: Comparison between experimental and FEM strains in function of temperature during cooling phase.

both configurations, the strain vs. temperature curves can be approximated well with a linear curve, and, for this reason, the materials elastic properties were modeled as temperature independent. Comparing FEA and experimental results, the axial and hoop residual strain values reached room temperature are overestimated by the numerical model with an error below 10%, as reported in Table 9.5.

The found errors, visible in Figure 9.9, are probably due by two main phenomena: the nonlinearities of the mechanical properties of the rubber-like material and the phase change of the resin at glass transition temperature during the cooling phase.

Micrograph analysis confirms the supposed results. The cross-section of the Epoxy-Config tube (Figure 9.10a) shows delamination developed in the epoxy layer. On the contrary, micrographs of Rubber-Like-Config show perfect bonding between the aluminum and CFRP portion, and no delaminations were detected

Table 9.5: Comparison between experimental and numerical thermal residual strains on aluminum evaluated at the tube centerline at room temperature.

			Experimental	FEM	error %
Rubber-Like-Config	$\varepsilon_{z,max}$	(mm/mm)	1067.0	1130.9	6.0
	$\varepsilon_{\theta,max}$	(mm/mm)	-388.0	-409.7	5.6
Epoxy-Config	$\varepsilon_{z,max}$	(mm/mm)	1043.7	1088.1	4.3
	$\varepsilon_{\theta,max}$	(mm/mm)	-362.2	-399.1	10.2

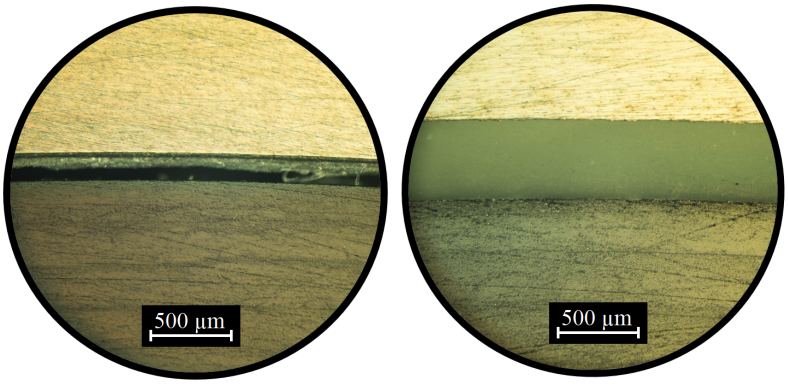

(a) Epoxy-Config. tube. (b) Rubber-Like-Config. tube.

Figure 9.10: Micrograph analysis of the cross sections of test tubes.

(Figure 9.10b).

9.4.3 Air convection coefficient determination

To correctly determine the dissipated energy, as shown in section 9.3.1 (Energy Dissipated), it is necessary to obtain the only unknown parameter: the air convection coefficient h_{air}. Once the dissipated energy has been calculated, it is possible to determine the sufficient electric current necessary to heat the tube at the curing temperature in 100 minutes (Section 9.4.7).

The aluminum tube was heated to 55 ℃ and was subsequently made to cool freely to room temperature to obtain the air convection coefficient experimentally. In this way, it was possible to determine the experimental air convection coefficient h_{air} by retrofitting the experimental curves with the theoretical model and by proper tuning of the FEM (Figure 9.11).

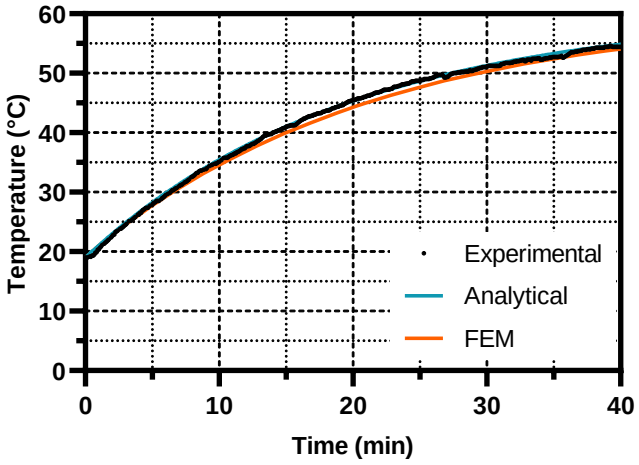

(a) Heating phase

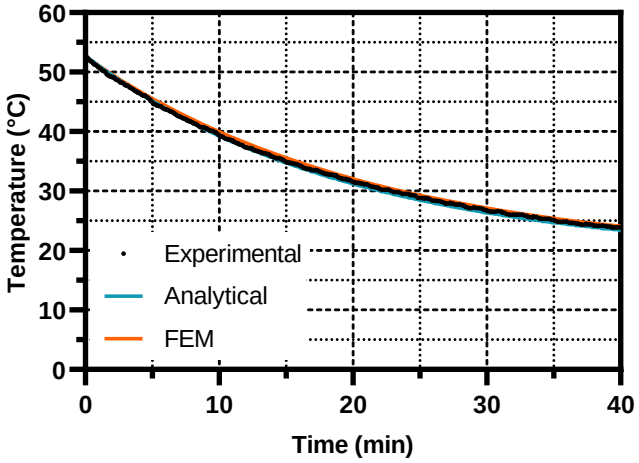

(b) Cooling phase

Figure 9.11: Experimental determination of air convection coefficient.

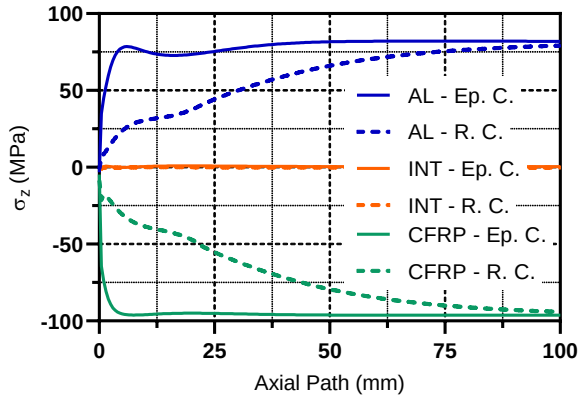

Figure 9.12: σ_z along axial path in Epoxy-Config and Rubber-Like-Config.

9.4.4 Numerical results and stresses performance

The stress distribution in the tubes were evaluated in cylindrical coordinates which coincide, for this particular case and staking sequence, with the principal directions of a composite unidirectional lamina ($z = x_1$, $\theta = x_2$, $r = x_3$) and laminate ($x = x$, $\theta = y$, $r = z$) according to Herakovich formulation[12]. Due to the selected material, geometry, and stacking sequence, the critical components are σ_z, σ_θ, σ_r and τ_{rz}.

For σ_r and τ_{rz}, stress continuity has to be kept between different material layers; there are no stress continuity requirements for σ_z and σ_θ according to stress equilibrium theory as reported by Herakovich[12]. For all stress components, maximum stress along r direction is observed near the interlayer region, for both configurations. Moreover, the maximum stress values are different for the path at the free edge and at 20 mm from the free edge. For the reasons above, the path along the axial direction has been applied at a radial distance of 0.05 mm out of the interface in the aluminum and CFRP parts and at the centerline for the interlayer. Furthermore, it was found that the highest stress levels occur within 100 mm from the free edges, and for this reason, path plots have been performed in this range. From Figures 9.12 to 9.15, σ_z, σ_r, σ_θ and τ_{rz} evolutions along the z-direction are reported.

From the free edge, as depicted in Figure 9.12, the σ_z stress grows asymptotically in a mirror way in both the aluminum and CFRP parts, ensuring a force equilibrium between the two materials. For both configurations, the asymptotic values of σ_z in the CFRP and aluminum parts are comparable, but it can be observed that stress distribution near the free edge is smoothed by adopting the rubber-like interlayer.

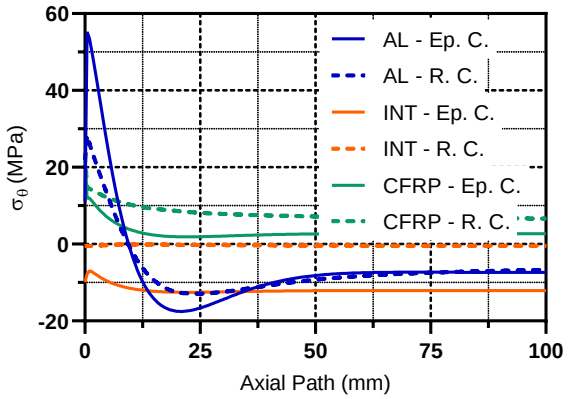

Figure 9.13: σ_θ along axial path in Epoxy-Config and Rubber-Like-Config.

σ_θ stress curves (Figure 9.13) have a similar shape, with a high-stress gradient in the proximity of the free edge, due to the particular deformation the tube assumes at its end. In particular, the maximum σ_θ stress developed in the CFRP is relatively high for both configurations (CFRP $\sigma_{\theta,max}$ in Epoxy-Config = 23.4 MPa, CFRP $\sigma_{\theta,max}$ in Rubber-Like-Config = 23.1 MPa). Indeed, in the axial direction, the capability of smoothing the stress peeks of the rubber interlayer is hindered by the closed shape geometry of the tube. Nevertheless, the stress peeks are still below the transverse tensile stress limit of the material ($\sigma_{L,y}$ = 30 MPa).

The σ_r stress curves (Figure 9.14) remain approximately zero for nearly the entire length of the tube, but at the free edge, stress peaks with a very high gradient develop. The σ_r for the epoxy interface is extremely high, while the rubber-like material exhibits negligible stress. The σ_r stresses that develop on the CFRP for both configurations are very high near the free edges. In this case, the rubber-like material does not help reduce the stress on CFRP and, consequently, the stress peaks are similar for both configuration.

In Figure 9.15, a comparison of the τ_{rz} distribution in the interlayer and CFRP, respectively, along the axial direction, is represented. For both configurations, the τ_{rz} values on the interlayer and CFRP are similar due to the closeness of the paths' radial position. For the case of Epoxy-Config, a high-stress concentration peak occurs at 0.7 mm from the free edge, with a maximum value of 22 MPa, which is critical for the shear strength of epoxy resin. For the case of Rubber-Like-Config, the τ_{rz} curve shows a "plateau" close to the free edge zone due to the plasticization interlayer.

Overall, for all the stress components which are not self-balanced by the closed shape geometry (tube), the rubber-like interlayer allows for the sliding of the two parts with different CTE due to its low yield strength and huge strain at break. In

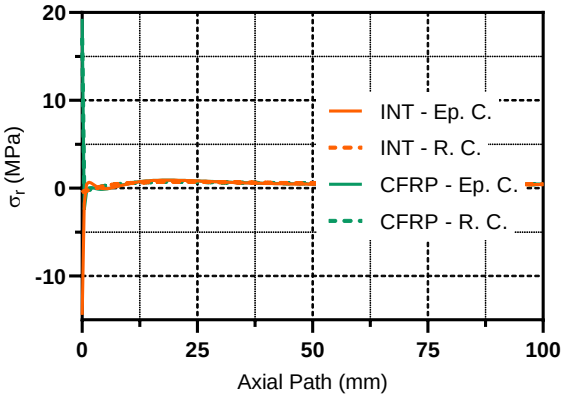

Figure 9.14: σ_r along initial 10 mm axial path in Epoxy-Config and Rubber-Like-Config.

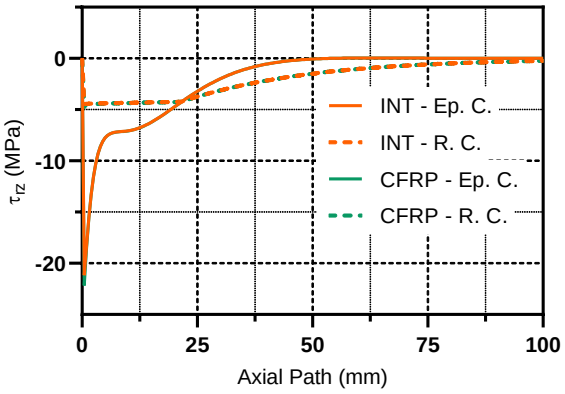

Figure 9.15: τ_{rz} along axial path in Epoxy-Config and Rubber-Like-Config.

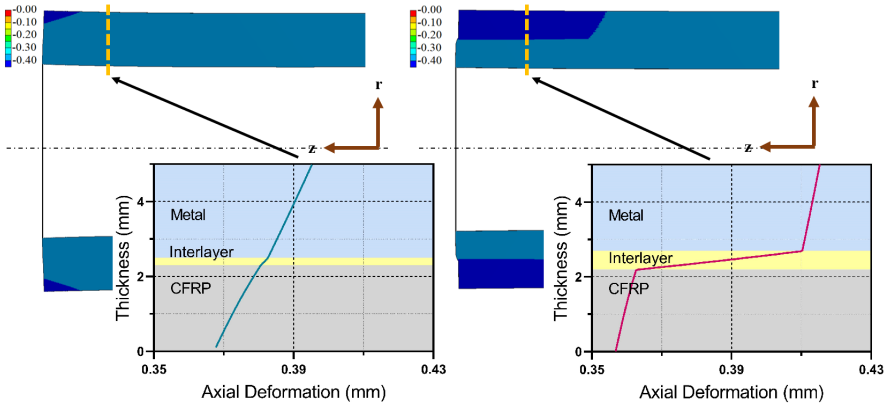

(a) Axial Deformation Epoxy-Config and Rubber-Like-Config.

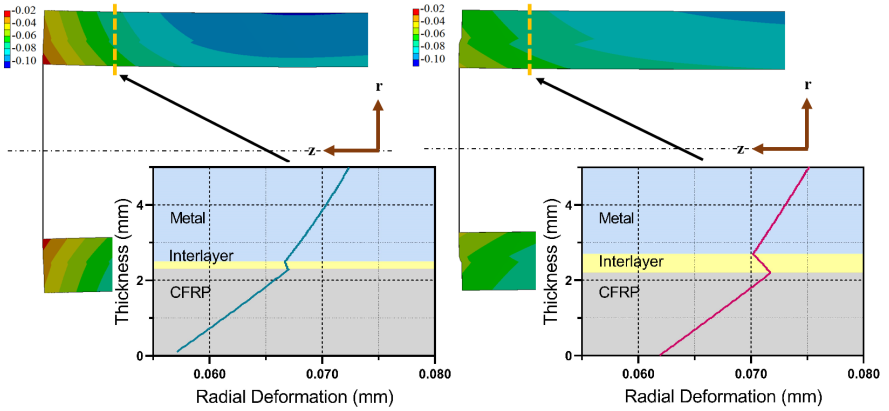

(b) Radial Deformation Epoxy-Config and Rubber-Like-Config.

Figure 9.16: Deformation in absolute value in Epoxy-Config and Rubber-Like-Config. Graphical displacement scale factor: 4.

particular, the analysis of deformations shows this phenomenon (Figure 9.16). In this way, the stress peaks developed at the free edge are smoothed and redistributed in a broader zone, preventing the premature failure of hybrid tube.

Globally, the multiaxial stress state influence has been evaluated using different failure criteria for each material type: Von Mises [171] for the isotropic aluminum, Tresca criterion for the interlayer, and Hashin 3D for the CFRP, according to [54]. The aluminum part does not present any criticality and, for this reason, is not discussed in detail. On the other hand, the CFRP and interlayer are critical, as shown in Figure 9.17. For the CFRP part, the Hashin 3D criterion was chosen due to its ability to identify the failure mechanism, predominantly the matrix failure. For the Epoxy-Config, the stress combination gave a failure index of approximately 1.0 for the CFRP and over 1.8 for the Epoxy-layer, which agrees with the experi-

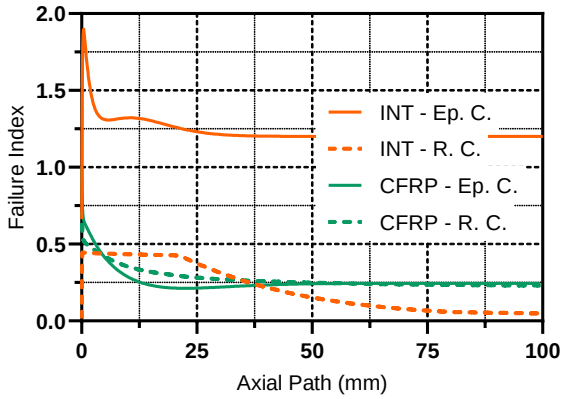

Figure 9.17: Failure Index along axial path in Epoxy-Config and Rubber-Like-Config test tube for the interlayer and CFRP.

mental results. However, for the Rubber-Like-Config, the stress combination gave a failure index of 0.7 for the CFRP and below 0.5 for the Rubber-Like layer. From these results, it is clear that the Epoxy-Config is not feasible because it manifests critical issues in both epoxy interlayer and CFRP.

9.4.5 Influence of geometric design parameters

Previously, it was established that the best solution involves inserting the Rubber-Like layer as interface. For this configuration, the interlayer is not critical due to its large deformation at break, while the aluminum works in the safety range. Therefore, the only crucial part is the CFRP, and for this reason, the influence of design parameters on the failure index is investigated only on this component.

Three tubes with different diameters (75, 115, and 150 mm) and reference thickness (2.5 mm for aluminum, 2.2 mm for CFRP) were investigated using their length as variable. As shown by FEA, the failure index grows with tube length up to 300 mm where it reaches a maximum and stable value, which means that for long tubes, which are usually required in converting industries, the failure index is not affected by the length.

Since the failure index is not affected by the tube length and the aluminum thickness can be considered a fixed parameter (being a coating), the remaining geometrical parameters are the CFRP thickness and the external tube diameter.

FEA showed that the failure index increases with the tube diameter in a parabolic manner. On the other hand, the risk of premature failure of the composite part decreases with its thickness. The results mentioned above suggest that for larger tube diameters, which are usually required in converting industries, it

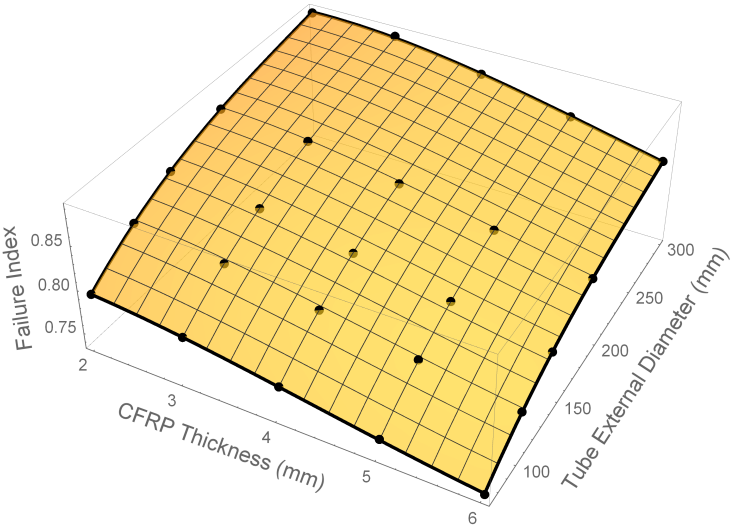

Figure 9.18: Polynomial regression model (3^{th} order).

is necessary to increase the CFRP thickness to avoid the premature failure of the hybrid tube. The combination of previous results were interpolated with a 3^{rd} order polynomial ($R^2 = 0.9997$) (Figure 9.18). Below is reported the polynomial function of the failure index ($f(t, D)$).

$$\begin{aligned} f(t,D) = 0.693 &+ 6.577 \times 10^4 t^3 + t^2(-7.824 \times 10^3 - 1.023 \times 10^5 D) \\ &+ D(1.553 \times 10^3 + (-5.227 \times 10^{-6} + 6.234 \times 10^{-9} D)D) \\ &+ t(1.463 \times 10^2 + (7.175 \times 10^5 + 1.271 \times 10^{-8} D)D) \end{aligned}$$

where t is the CFRP thickness and D the external tube diameter.

9.4.6 Influence of Rubber-like material parameters

In addition to the previous evaluation of the purely geometric parameters of hybrid tubes, the parameters of an ideal rubber-like material have been investigated to find the best characteristics for a rubber-like interface material to reduce the residual stress developed in the CFRP. For this reason, the influence of the elastic modulus, tangential modulus (for bi-linear elastic material model, as previously mentioned), thickness, and yield strength was evaluated on the failure index of CFRP.

It was found that the CFRP failure index is affected by the Elastic modulus (E) for values near the tangent modulus (E_y) but not for values higher than 200 Mpa and by the rubber-like material yield strength σ_y, especially for lower values of tangent modulus E_y.

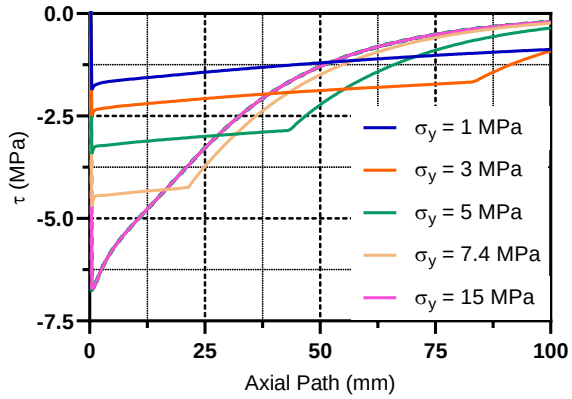

Figure 9.19: Influence of rubber-like material yield strength on τ_{rz}.

Figure 9.19, the τ_{rz} developed in the CFRP along the axial path is reported for different hypothetical yield strength of the rubber-like interlayer. Curves show a peculiar plateau observed in section 9.4.4, which smooth and redistribute the stress peeks developed at the free edge zone. By decreasing the yield strength, a more expansive stress redistribution zone is observed with a significant reduction of the stress peeks.

The numerical simulations show that the ideal characteristics of rubber-like material for the production of hybrid tubes should have minimum yield strength and tangent modulus. It can be notice how a parameter related to the strength of a material can modify the stress state of the system. This phenomenon is due by the changing from elastic modulus to tangent modulus of the interlayer after the stress has exceeded that of yield strength.

9.4.7 Hybrid tube curing and Thermal Results

The hybrid tube was heated to 90℃ with a ramp that approximates the theoretical one (Figure 9.20) of the Epoxy resin EP230. During the whole curing cycle, the external temperature of aluminum tube was acquired in different positions by thermocouples to verifying the analytical model and the FEA.

Subsequently, the hybrid tube was cut and lapped, and micrographs of the cross-section were made to verify the presence of voids, defects, and delaminations. DSC tests were performed to assess the quality of the crosslinking of EP230 by evaluating the transition temperature (Tg) of the CFRP part.

Thanks to the FEA of the first model, the convective air coefficient h_{air} was calculated. Besides, thanks to this parameter, it was possible to numerically verify, with the second FEM model, that 1880 Amps (RMS) are required to heat the

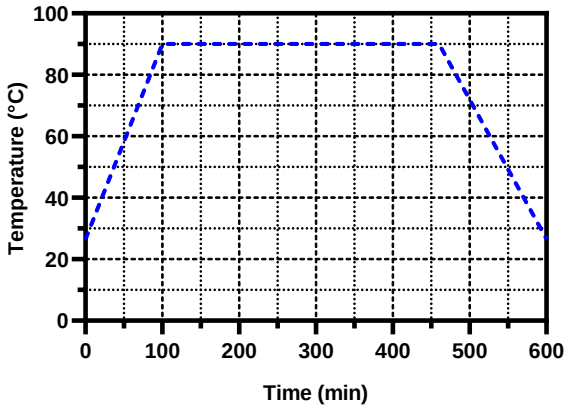

Figure 9.20: EP230 curing cycle.

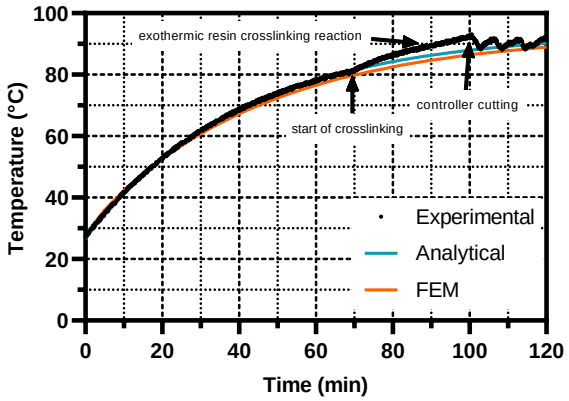

Figure 9.21: Heating ramp of the curing cycle.

hybrid tube to 90℃ in 100 minutes. Therefore, the electrical curing system was developed with a custom mono-phase transformer to reach the required amperage.

Subsequently, it was possible to carry out the electrical curing of the hybrid tube. The first part of the curing cycle (the ramp) is represented in Figure 9.21, which shows that the analytical model and the FEA represent the experimental test well.

Moreover, in the proximity of 80℃, there is a discontinuity in the experimental curve, for epoxy crosslinking begins with the consequent release of heat due to the exothermic reaction of epoxy resin EP230. Therefore, the area between the observed and analytical models represents the amount of exothermic crosslinking energy.

At 90℃, the controller starts cutting electric current with an on/off system,

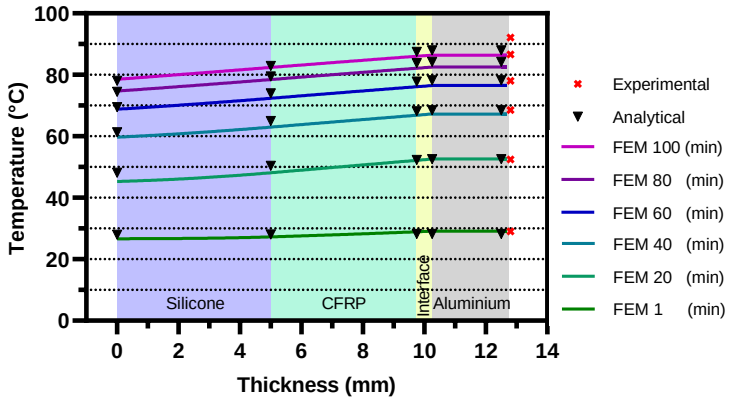

Figure 9.22: Trend of temperature through the thickness in time domain for analytical model and FEM.

allowing the tube to remain in a temperature range of 90℃ +/-2℃.

Then, the temperature trend through the thickness of the tube can be determined with the analytical model and FEA for each instant of time t considered (t = 1, 20, 40, 60, 80, 100 min) as reported in Figure 9.22. The analytical and numerical models present very similar results with small differences between them.

To obtain the ramp shown in Figure 9.21, an RMS of 1880 amps was required. The power used, given by the relation $W_p = R_0 i^2$ (simplification of Equation 9.3.1), was approximately 120 Watt, and the energy required per unit of mass is, therefore, less than 40 Wh/kg. Moreover, if a heat insulator were applied on the external surface of the tube during the electrical resistance curing, the power needed to heat it could still be reduced.

DSC analyses of the CFRP part of a hybrid tube cured by electrical resistance (Joule) were performed, and a Tg = 80℃ was discovered. From the results obtained, visible in Figure 9.23, it can be deduced that the crosslinking of the resin was complete.

9.5 Optimization of the stacking sequence

In common practice, an optimization process of composite structure is dominated by objective functions, design variables, and constraints [172]. A failure index of 0.7, according to Hashin 3D criterion, has been assumed as a constrain in the present work. Hashin 3D, as mentioned above, is an interactive failure criterion that enables to detect fiber or matrix failure and can describe as well the interlaminar one [173].

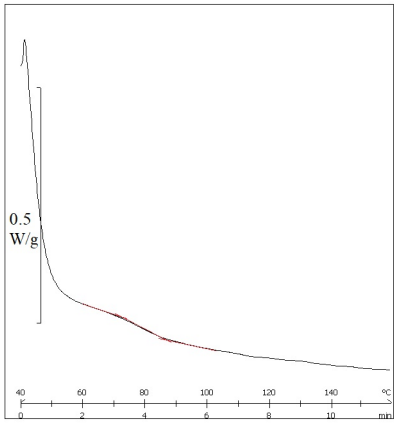

Figure 9.23: DSC results of the hybrid-CFRP tube.

Table 9.6: optimization stacking sequence comparison.

Layer number	Optimization angle value (deg)	Equivalent manufacturing angle value (deg)
1	-19.8	-30
2	+42.6	+30
3	-5.4	0
4	-0.9	0
5	-3.7	0
6	-9.2	0

The minimization of the deflection under pure bending load has been set as an objective function. The stacking sequence angles of the six layers that compose the laminate were set as a continuous variable. The optimization was performed using the "surrogate model" proposed in the Design Of Experiment (DOE) module of Ansys to evaluate the influence of the variables on the responses and reduce the global computational time.

After the DOE was performed, the tube has been optimized by a Multi-Objective Genetic Algorithm (MOGA). The best solution obtained with MOGA foresees a predominance of layers at almost zero degrees, except for the first two in contact with the viscoelastic layer (Table 9.6). This solution provided a failure index of 0.68, but manufacturability limits impose to use discrete angles for the prepreg wrapping sequence. For this reason, a new simulation with manufacturable layers angles (Table 9.6) was carried out, and the results were compared. An acceptable 3% increase of the deflection was obtained with a failure index of 0.63.

9.6 Final comments

In this chapter, a manufacturing process was implemented to realize two prototypes tubes with different interface layers: Epoxy and Rubber-Like (Krybon HAA).

The FEA revealed a complex triaxial stress state with a high gradient in the proximity of the free edges zone, which is often neglected in the literature investigating hybrid tubes. For the case of Epoxy-Config, the numerical results forecasted the premature failure of the hybrid tube during the cooling phase. These results were confirmed by real-time monitoring of the strain evolution during the entire curing cycle and micrograph analysis of the cross-section.

Additionally, the FEA results showed that the adoption of a rubber-like interlayer allows for smoothing the stress peeks (σ_θ, σ_r, and τ_{rz}) developed at the free edge due to its low yielding stress and high elongation at break. The feasibility of this solution was proven by experimental and micrograph analysis.

The numerical model, validated by experimental results, established the influence of length, total tube diameter, and thickness of materials in the design of hybrid tubes. A polynomial model, which interpolates the resulting failure index, was proposed. The best characteristics for rubber-like interface materials for the production of hybrid tubes were numerically identified.

Also, a novel curing process for hybrid metal-CFRP tubes was proposed. An analytic model was developed and verified through experimental tests and FEA.

The analytical model also allows us to correctly evaluate the amperage required for the curing and the temperature trend over time and in the thickness of tube; however, it neglects the heat due to the exothermic resin reaction.

Besides, the good quality of the final products is demonstrated by

- Micrographs that show no voids, no defects and no delaminations.
- DSC that shows the correct glass transition temperature of the matrix for tubes cured electrically.

Furthermore, in contrast to others, this method allows for easy checking and regulating the temperature of the tube during the curing thanks to feedback control and allows for the curing of different geometry of hybrid metal-CFRP components due to its flexibility.

It is also recommended to use metals with low thickness and high electrical resistances to avoid high amperage systems. As seen in the previous chapter, nanofibrous mats could be used to increase damping and remove the viscoelastic layer. In the next few years it will probably be a major application in hybrid tubes.

Bibliography

[1] G. D. Shaffer, An archaeomagnetic study of a wattle and daub building collapse, Journal of Field Archaeology 20 (1) (1993) 59–75.

[2] M. Kühnel, T. Kraus, The global cfrp market 2016, Experience Composites, Augsburg 21 (2016).

[3] M. Povolo, L. Raimondi, T. M. Brugo, A. Pagani, D. Comand, L. Pirazzini, A. Zucchelli, Design and manufacture of hybrid aluminum/composite co-cured tubes with viscoelastic interface layer, Procedia Structural Integrity 12 (2018) 196–203.

[4] M. Povolo, L. raimondi, T. Brugo, A. Pagani, D. Comand, L. Pirazzini, A. Zucchelli, Numerical and experimental analysis of the metal-composite interface in hybrid tubes, ICCS21 – 21st International Conference on Composite Structures (2018).

[5] M. Povolo, Optimization approach for designing composite components, JEC COMPOSITES 135 (2020).

[6] M. Povolo, T. M. Brugo, A. Zucchelli, Numerical and experimental investigation of aluminum/cfrp hybrid tubes with rubber-like interlayer, Applied Composite Materials 1–15.

[7] A. Kordijazi, S. K. Behera, O. Akbarzadeh, M. Povolo, P. Rohatgi, A statistical analysis to study the effect of silicon content, surface roughness, droplet size and elapsed time on wettability of hypoeutectic cast aluminum–silicon alloys, in: Light Metals 2020, Springer, 2020, pp. 185–193.

[8] A. Kordijazi, S. K. Behera, O. Akbarzadeh, M. Povolo, P. Rohatgi, Data-driven modeling of wetting angle and corrosion resistance of hypereutectic cast aluminum-silicon alloys based on physical and chemical properties of surface, Surfaces and Interfaces (2020).

[9] M. Povolo, J. Tabucol, T. M. Brugo, A. Zucchelli, Electrical resistance curing method for hybrid metal-cfrp tubes, Applied Composite Materials (2020) 1–15.

[10] M. Povolo, E. Maccaferri, D. Cocchi, T. M. Brugo, A. Zucchelli, Investigation on mechanical and damping behavior of nbr-pcl nano-reinforced unidirectional carbon fiber composites (2020).

[11] M. Povolo, M. I. Haider, N. P. Salowitz, P. K. Rohatgi, A preliminary study on niti shape memory alloy fiber-reinforced sn-bi self-healing metal matrix composite (2020).

[12] C. T. Herakovich, Mechanics of fibrous composites (1998).

[13] H. Goldstein, Classical mechanics, Pearson Education India, 2011.

[14] R. HOOKE, 1678: De potentia restitutiva, or of spring explaining the power of springing bodies.

[15] Y.-c. Fung, Foundations of solid mechanics, Prentice Hall, 2017.

[16] S. Lekhnitskii, P. Fern, J. J. Brandstatter, E. Dill, Theory of elasticity of an anisotropic elastic body, Physics Today 17 (1964) 84.

[17] E. J. Barbero, Introduction to composite materials design, CRC press, 2017.

[18] M. E. Gurtin, The linear theory of elasticity, in: Linear theories of elasticity and thermoelasticity, Springer, 1973, pp. 1–295.

[19] A. E. H. Love, A treatise on the mathematical theory of elasticity, at the University Press, 1906.

[20] G. Green, On the laws of the reflexion and refraction of light at the common surface of two non-crystallized media, Transactions of the Cambridge Philosophical Society 7 (1848) 1.

[21] ANSYS, Engineering data user's guide 16.2.

[22] ANSYS, Workbench user's guide 16.2.

[23] K. Pister, S. Dong, Elastic bending of layered plates, Journal of the Engineering Mechanics Division 85 (4) (1959) 1–10.

[24] S. Dong, On the theory of laminated anisotropic shells and plates, Journal of the Aerospace Sciences 29 (8) (1962) 969–975.

[25] E. Reissner, Y. Stavsky, Bending and stretching of certain types of heterogeneous aeolotropic elastic plates, Journal of applied mechanics 28 (3) (1961) 402–408.

[26] G. Kirchhoff, On the equilibrium and deflection of an elastic plate german, J. Reine Angew. Math 40 (1850) 51–88.

[27] S. Timoshenko, S. Woinowsky-Krieger, Theory of plates and shells, Engineering societies monographs, McGraw-Hill, 1959.

[28] B. Paul, Prediction of elastic constants of multi-phase materials, Tech. rep., BROWN UNIV PROVIDENCE RI (1959).

[29] Z. Hashin, The elastic moduli of heterogeneous materials, Journal of Applied Mechanics 29 (1) (1962) 143–150.

[30] Z. Hashin, B. W. Rosen, The elastic moduli of fiber-reinforced materials, Journal of applied mechanics 31 (2) (1964) 223–232.

[31] R. Hill, Theory of mechanical properties of fibre-strengthened materials: I. elastic behaviour, Journal of the Mechanics and Physics of Solids 12 (4) (1964) 199–212.

[32] R. Hill, A self-consistent mechanics of composite materials, Journal of the Mechanics and Physics of Solids 13 (4) (1965) 213–222.

[33] C.-T. Sun, J. D. Achenbach, G. Herrmann, Continuum theory for a laminated medium, Journal of Applied Mechanics 35 (3) (1968) 467–475.

[34] R. Younes, A. Hallal, F. Fardoun, F. H. Chehade, Comparative review study on elastic properties modeling for unidirectional composite materials, in: Composites and their properties, IntechOpen, 2012.

[35] W. Voigt, Ueber die beziehung zwischen den beiden elasticitatsconstanten isotroper korper, Annalen der physik 274 (12) (1889) 573–587.

[36] A. Reuss, Berechnung der fliessgrenze von mischkristallen auf grund der plastizitatsbedingung fur einkristalle., ZAMM-Journal of Applied Mathematics and Mechanics/Zeitschrift fur Angewandte Mathematik und Mechanik 9 (1) (1929) 49–58.

[37] J. H. Affdl, J. Kardos, The halpin-tsai equations: a review, Polymer Engineering & Science 16 (5) (1976) 344–352.

[38] C. C. Chamis, Mechanics of composite materials: past, present, and future, Journal of Composites, Technology and Research 11 (1) (1989) 3–14.

[39] R. M. Christensen, A critical evaluation for a class of micro-mechanics models, Journal of the Mechanics and Physics of Solids 38 (3) (1990) 379–404.

[40] T. Mori, K. Tanaka, Average stress in matrix and average elastic energy of materials with misfitting inclusions, Acta metallurgica 21 (5) (1973) 571–574.

[41] Y. Benveniste, A new approach to the application of mori-tanaka's theory in composite materials, Mechanics of materials 6 (2) (1987) 147–157.

[42] B. Budiansky, On the elastic moduli of some heterogeneous materials, Journal of the Mechanics and Physics of Solids 13 (4) (1965) 223–227.

[43] Z.-M. Huang, Simulation of the mechanical properties of fibrous composites by the bridging micromechanics model, Composites Part A: applied science and manufacturing 32 (2) (2001) 143–172.

[44] S. Li, Boundary conditions for unit cells from periodic microstructures and their implications, Composites Science and technology 68 (9) (2008) 1962–1974.

[45] A. Kelly, G. Davies, The principles of the fibre reinforcement of metals, Metallurgical Reviews 10 (1) (1965) 1–77.

[46] H. T. Hahn, J. G. Williams, Compression failure mechanisms in unidirectional composites, in: Composite materials: testing and design (seventh conference), ASTM International, 1986.

[47] S. W. Tsai, E. M. Wu, A general theory of strength for anisotropic materials, Journal of composite materials 5 (1) (1971) 58–80.

[48] R. Hill, The mathematical theory of plasticity, Vol. 11, Oxford university press, 1998.

[49] R. v. Mises, Mechanik der plastischen formanderung von kristallen, ZAMM-Journal of Applied Mathematics and Mechanics/Zeitschrift fur Angewandte Mathematik und Mechanik 8 (3) (1928) 161–185.

[50] S. W. Tsai, Strength theories of filamentary structure, Fundamental aspects of fiber reinforced plastic composites (1968).

[51] V. Azzi, S. Tsai, Anisotropic strength of composites, Experimental mechanics 5 (9) (1965) 283–288.

[52] S. W. Tsai, A survey of macroscopic failure criteria for composite materials, Journal of Reinforced Plastics and Composites 3 (1) (1984) 40–62.

[53] O. Hoffman, The brittle strength of orthotropic materials, Journal of Composite Materials 1 (2) (1967) 200–206.

[54] Z. Hashin, Failure criteria for unidirectional fiber composites, Journal of applied mechanics 47 (2) (1980) 329–334.

[55] A. Puck, W. Schneider, On failure mechanisms and failure criteria of filament-wound glass-fibre/resin composites, Plastics & Polymers 37 (127) (1969) 33–+.

[56] A. Puck, H. Schürmann, Failure analysis of frp laminates by means of physically based phenomenological models, in: Failure Criteria in Fibre-Reinforced-Polymer Composites, Elsevier, 2004, pp. 832–876.

[57] A. Puck, M. Mannigel, Physically based non-linear stress–strain relations for the inter-fibre fracture analysis of frp laminates, Composites Science and Technology - COMPOSITES SCI TECHNOL 67 (2007) 1955–1964. doi:10.1016/j.compscitech.2006.10.008.

[58] R. M. Jones, Mechanics of composite materials, taylor & francis, Inc., USA (1999).

[59] C. Davila, N. Jaunky, S. Goswami, Failure criteria for frp laminates in plane stress, in: 44th AIAA/ASME/ASCE/AHS/ASC Structures, Structural Dynamics, and Materials Conference, 2003, p. 1991.

[60] S. T. Pinho, C. G. Davila, P. P. Camanho, L. Iannucci, P. Robinson, Failure models and criteria for frp under in-plane or three-dimensional stress states including shear non-linearity (2005).

[61] T. Sebaey, N. Blanco, C. Lopes, J. Costa, Numerical investigation to prevent crack jumping in double cantilever beam tests of multidirectional composite laminates, Composites Science and Technology 71 (13) (2011) 1587–1592.

[62] R. Cuntze, A. Freund, The predictive capability of failure mode concept-based strength criteria for multidirectional laminates, in: Failure Criteria in Fibre-Reinforced-Polymer Composites, Elsevier, 2004, pp. 429–489.

[63] R. Cuntze, Efficient 3d and 2d failure conditions for ud laminae and their application within the verification of the laminate design, Composites Science and Technology 66 (7-8) (2006) 1081–1096.

[64] R. Cuntze, The predictive capability of failure mode concept-based strength conditions for laminates composed of unidirectional laminae under static triaxial stress states, Journal of Composite Materials 46 (19-20) (2012) 2563–2594.

[65] C. W. De Silva, Vibration damping, control, and design, CRC Press, 2007.

[66] S. Akishita, H. Benaroya, S. Huan Chen, M. Dabestani, M. Dahleh, K. Danai, C. DeFilippo, C. de Silva, I. Esat, E. Esmailzadeh, Vibration and shock handbook (2005).

[67] C. W. De Silva, Vibration monitoring, testing, and instrumentation, CRC Press, 2007.

[68] W. Voigt, Ueber innere reibung fester körper, insbesondere der metalle, Annalen der Physik 283 (12) (1892) 671–693.

[69] N. W. Tschoegl, The phenomenological theory of linear viscoelastic behavior: an introduction, Springer Science & Business Media, 2012.

[70] H.-P. Liu, D. L. Anderson, H. Kanamori, Velocity dispersion due to anelasticity; implications for seismology and mantle composition, Geophysical Journal International 47 (1) (1976) 41–58.

[71] A. V. Oppenheim, Discrete-time signal processing, Pearson Education India, 1999.

[72] J. M. Berthelot, M. Assarar, Y. Sefrani, A. E. Mahi, Damping analysis of composite materials and structures, Composite Structures 85 (3) (2008) 189–204. doi:10.1016/j.compstruct.2007.10.024.

[73] A. D. Nashif, D. Jones, J. Henderson, Vibration damping, 1985.

[74] J. M. Berthelot, Y. Sefrani, Damping analysis of unidirectional glass and Kevlar fibre composites, Composites Science and Technology (2004). doi:10.1016/j.compscitech.2003.10.003.

[75] M. J. Le Guen, R. H. Newman, A. Fernyhough, G. W. Emms, M. P. Staiger, The damping-modulus relationship in flax-carbon fibre hybrid composites, Composites Part B: Engineering (2016). doi:10.1016/j.compositesb.2015.10.046.

[76] A. Treviso, B. Van Genechten, D. Mundo, M. Tournour, Damping in composite materials: Properties and models, Composites Part B: Engineering (2015). doi:10.1016/j.compositesb.2015.03.081.

[77] S. H. Crandall, The role of damping in vibration theory, Journal of Sound and Vibration (1970). doi:10.1016/S0022-460X(70)80105-5.

[78] R. F. Gibson, Principles of Composite Material Mechanics, Isbn0070234515 9780070234512 (1994).

[79] R. D. Adams, D. G. Bacon, The Dynamic Properties of Unidirectional Fibre Reinforced Composites in Flexure and Torsion, Journal of Composite Materials (1973). doi:10.1177/002199837300700104.

[80] R. D. Adams, D. G. Bacon, Effect of Fibre Orientation and Laminate Geometry on the Dynamic Properties of CFRP, Journal of Composite Materials (1973). doi:10.1177/002199837300700401.

[81] G. C. Wright, The dynamic properties of glass and carbon fibre reinforced plastic beams, Journal of Sound and Vibration (1972). doi:10.1016/0022-460X(72)90907-8.

[82] R. D. Adams, D. G. Bacon, Measurement of the flexural damping capacity and dynamic Young's modulus of metals and reinforced plastics, Journal of Physics D: Applied Physics (1973). doi:10.1088/0022-3727/6/1/308.

[83] F. J. Guild, R. D. Adams, A new technique for the measurement of the specific damping capacity of beams in flexure, Journal of Physics E: Scientific Instruments (1981). doi:10.1088/0022-3735/14/3/021.

[84] D. X. Lin, R. G. Ni, R. D. Adams, Prediction and Measurement of the Vibrational Damping Parameters of Carbon and Glass Fibre-Reinforced Plastics Plates, Journal of Composite Materials (1984). doi:10.1177/002199838401800204.

[85] A. Wolfenden, S. Suarez, R. Gibson, Improved Impulse-Frequency Response Techniques for Measurement of Dynamic Mechanical Properties of Composite Materials, Journal of Testing and Evaluation (1987). doi:10.1520/jte10991j.

[86] J. Y. Lai, K. F. Young, Dynamics of graphite/epoxy composite under delamination fracture and environmental effects, Composite Structures (1995). doi:10.1016/0263-8223(94)00017-4.

[87] M. R. Maheri, R. D. Adams, Finite-element prediction of modal response of damped layered composite panels, Composites Science and Technology (1995). doi:10.1016/0266-3538(95)00074-7.

[88] C. Kyriazoglou, F. J. Guild, Finite element prediction of damping of composite GFRP and CFRP laminates - a hybrid formulation - vibration damping experiments and Rayleigh damping, Composites Science and Technology (2007). doi:10.1016/j.compscitech.2004.12.044.

[89] J. D. Stevenson, Structural damping values as a function of dynamic response stress and deformation levels, Nuclear Engineering and Design (1980). doi:10.1016/0029-5493(80)90238-1.

[90] J. Vanwalleghem, I. De Baere, M. Loccufier, W. Van Paepegem, External damping losses in measuring the vibration damping properties in lightly damped specimens using transient time-domain methods, Journal of Sound and Vibration (2014). doi:10.1016/j.jsv.2013.10.015.

[91] J. Li, Y. Narita, Analysis and optimal design for the damping property of laminated viscoelastic plates under general edge conditions, Composites Part B: Engineering (2013). doi:10.1016/j.compositesb.2012.09.014.

[92] M. R. Maheri, The effect of layup and boundary conditions on the modal damping of FRP composite panels, Journal of Composite Materials (2011). doi:10.1177/0021998310382314.

[93] High damping and high stiffness CFRP composites with aramid non-woven fabric interlayers, Composites Science and Technology 117 (2015) 92–99. doi:10.1016/j.compscitech.2015.06.002.
URL `http://dx.doi.org/10.1016/j.compscitech.2015.06.002`

[94] Y. Li, S. Cai, X. Huang, Multi-scaled enhancement of damping property for carbon fiber reinforced composites, Composites Science and Technology 143 (2017) 89–97. doi:10.1016/j.compscitech.2017.03.008.
URL `http://dx.doi.org/10.1016/j.compscitech.2017.03.008`

[95] R. M. Crane, J. W. Gillespie, Characterization of the vibration damping loss factor of glass and graphite fiber composites, Composites Science and Technology (1991). doi:10.1016/0266-3538(91)90030-S.

[96] D. D. Chung, Structural composite materials tailored for damping, in: Journal of Alloys and Compounds, 2003. doi:10.1016/S0925-8388(03)00233-0.

[97] R. G. Ni, R. D. Adams, A rational method for obtaining the dynamic mechanical properties of laminae for predicting the stiffness and damping of laminated plates and beams, Composites (1984). doi:10.1016/0010-4361(84)90274-X.

[98] J. Vantomme, A parametric study of material damping in fibre-reinforced plastics, Composites (1995). doi:10.1016/0010-4361(95)90415-V.

[99] D. J. Nelson, J. W. Hancock, Interfacial slip and damping in fibre reinforced composites, Journal of Materials Science (1978). doi:10.1007/BF00808058.

[100] S. W. S. Doebling, C. R. C. Farrar, M. B. M. Prime, D. W. D. Shevitz, Damage identification and health monitoring of structural and mechanical systems from changes in their vibration characteristics: a literature review, Los Alamos National Laboratory (1996). doi:10.2172/249299.

[101] Y. Sefrani, J. M. Berthelot, Temperature effect on the damping properties of unidirectional glass fibre composites, Composites Part B: Engineering (2006). doi:10.1016/j.compositesb.2005.10.001.

[102] T. L. Attard, L. He, H. Zhou, Improving damping property of carbon-fiber reinforced epoxy composite through novel hybrid epoxy-polyurea interfacial reaction, Composites Part B: Engineering 164 (July 2018) (2019) 720–731. doi:10.1016/j.compositesb.2019.01.064.

[103] R. F. Gibson, S. K. Chaturvedi, C. T. Sun, Complex moduli of aligned discontinuous fibre-reinforced polymer composites, Journal of Materials Science (1982). doi:10.1007/BF00752195.

[104] C. Subramanian, S. B. Deshpande, S. Senthilvelan, Effect of reinforced fiber length on the damping performance of thermoplastic composites, Advanced Composite Materials (2011). doi:10.1163/092430410X550872.

[105] J. L. Tsai, Y. K. Chi, Effect of fiber array on damping behaviors of fiber composites, Composites Part B: Engineering (2008). doi:10.1016/j.compositesb.2008.03.003.

[106] X. Lei, W. Rui, Z. Shujie, L. Yong, Vibration characteristics of glass fabric/epoxy composites with different woven structures, Journal of Composite Materials (2011). doi:10.1177/0021998310377943.

[107] A. E. Mahi, M. Assarar, Y. Sefrani, J. M. Berthelot, Damping analysis of orthotropic composite materials and laminates, Composites Part B: Engineering 39 (7-8) (2008) 1069–1076. doi:10.1016/j.compositesb.2008.05.003.

[108] S. Wray, J. N. Ashton, H. El-Sobky, An investigation of the influence of anisotropy and frequency on damping in short glass fibre reinforced polypropylene, Composite Structures (1990). doi:10.1016/0263-8223(90)90080-X.

[109] S. J. Hwang, R. F. Gibson, The effects of three-dimensional states of stress on damping of laminated composites, Composites Science and Technology (1991). doi:10.1016/0266-3538(91)90073-X.

[110] S. J. Hwang, R. F. Gibson, Contribution of interlaminar stresses to damping in thick laminated composites under uniaxial extension, Composite Structures (1992). doi:10.1016/0263-8223(92)90009-2.

[111] S. H. Zhang, H. L. Chen, A study on the damping characteristics of laminated composites with integral viscoelastic layers, Composite Structures 74 (1) (2006) 63–69. doi:10.1016/j.compstruct.2005.03.008.

[112] M. Assarar, W. Zouari, R. Ayad, H. Kebir, J. M. Berthelot, Improving the damping properties of carbon fibre reinforced composites by interleaving flax and viscoelastic layers, Composites Part B: Engineering 152 (July) (2018) 248–255. doi:10.1016/j.compositesb.2018.07.010.
URL `https://doi.org/10.1016/j.compositesb.2018.07.010`

[113] J. M. Berthelot, Y. Sefrani, Damping analysis of unidirectional glass fiber composites with interleaved viscoelastic layers: Experimental investigation and discussion, Journal of Composite Materials (2006). doi:10.1177/0021998306061303.

[114] J. M. Berthelot, Damping analysis of orthotropic composites with interleaved viscoelastic layers: Modeling, Journal of Composite Materials (2006). doi:10.1177/0021998306061302.

[115] E. R. Fotsing, M. Sola, A. Ross, E. Ruiz, Lightweight damping of composite sandwich beams: Experimental analysis, Journal of Composite Materials (2013). doi:10.1177/0021998312449027.

[116] A. Yildiz, K. Stevens, Optimum thickness distribution of unconstrained viscoelastic damping layer treatments for plates, Journal of Sound and Vibration (1985). doi:10.1016/0022-460X(85)90232-9.

[117] H. Kishi, M. Kuwata, S. Matsuda, T. Asami, A. Murakami, Damping properties of thermoplastic-elastomer interleaved carbon fiber-reinforced epoxy composites, Composites Science and Technology 64 (16) (2004) 2517–2523.

[118] S. Tahan Latibari, M. Mehrali, L. Mottahedin, A. Fereidoon, H. S. C. Metselaar, Investigation of interfacial damping nanotube-based composite, Composites Part B: Engineering (2013). doi:10.1016/j.compositesb.2013.02.022.

[119] N. A. Koratkar, J. Suhr, A. Joshi, R. S. Kane, L. S. Schadler, P. M. Ajayan, S. Bartolucci, Characterizing energy dissipation in single-walled carbon nanotube polycarbonate composites, Applied physics letters 87 (6) (2005) 063102.

[120] V. Hiremath, D. Shukla, Effect of particle morphology on viscoelastic and flexural properties of epoxy–alumina polymer nanocomposites, Plastics, Rubber and Composites 45 (5) (2016) 199–206.

[121] E. Maccaferri, L. Mazzocchetti, T. Benelli, T. M. Brugo, A. Zucchelli, L. Giorgini, Rubbery nanofibrous interleaves enhance fracture toughness and damping of cfrp laminates, Materials & Design 195 (2020) 109049.

[122] C. Garcia, J. Wilson, I. Trendafilova, L. Yang, Vibratory behaviour of glass fibre reinforced polymer (gfrp) interleaved with nylon nanofibers, Composite Structures 176 (2017) 923–932.

[123] R. Palazzetti, A. Zucchelli, Electrospun nanofibers as reinforcement for composite laminates materials–a review, Composite Structures 182 (2017) 711–727.

[124] Z. D. Xu, Y. X. Liao, T. Ge, C. Xu, Experimental and theoretical study of viscoelastic dampers with different matrix rubbers, Journal of Engineering Mechanics 142 (8) (2016) 04016051.

[125] X. Zhang, G. G. Chase, Electrospun elastic acrylonitrile butadiene copolymer fibers, Polymer 97 (2016) 440–448.

[126] H. Wu, Q. Hu, L. Zhang, H. Fong, M. Tian, Electrospun composite nanofibers of polybutadiene rubber containing uniformly distributed ag nanoparticles, Materials Letters 84 (2012) 5–8.

[127] X. Zhang, X. Yang, G. G. Chase, Filtration performance of electrospun acrylonitrile-butadiene elastic fiber mats in solid aerosol filtration, Separation and Purification Technology 186 (2017) 96–105.

[128] K. Phatcharasit, W. Taweepreda, K. Boonkerd, J. K. Kim, Electrospun epoxidized natural rubber with poly (vinyl chloride)(enr-pvc) nanofibrous for pemfc applications, in: Advanced Materials Research, Vol. 844, Trans Tech Publ, 2014, pp. 507–510.

[129] M. W. Thielke, E. P. Bruckner, D. L. Wong, P. Theato, Thiol-ene modification of electrospun polybutadiene fibers crosslinked by uv irradiation, Polymer 55 (22) (2014) 5596–5599.

[130] T. E. Kerr-Phillips, V. Woehling, R. Agniel, G. T. Nguyen, F. Vidal, P. Kilmartin, C. Plesse, J. Travas-Sejdic, Electrospun rubber fibre mats with electrochemically controllable pore sizes, Journal of Materials Chemistry B 3 (20) (2015) 4249–4258.

[131] S.-S. Choi, J.-P. Hong, Y. Seo, S. Chung, C. Nah, Fabrication and characterization of electrospun polybutadiene fibers crosslinked by uv irradiation, Journal of Applied Polymer Science 101 (4) (2006) 2333–2337.

[132] H. Liu, B. Lin, C. Jiang, A new method for determining coal seam permeability redistribution induced by roadway excavation and its applications, Process Safety and Environmental Protection 131 (2019) 1–8.

[133] R. D. Peters, Toward a universal model of damping–modified coulomb friction, arXiv preprint physics/0208025 (2002).

[134] Clarence W. de Silva, vibration and Shock handbook, 2005.

[135] C. W. De Silva, Vibration monitoring, testing, and instrumentation, 2007. doi:10.1201/9781420053203.

[136] G. Zhu, G. Sun, Q. Liu, G. Li, Q. Li, On crushing characteristics of different configurations of metal composites hybrid tubes, Composite Structures 175 (2017) 58–69.

[137] G. Zhu, X. Zhao, P. Shi, Q. Yu, Crashworthiness analysis and design of metal/cfrp hybrid structures under lateral loading, IEEE Access 7 (2019) 64558–64570.

[138] G. Zhu, G. Sun, H. Yu, S. Li, Q. Li, Energy absorption of metal, composite and metal/composite hybrid structures under oblique crushing loading, International Journal of Mechanical Sciences 135 (2018) 458–483.

[139] C. Reuter, T. Tröster, Crashworthiness and numerical simulation of hybrid aluminium-cfrp tubes under axial impact, Thin-Walled Structures 117 (2017) 1–9.

[140] P. Feng, L. Hu, P. Qian, L. Ye, Buckling behavior of cfrp-aluminum alloy hybrid tubes in axial compression, Engineering Structures 132 (2017) 624–636.

[141] P. Shi, Q. Yu, R. Huang, X. Zhao, G. Zhu, Crashworthy and performance-cost characteristics of aluminum-cfrp hybrid tubes under quasi-static axial loading, Fibers and Polymers 20 (2) (2019) 384–397.

[142] G. Sun, Z. Wang, J. Hong, K. Song, Q. Li, Experimental investigation of the quasi-static axial crushing behavior of filament-wound cfrp and aluminum/cfrp hybrid tubes, Composite Structures 194 (2018) 208–225.

[143] P. Feng, L. Hu, P. Qian, L. Ye, Compressive bearing capacity of cfrp–aluminum alloy hybrid tubes, Composite Structures 140 (2016) 749–757.

[144] G. Sun, H. Yu, Z. Wang, Z. Xiao, Q. Li, Energy absorption mechanics and design optimization of cfrp/aluminium hybrid structures for transverse loading, International Journal of Mechanical Sciences 150 (2019) 767–783.

[145] J. Zhang, B. Lu, D. Zheng, Z. Li, Axial crushing theory of metal-frp hybrid square tubes wrapped with antisymmetric angle-ply, Thin-Walled Structures 137 (2019) 367–376.

[146] R. Adams, N. Peppiatt, Stress analysis of adhesive bonded tubular lap joints, The Journal of Adhesion 9 (1) (1977) 1–18.

[147] J. H. Choi, D. G. Lee, Torque capacity of co-cured tubular lap joints, Journal of composite materials 31 (14) (1997) 1381–1396.

[148] C. T. Chon, Analysis of tubular lap joint in torsion, Journal of Composite Materials 16 (4) (1982) 268–284.

[149] S.-W. Jeon, Y. H. Cho, M.-G. Han, S.-H. Chang, Design of carbon/epoxy–aluminum hybrid upper arm of the pantograph of high-speed trains using adhesive bonding technique, Composite Structures 152 (2016) 538–545.

[150] J. K. Kim, D. G. Lee, D. H. Cho, Investigation of adhesively bonded joints for composite propeller shafts, Journal of composite materials 35 (11) (2001) 999–1021.

[151] J. Wang, H. Gao, L. Ding, Y. Hao, B. Wang, T. Sun, Y. Liang, Bond strength between carbon fiber–reinforced plastic tubes and aluminum joints for racing car suspension, Advances in Mechanical Engineering 8 (10) (2016) 1687814016674627.

[152] D. H. Cho, J. H. Choi, et al., Manufacture of one-piece automotive drive shafts with aluminum and composite materials, Composite structures 38 (1-4) (1997) 309–319.

[153] D. H. Cho, D. G. Lee, Manufacturing of co-cured composite aluminum shafts with compression during co-curing operation to reduce residual thermal stresses, Journal of composite materials 32 (12) (1998) 1221–1241.

[154] D. H. Cho, D. G. Lee, Optimum design of co-cured steel–composite tubular single lap joints under axial load, Journal of adhesion science and technology 14 (7) (2000) 939–963.

[155] H. S. Kim, J. W. Kim, J. K. Kim, et al., Design and manufacture of an automotive hybrid aluminum/composite drive shaft, Composite structures 63 (1) (2004) 87–99.

[156] M.-G. Han, Y. H. Cho, S.-W. Jeon, S.-H. Chang, Design and fabrication of a metal-composite hybrid pantograph upper arm by co-cure technique with a friction layer, Composite Structures 174 (2017) 166–175.

[157] C. Joseph, C. Viney, Electrical resistance curing of carbon-fibre/epoxy composites, Composites Science and Technology 60 (2) (2000) 315–319.

[158] S. Enoki, K. Iwamoto, R. Harada, K. Tanaka, T. Katayama, Heating properties of carbon fibers by using direct resistance heating, WIT Transactions on the Built Environment 124 (2012) 239–248.

[159] N. Athanasopoulos, G. Sotiriadis, V. Kostopoulos, A study on the effect of joule-heating during the liquid composite molding (lcm) process and on the curing of cfrp composite laminates, in: Proceedings of 10th international conference on flow processes in composite materials (FPCM10). Paper, no. 32, 2010.

[160] H. Asanuma, O. Haga, J. Ohira, K. Takemoto, M. Imori, Fabrication of cfrp/al active laminates, JSME International Journal Series A Solid Mechanics and Material Engineering 46 (3) (2003) 478–483.

[161] B. Mas, J. P. Fernández-Blázquez, J. Duval, H. Bunyan, J. J. Vilatela, Thermoset curing through joule heating of nanocarbons for composite manufacture, repair and soldering, Carbon 63 (2013) 523–529.

[162] N. Nguyen, A. Hao, J. G. Park, R. Liang, In situ curing and out-of-autoclave of interply carbon fiber/carbon nanotube buckypaper hybrid composites using electrical current, Advanced Engineering Materials 18 (11) (2016) 1906–1912.

[163] L. Zhu, R. Pitchumani, Analysis of a process for curing composites by the use of embedded resistive heating elements, Composites Science and Technology 60 (14) (2000) 2699–2712.

[164] B. Ramakrishnan, L. Zhu, R. Pitchumani, Curing of composites using internal resistive heating, Journal of manufacturing science and engineering 122 (1) (2000) 124–131.

[165] A. Mawardi, R. Pitchumani, Optimal temperature and current cycles for curing of composites using embedded resistive heating elements, Journal of heat transfer 125 (1) (2003) 126–136.

[166] M. Ashrafi, S. Devasia, M. E. Tuttle, Resistive embedded heating for homogeneous curing of adhesively bonded joints, International Journal of Adhesion and Adhesives 57 (2015) 34–39.

[167] S. S. Rao, Vibration of continuous systems, John Wiley & Sons, 2007.

[168] A. R. M. Ansys, help system, Engineering DATA, ANSYS, Inc (2017).

[169] A. F. Mills, Basic heat and mass transfer, Prentice hall, 1999.

[170] J. Holman, Heat transfer tenth edition (2010).

[171] R. v. Mises, Mechanik der festen körper im plastisch-deformablen zustand, Nachrichten von der Gesellschaft der Wissenschaften zu Göttingen, Mathematisch-Physikalische Klasse 1913 (1913) 582–592.

[172] S. Nikbakt, S. Kamarian, M. Shakeri, A review on optimization of composite structures part i: Laminated composites, Composite Structures 195 (2018) 158–185.

[173] F. Cesari, V. Dal Re, G. Minak, A. Zucchelli, Damage and residual strength of laminated carbon–epoxy composite circular plates loaded at the centre, Composites Part A: Applied Science and Manufacturing 38 (4) (2007) 1163–1173.